

AD-A274 380



①

QUEST Technical Report No. 547

**THE DYNAMICS OF PROJECTILES LAUNCHED
BY A TWO-STAGE LIGHT-GAS GUN**

Alan C. Mueller and Emerick M. Fernando

QUEST Integrated, Inc.
21414 - 68th Avenue South
Kent, Washington 98032

November 1991

Contract F40600-91-C-0008

S **DTIC**
ELECTE
DEC 28 1993
A

Approved for public release; distribution is unlimited.

Prepared for

UNITED STATES AIR FORCE
Arnold Engineering Development Center
Arnold AFB, Tennessee 37389-5000

12278 **93-31353**

93 12 27 075

QUEST Technical Report No. 547

THE DYNAMICS OF PROJECTILES LAUNCHED BY A TWO-STAGE LIGHT-GAS GUN

Alan C. Mueller and Emerick M. Fernando

QUEST Integrated, Inc.
21414 - 68th Avenue South
Kent, Washington 98032

November 1991

Contract F40600-91-C-0008

Approved for public release; distribution is unlimited.

Prepared for

UNITED STATES AIR FORCE
Arnold Engineering Development Center
Arnold AFB, Tennessee 37389-5000

REPORT DOCUMENTATION PAGE			Form Approved OMB No 0704-0188	
<small>Public reporting burden for this collection of information is estimated to average 1 hour per response, including the time for reviewing instructions, searching existing data sources, gathering and maintaining the data needed, and completing and reviewing the collection of information. Send comments regarding this burden estimate or any other aspect of this collection of information, including suggestions for reducing this burden, to Washington Headquarters Services, Directorate for Information Operations and Reports, 1215 Jefferson Davis Highway, Suite 1204, Arlington, VA 22202-4302, and to the Office of Management and Budget, Paperwork Reduction Project (0704-0188), Washington, DC 20503.</small>				
1. AGENCY USE ONLY (Leave blank)	2. REPORT DATE November 1991	3. REPORT TYPE AND DATES COVERED June 3 - Final Report: Dec. 3, 1991		
4. TITLE AND SUBTITLE The Dynamics of Projectiles Launched by a Two-Stage Light-Gas Gun		5. FUNDING NUMBERS F40600-91-C-0008		
6. AUTHOR(S) Alan C. Mueller and Emerick M. Fernando		8. PERFORMING ORGANIZATION REPORT NUMBER QUEST Technical Report No. 547		
7. PERFORMING ORGANIZATION NAME(S) AND ADDRESS(ES) QUEST Integrated, Inc. 21414 - 68th Ave. South Kent, Washington 98032		10. SPONSORING / MONITORING AGENCY REPORT NUMBER		
9. SPONSORING / MONITORING AGENCY NAME(S) AND ADDRESS(ES) U.S. Air Force Arnold Engineering Development Center Arnold AFB, TN 37389-5000		11. SUPPLEMENTARY NOTES		
12a. DISTRIBUTION / AVAILABILITY STATEMENT Approved for public release; distribution is unlimited.		12b. DISTRIBUTION CODE		
13. ABSTRACT (Maximum 200 words) <p>Projectiles launched at hypervelocities at the ballistic ranges of Arnold Engineering Development Center (AEDC) are subject to extreme loads of over 100,000 g's and occasionally fail. The ultimate material strength, in practice, limits the maximum speed to which the projectile can be launched and still remain intact. The projectiles are constructed from a variety of materials, including metals, plastics, and composites, and may undergo large viscoplastic deformations dependent on the strain rate. An understanding of the dynamics of the projectile and its interaction with the light-gas and barrel wall could lead to improved projectile designs and to procedures to reduce the possibility of model failure without degrading the overall performance of the gas gun. This Phase I effort addresses the need for an analytical tool to simulate accurately the projectile dynamic stresses. Under this study, a prototype finite element code has been developed and tested for axisymmetric projectiles to</p> <p style="text-align: right;">(Cont.)</p>				
14. SUBJECT TERMS Finite element method, Friction, Hypervelocity, Light-gas gun, Viscoelasticity, Viscoplasticity		15. NUMBER OF PAGES 116		
17. SECURITY CLASSIFICATION OF REPORT Unclassified		16. PRICE CODE		
18. SECURITY CLASSIFICATION OF THIS PAGE Unclassified	19. SECURITY CLASSIFICATION OF ABSTRACT Unclassified	20. LIMITATION OF ABSTRACT Unlimited		

Block 13. ABSTRACT (Cont.)

assess the feasibility of conducting realistic simulations. The model includes an accurate description of the strain-rate-dependent viscoelastic-viscoplastic behavior of plastics and ductile metals; a friction element to account for contact forces between the model/sabot and the barrel wall or between the interfaces within the model and the sabot; an erosion model to account for the ablating of the sabot surface at the barrel wall; and a side-pressure-loading element that models the pressure drop in any gas leaking around the ablated sides of the model/sabot.

Numerous simulations were conducted to examine the effects of the axial pressure history, material nonlinearities, side friction loads, and side loads due to pressure blow-by on a simplified "pyro" model/sabot configuration. The results of simulations of a dynamic test on a Lexan slug accelerated by a water cannon compare favorably to the experimental results in a companion study at QUEST. The simulations indicate that:

- The duration of the spikes in the pressure history relative to the time required for sound to propagate through the solid projectile is an important factor in determining whether tensile waves will appear in the projectile.
- Significant compression yielding occurs at the interface of the model and the sabot near the base of the model, most of which is associated with the peaks of the pressure spikes.
- The viscous relaxation time is an important parameter in describing the behavior of Lexan and nylon.
- The wear of Lexan while in the barrel is neither a linear function of position along the barrel nor the time after launch.
- Side-pressure loads, as a result of gas leaking around the sides of the Lexan, tend to move the maximum shear load closer to the top of the sabot and in the model.

It is anticipated that the analysis software developed in Phase II will provide the engineers at AEDC, and other agencies that operate hypervelocity light-gas guns, with an efficient tool for incorporating design improvements for projectile and gas gun operations

DTIC QUALITY INSPECTED 8

Accession For	
NTIS	CRA&I
DTIC	TAB
Unannounced	
Justification	
By	
Distribution /	
Availability Codes	
Dist	Avail and/or Special
A-1	

TABLE OF CONTENTS

REPORT DOCUMENTATION PAGE.....	i
LIST OF FIGURES AND TABLES	iv
1. INTRODUCTION.....	1
2. BACKGROUND.....	3
2.1 Two-Stage Light-Gas Gun.....	3
2.2 Geometry	3
2.3 Axial Pressure Loading	3
2.4 Strain-Rate-Dependent Materials	5
2.5 Friction And Erosion.....	7
2.6 Pressure Blow-By	7
2.7 Ballating	8
3. MATHEMATICAL MODEL	9
3.1 Kinematics	9
3.2 Momentum Laws.....	11
3.3 Constitutive Model.....	11
3.4 Boundary Conditions	17
3.5 Side-Wear Model.....	22
4. FINITE ELEMENT MODEL.....	24
4.1 FEAMOD Overview	24
4.2 Numerical Time Integration Method	25
4.3 Linear Solver	25
4.4 Discrete Constitutive Model	26
4.5 Boundary Conditions	27
4.6 Side-Wear Model.....	29
5. EXAMPLE SIMULATIONS AND RESULTS.....	30
5.1 Aluminum Pyro Model/Lexan Sabot	30
5.2 Water Cannon Tests on a Lexan Slug.....	57
6. CONCLUSIONS.....	69
REFERENCES	72
APPENDIX A. FEAMOD USER' GUIDE	
A.1 1987 FEAMOD User's Guide	
A.2 FEAMOD Amendments	
APPENDIX B. SUPERTAB UNIVERSAL FILE FORMAT DEFINITION	

LIST OF FIGURES AND TABLES

Figure 1.	Two-Stage Accelerated-Reservoir Light-Gas Gun	4
Figure 2.	Pyro Model/Sabot Configuration	4
Figure 3.	Modeled Dynamic Pressure at the Base of the Projectile..... in a Two-Stage Light-Gas Gun	6
Figure 4.	Drop-Impact-Derived Stress-Strain Curves	6
Figure 5.	Coordinate Systems and Deformation Definition	9
Figure 6.	Elastic-Viscoplastic Strain Rate Sensitivity	12
Figure 7.	Viscoelastic-Viscoplastic Strain Rate Sensitivity.....	15
Figure 8.	Material Model Comparison	15
Figure 9.	Gas Flow in the Annulus	17
Figure 10.	Variation of Gas State on Fanno Line	20
Figure 11.	Pressure and Mach Number Axial Distribution.....	20
Figure 12.	Maximum Load Von Mises Stress Contours (Elastic Simulation).....	32
Figure 13.	Peak Tensile Stress Contours	33
Figure 14.	Axial Stress Contours (Elastic-Viscoplastic Model).....	35
Figure 15.	Plastic Work Density Contours (Elastic-Viscoplastic Model)	42
Figure 16.	Maximum-Load Von Mises Contours with Friction at the Interfaces.....	53
Figure 17.	Acceleration of the Center of Mass with Friction	54
Figure 18.	Maximum-Load Von Mises Contours with Side-Pressure Loads	55
Figure 19.	Lexan Slug Erosion History	56
Figure 20.	Typical Water Cannon Pressure Pulse History.....	58
Figure 21.	Elastic Lexan Slug Axial Stress History ($p_{max} = 25$ ksi)	59
Figure 22.	Acceleration and Velocity of the Center of Mass (Elastic Model).....	62
Figure 23.	Elastic Lexan Slug Axial Stress at $t = 160 \mu s$ ($p_{max} = 40$ ksi).....	63
Figure 24.	Elastic-Viscoplastic Lexan Slug Axial Stress at $t = 160 \mu s$ ($p_{max} = 40$ ksi).....	63
Figure 25.	Elastic-Viscoplastic Lexan Slug Plastic Work at $t = 160 \mu s$ ($p_{max} = 40$ ksi).....	63
Figure 26.	Elastic-Viscoplastic Lexan Slug Axial Stress at $t = 160 \mu s$ ($p_{max} = 50$ ksi).....	64
Figure 27.	Elastic-Viscoplastic Lexan Slug Plastic Work at $t = 160 \mu s$ ($p_{max} = 50$ ksi).....	64
Figure 28.	Viscoelastic-Viscoplastic Lexan Slug Axial Stress History	66
Figure 29.	Acceleration and Velocity of the Center of Mass (Viscoelastic-Viscoplastic).....	68
Table 1.	Elastic-Viscoplastic Material Parameters	12
Table 2.	Viscoelastic-Viscoplastic Material Parameters for Lexan.....	14
Table 3.	Free/Contact Decision Matrix.....	29

1. INTRODUCTION

The ballistic test ranges at the Arnold Engineering Development Center (AEDC) use two-stage light-gas guns to launch projectiles up to speeds of 6 km/s. Graphite-tipped models, with 2.5-in. diameters and weighing near 500 g, are subjected to accelerations up to 100,000 g, pressures over 40,000 psi, and strain rates over 1000 s^{-1} . More massive models are subjected to even higher pressures. Under these high loads and strain rates, the dynamical stress can be quite high. Occasionally a model will fail, causing damage to the track and scattering model fragments on the track. A model failure not only results in the loss of test data, it also leads to expensive downtime to inspect and correct the damage.

The projectiles are often configured using a model and a sabot to hold the model in place. They are constructed from metals, plastics, and composites. Under these extreme loads, yielding can occur with the material flowing plastically at very high strain rates.

Although the major loads act along the axis, side loads are also important to the performance of the gun. The model/sabot must act as a seal to prevent "blow-by," the high-pressure gas leaking to the front side of the model. The relatively snug fit of the projectile in the bore also prevents the model from ballating as it travels down the barrel. The friction between the projectile and the gun-barrel wall tends to wear the model, reducing the effectiveness of the seal, increasing the side forces due to gas pressure, and allowing more freedom for the unwanted ballating motion.

The design of the model/sabot and the gas gun attempts to satisfy dual and often opposing requirements: maximizing the launch velocity while keeping the projectile intact. An understanding of the dynamics of the projectile and its interaction with the light gas and the barrel wall could lead to improved model/sabot designs and procedures to reduce the possibility of model failure without degrading the overall performance of the gas gun. However, due to the extremely high loadings and short operation times, it is difficult at best to measure the dynamical stresses acting within the projectile. Numerical simulations of the dynamical process have the potential to provide more insight into the complicated problem and offer a means to judge strategies for improving the model survivability and increasing the gas gun performance. It is the development of such a numerical dynamical stress model that is the subject of this effort.

In the discussion to follow, several key factors are identified that are important to the accuracy and utility of a numerical simulation of the dynamics of the model/sabot. These include:

- The coupled response of the model/sabot and the light gas.
- A good representation of the particular geometry and construction of the model/sabot.
- A viscoelastic-viscoplastic, rate-dependent material model that accounts for finite strains and large deformations.
- A side-friction and normal-force model resulting from contact with the barrel wall or high-pressure gas leaking to the sides.

During this Phase I study conducted by QUEST Integrated, Inc., the objectives of the effort have been to examine and develop models for each of these key areas and demonstrate their relative importance. In this final report for Phase I, we present the various parts of the mathematical model and the results of some example simulations. The appendices contain the User's Guide for the FEAMOD code, which is essential to this model, and some file format information and example files. First, however, in Section 2 we give some background information on the two-stage light-gas guns at AEDC and the specific problem to be solved.

2. BACKGROUND

2.1 Two-Stage Light-Gas Gun

Figure 1 shows the basic geometry and operation of a two-stage light-gas gun. The ignition of a chemical propellant drives a piston down a pump tube containing a reservoir of a light gas (often hydrogen) contained by a membrane. The piston compresses the gas nearly isentropically to high pressures and temperatures. When the pressure exceeds the membrane strength, the membrane ruptures, allowing a shock wave to accelerate the projectile. As the projectile moves down the barrel, the pressure applied at the base of the projectile slowly decreases, because much of potential energy initially present in the pressure is converted into the kinetic energy of the projectile and the gas. The key to obtaining a very high velocity requires a low-molecular-weight hot gas, to maximize the sound velocity, and the use of long barrels to contain the gas until most of the energy is imparted to the projectile. The survivability of the projectile depends on the maximum pressure applied. It is better to accelerate with a constant, but lower pressure than with a larger initial pressure that drops thereafter. To apply a more constant pressure to the base of the projectile, the piston may be constructed of two parts: a heavy back side and a light, easily deformable front side. This front side, deforming as an incompressible fluid, tends to accelerate as it moves into the constriction, thus accelerating light-gas compression and, in turn, maintaining a more constant pressure on the base.

2.2 Geometry

The models and sabots come in a variety of shapes and sizes. The "pyro" model shown in Figure 2 is more or less typical. The sabot is a lightweight, nonmetallic material (Lexan) and the model is usually a graphite-tipped light metal, which tends to ballast the center of mass forward for better aerodynamic stability. The sabot deforms plastically to provide a more uniform load on the model, to act as a seal to prevent the gas from leaking to the front side of the model, and to act as a stabilizer to prevent the projectile from rotating. At the end of the barrel, a barrier allows the model to pass through but prevents the sectioned sabot from traveling further.

2.3 Axial Pressure Loading

Consider the case of a constant pressure suddenly applied to the end of a free-elastic, homogeneous rod. A compressive wave passes through the rod at the speed of sound in the rod. On one side of the discontinuity the stress is equal to the applied pressure, p , with the material velocity equal to a fundamental velocity, $v = p/(\rho c)$, where ρ and c are the rod density and speed of sound, respectively. This wave reflects off the free boundary producing a tensile wave that cancels the outgoing compression wave. On reflection, the material velocity behind the shock jumps to $2v$. Each time the wave reflects off a boundary, the material velocity behind the shock ramps up one fundamental velocity. This ringing would occur indefinitely in an elastic rod. In reality, material viscous damping and inhomogeneities will tend to disperse and dissipate the shock. Eventually, the compressive stress field would

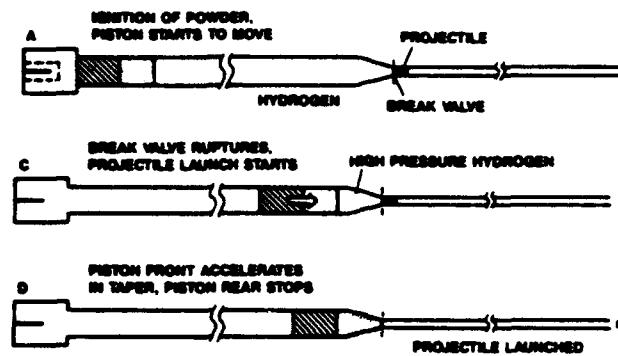


Figure 1. Two-Stage Accelerated-Reservoir Light-Gas Gun

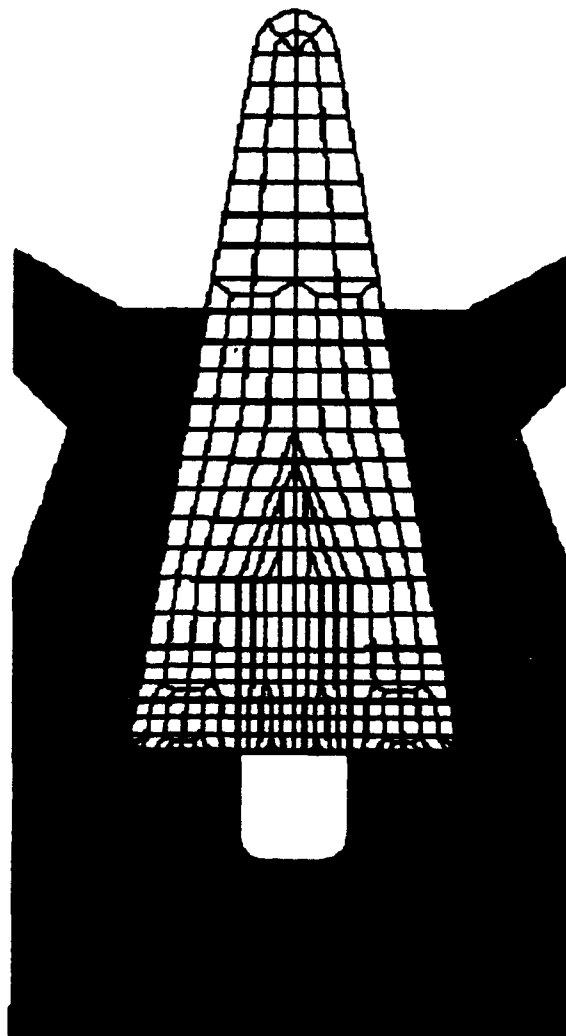


Figure 2. Pyro Model/Sabot Configuration

come to a steady state, dropping linearly from the applied stress to zero on the free end, and the entire rod would move at the velocity of the center of mass.

In this constant-pressure elastic example, the rod is either in compression or in a zero state of stress. Since most materials are very strong in compression, one might expect that the model/sabot could survive a very large pressure pulse. In the gas gun, the applied pressure is far from constant, and this in itself can produce a tensile wave in the rod. In Figure 3, the typical pressure history on the base of the model is predicted by the AEDC launch code. The pressure history exhibits a series of spikes that are a result of shock waves within the gas reflecting off the back surface of the sabot and off the driving piston. Consider the elastic rod case but with an applied pressure that decreases rapidly with time. As before, the compression wave reflects off the free surface, returning as a tensile wave, but now, because the applied pressure is weaker, the sum of the incoming tensile and outgoing compressive waves does not cancel but may in fact be in tension. These tensile waves are most certainly generated when the model undergoes a sharp decompression as it exits the barrel into a one-atmosphere environment. Model geometry, more complicated than rods, can also produce tensile stresses or stress concentrations within the body. A configuration constructed with different materials will provide additional interfaces by which to transmit or partially reflect the stress wave.

Since the generation and timing of shock waves within the light gas depend, in part, on the movement of the model/sabot, it is immediately clear that a numerical model must account for the coupled dynamical responses in both the solid model/sabot and the gas.

2.4 Strain-Rate-Dependent Materials

With the model/sabot subject to such large stresses, plastic deformations with large finite strains will occur, especially in the soft sabot. Near the shock wave the strain rates may be very high (in the elastic example, the region at the shock interface has infinite strain rates). Most materials, especially plastics such as Lexan, behave differently at high strain rates, with stresses dependent on the strain rate. Accounting for this viscoelastic-viscoplastic behavior will be important to the characterization of the state of stress in the model.

From estimates of the maximum compressive stresses acting on the sabot, it appears that the ultimate compressive strength at these high strain rates may be 2 to 3 times higher than the static compressive strength. Instrumented drop impact tests of Tardif and Marquis (1963) indicate that both the stiffness and the ultimate strength increase with strain rate. In these tests, a specimen sitting atop a stiff anvil bar is impact loaded by a stiff drop-weight bar released from a given height. The mean strain in the specimen is determined from integration of the strain rate, and the strain rate is implied via elastic wave relation involving the mean stress. This elastic relation introduces a degree of error, since the speed of sound is not a constant but in fact varies within the test. In addition, the strain rate deviates considerably from the mean strain rate during the course of the test. Nevertheless, the tests provide an important measure of the rate dependence of plastics under compressive loads. Figure 4a shows the derived compressive stress-strain curve for various mean strain rates (drop heights) in Lexan (labeled

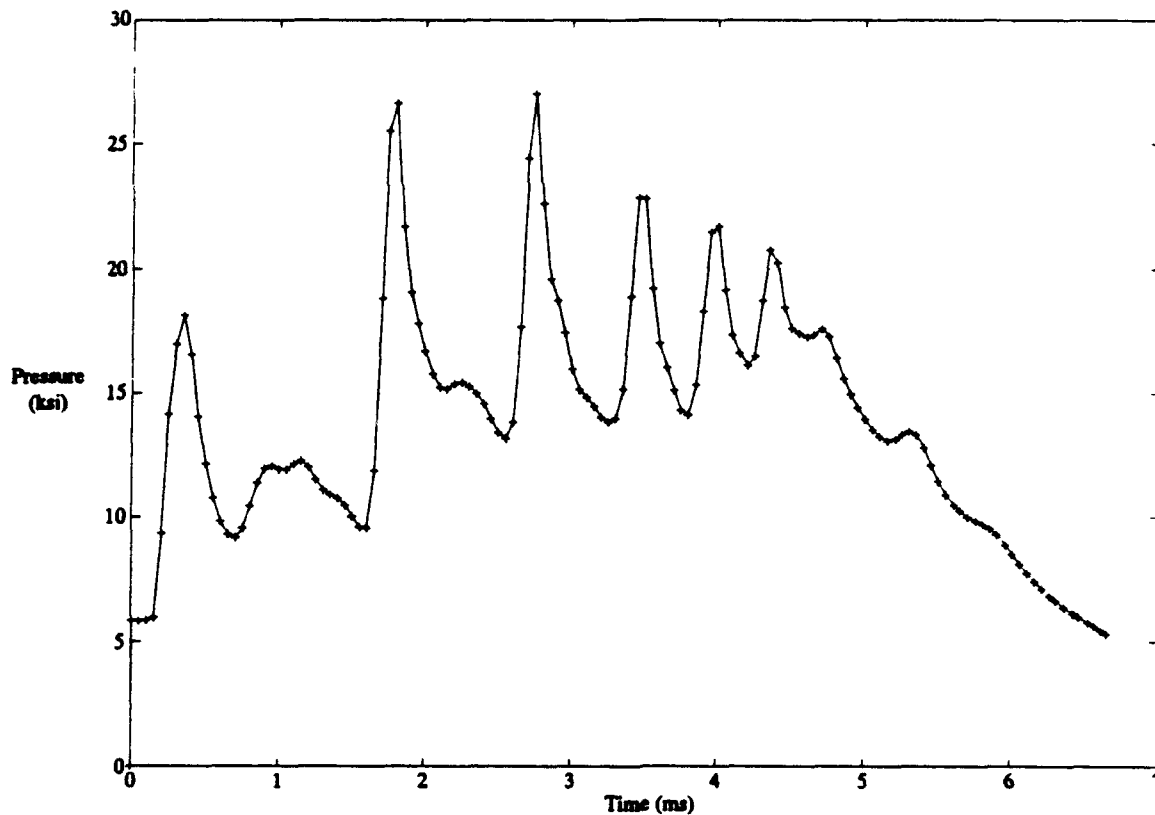
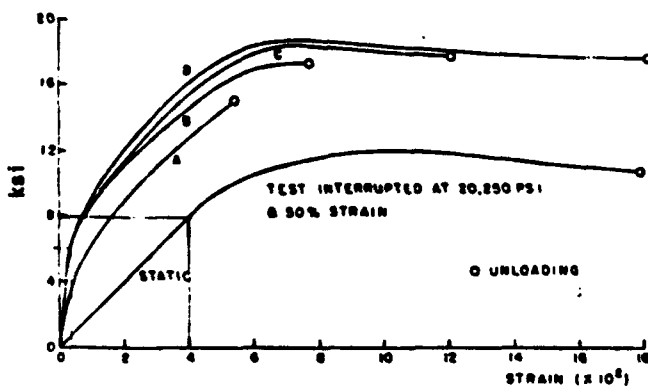


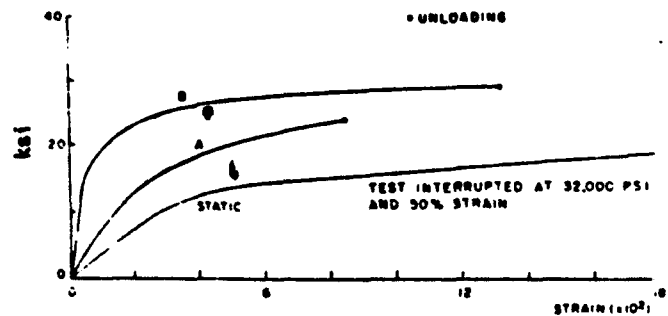
**Figure 3. Modeled Dynamic Pressure at the Base of the Projectile
In a Two-Stage Light-Gas Gun**

	E (PSI $\times 10^3$)	DROP Ht (FT)	PEAK $\dot{\epsilon}$ (SEC ⁻¹)	MEAN $\dot{\epsilon}$ (SEC ⁻¹)
STATIC	20	-	-	0.002
A	100	5	520	327
B	100	10	710	485
C	100	20	990	693
D	100	25	1,230	1,028



**a. Drop-impact-derived stress-strain
curves (Lexan)**

	E (PSI $\times 10^3$)	DROP Ht (FT)	PEAK $\dot{\epsilon}$ (SEC ⁻¹)	MEAN $\dot{\epsilon}$ (SEC ⁻¹)
STATIC	40	-	-	0.002
A	77	10	950	600
B	220	25	1,300	860



**b. Drop-impact-derived stress-strain
curves (nylon)**

**Figure 4. Drop-Impact-Derived Stress-Strain Curves
(from Tardif and Marquis, 1963)**

Zelux in Tardif and Marquis). The tests show a dramatic increase in the dynamic compressive strength over the static strengths. The stiffness also appears to rise, but an accurate determination of the slope is difficult since the linear portion is so small. Nylon exhibits similar results, as seen in Figure 4b. Lexan and nylon are in a class of plastic materials in which the 3% total elongation yield strength grows approximately linear with strain rate.

2.5 Friction and Erosion

The wall friction will melt, burn, and erode the model/sabot as it moves down the barrel and will eventually degrade the seal, allowing the gas to leak through to the side and front and slow the projectile. The erosion of the projectile also gives it more freedom to wobble or "ballat" as it travels down the barrel, producing additional undesirable, unsymmetrical side loads at the contact points between barrel and projectile. In fact, the inside diameter of the barrel at AEDC is tapered slightly to compensate for the wear on the model/sabot and hence maintains a good seal and prevents ballating from occurring. The slope of the taper has been selected by measuring the amount of wear on a tested model in an untapered barrel. Although superior performance with the tapered barrel has been observed, no other studies have been conducted to determine if the wear is over- or undercompensated in the current taper. A numerical simulation that accounts for the friction and wear offers the potential to further refine the taper design.

During its acceleration, the compressive axial stresses will tend to expand the sabot into the barrel wall to help maintain the seal but, in turn, produce a higher friction stress and a faster erosion rate. Eventually the erosion will be sufficient that the seal cannot be maintained even when the sabot is under high axial compression. On the other hand, if an axial tensile stress develops in the sabot, the necking in the radial direction can be sufficient to pull part of the sabot away from the barrel wall. One can imagine a scenario in which the sabot is periodically constrained and unconstrained as waves of compressive stresses pass through the sabot and reflect off the free surface as tensile stresses. This indicates that a friction model must be developed that recognizes and moves from three different possible states: no contact (free), sliding contact, and sticking contact.

2.6 Pressure Blow-By

Forces other than axial pressure force also come into play. The model/sabot must keep a seal to prevent "blow-by," the passage of high-pressure gas between the model/sabot and the barrel wall. As the sabot erodes, the space between the sabot and the barrel wall becomes sufficiently large to allow the gas to pass along to the front. Since the pressure in front of the sabot is subatmospheric, the gas flow is choked at the front with a standing shock. Because of the choking, the gas pressure exerted on the side of the sabot will gradually decrease in moving to the front of the sabot. It is well known that materials under compression do not fail as easily when under confining loads, and thus this side gas pressure helps to inhibit the failure of the sabot, but any possible turbulence may initiate a ballating motion.

2.7 Ballating

It is thought that the sabot ballats, or rocks back and forth, within the bore. This ballating is felt to be more severe as the sabot erodes and is given more freedom to rotate. Although a mechanism responsible for ballating motion has not been positively identified, several possible sources are:

- (1) An unsymmetrical pressure loading on the base of the sabot resulting from gas turbulence.
- (2) An unsymmetrical pressure loading on the base of the sabot resulting from uneven diaphragm rupture.
- (3) An eccentric center of mass.
- (4) An unsymmetrical pressure loading on the sides of the sabot resulting from leaking gas turbulence.
- (5) A slight curvature in the barrel.

The second is an unlikely source, since any uneven flow due to rupture would have time to relax to symmetry, especially in the later stages of the acceleration. The third source can be eliminated by careful design of the model/sabot. The fourth is not likely because, as we will show, the Reynolds numbers are no larger than 2000 in the annulus, not large enough to promote any strong turbulent pressure fluctuations. The fifth source is also unlikely because the accelerations resulting from the curvature of the barrel are small, even at the maximum velocities. Thus, the first seems to be the most likely source.

The Reynolds number, based on bore diameter, peak temperatures, and pressures, is about 10^6 , and large, unsymmetrical structures generated via any shock boundary-layer interactions could be sustained. Each time a shock reflects and moves away from the base of the sabot one might expect large structures to be generated. The magnitude of the pressure variations due to the structures is probably on the order of the pressure drop of the shocks within the bore. If the turbulent structures are near the size of the bore radius, then one might expect significant moments could be applied to torque the sabot.

Any more concrete analysis regarding the ballating motion would require a three-dimensional model along with a firm understanding of the statistical nature of the turbulent forcing. This is beyond the scope of this Phase I effort. Our efforts here have concentrated on the analysis of axisymmetric bodies undergoing axisymmetric loadings.

3. MATHEMATICAL MODEL

Each part of the mathematical model will be discussed in the subsequent sections. Most of the development will be applicable to general three-dimensional dynamics, and only when necessary will the discussion be restricted to axisymmetric dynamics.

3.1 Kinematics

In the standard definition, the position of the material point is the sum of the initial material position plus the change (or deformation) from the original position. Since the projectile is translating much further than the difference in deformation of neighboring points, this usual definition of the deformation may result in considerable round-off problems, especially in single precision. In an effort to avoid these round-off errors, a slightly new definition for the deformation vector has been adopted. In Figure 5, the initial, current, and intermediate configurations are shown. The absolute coordinate frame is at the center of mass of the initial configuration Ω^0 .

The deformation vector can be defined with reference to an inertial frame that translates relative to the absolute frame at the velocity of the center of mass of the body at time t^n :

$$\mathbf{x}(\mathbf{x}^0, t) = \bar{\mathbf{x}}(t^n) + (t - t^n) \bar{\mathbf{v}}(t^n) + \mathbf{x}^0 + \mathbf{u}^n(\mathbf{x}^0, t) \quad (1)$$

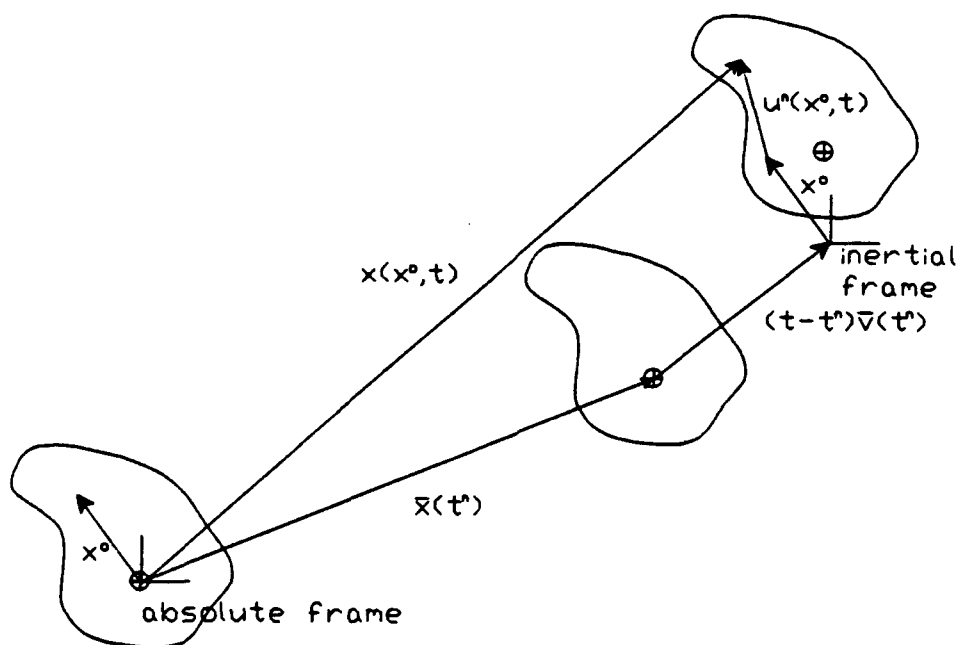


Figure 5. Coordinate Systems and Deformation Definition

The velocity of the material point can also be expressed as

$$\frac{\partial \mathbf{x}}{\partial t}(\mathbf{x}^o, t) = \bar{\mathbf{v}}(t^n) + \frac{\partial \mathbf{u}^n}{\partial t}(\mathbf{x}^o, t) \quad (2)$$

The absolute acceleration of a material point is then simply the relative acceleration

$$\frac{\partial^2 \mathbf{x}}{\partial t^2}(\mathbf{x}^o, t) = \frac{\partial^2 \mathbf{u}^n}{\partial t^2}(\mathbf{x}^o, t) \quad (3)$$

and the Green-Lagrange strain is also only an operation on the deformation \mathbf{u}^n

$$2\varepsilon_{ij}(\mathbf{x}^o, t) = \frac{\partial u_i^n}{\partial x_j^o} + \frac{\partial u_j^n}{\partial x_i^o} + \frac{\partial u_i^n}{\partial x_i^o} \frac{\partial u_j^n}{\partial x_j^o} \quad (4)$$

From the definition of the center of mass

$$\bar{\mathbf{x}}(t) = \frac{1}{M} \int_{\Omega^o} \rho^o \mathbf{x}(\mathbf{x}^o, t) d\Omega^o \quad (5)$$

with the fixed total mass

$$M = \int_{\Omega^o} \rho^o d\Omega^o \quad (6)$$

The center of mass becomes

$$\bar{\mathbf{x}}(t) = \bar{\mathbf{x}}(t^n) + (t - t^n) \bar{\mathbf{v}}(t^n) + \frac{1}{M} \int_{\Omega^o} \rho^o \mathbf{u}^n(\mathbf{x}^o, t) d\Omega^o \quad (7)$$

and its velocity

$$\bar{\mathbf{v}}(t) = \bar{\mathbf{v}}(t^n) + \frac{1}{M} \int_{\Omega^o} \rho^o \frac{\partial \mathbf{u}^n}{\partial t}(\mathbf{x}^o, t) d\Omega^o \quad (8)$$

If one defines a deformation \mathbf{u} based on a coordinate system that remains at the center of mass

$$\mathbf{x}(\mathbf{x}^o, t) = \bar{\mathbf{x}}(t) + \mathbf{x}^o + \mathbf{u}(\mathbf{x}^o, t) \quad (9)$$

then the relationship between the two different deformation systems is

$$\mathbf{u}(\mathbf{x}^o, t) = \mathbf{u}^n(\mathbf{x}^o, t) - \frac{1}{M} \int_{\Omega^o} \rho^o \mathbf{u}^n(\mathbf{x}^o, t) d\Omega^o \quad (10)$$

with a similar definition for the relative velocity

$$\frac{\partial \mathbf{u}}{\partial t}(\mathbf{x}^o, t) = \frac{\partial \mathbf{u}^*}{\partial t}(\mathbf{x}^o, t) - \frac{1}{M} \int_{\Omega^o} \rho^o \frac{\partial \mathbf{u}^*}{\partial t}(\mathbf{x}^o, t) d\Omega^o \quad (11)$$

In the numerical scheme to be described later, after each time step the coordinate system is redefined to be that at the current center of mass and translating with the current center-of-mass velocity. The deformation and relative velocity in the new coordinate frame can then be found from Equations (10) and (11).

3.2 Momentum Laws

The familiar form of the momentum equation is

$$\rho \frac{\partial^2 \mathbf{x}}{\partial t^2} = \nabla \cdot \boldsymbol{\sigma} \quad (12)$$

3.3 Constitutive Model

The constitutive model provides the relation between the stress and the strain. The discussion here will focus on the strain-rate-dependent properties of plastics, such as Lexan and nylon.

3.3.1 Elastic-Viscoplastic

Following the usual convention, the rate of change of the stress tensor is related linearly to the elastic part of the strain rate tensor

$$\dot{\sigma}_i = D_{ij} \dot{\epsilon}_j^e \quad (13)$$

where the strain rate is defined as the sum of elastic, viscoplastic, and thermal components

$$\dot{\epsilon}_i = \dot{\epsilon}_i^e + \dot{\epsilon}_i^p + \dot{\epsilon}_i^t \quad (14)$$

The thermal strain is defined as usual

$$\dot{\epsilon}_i^t = \alpha_i \dot{T} \quad (15)$$

The viscoplastic strain will be defined using the Bodner-Partom model (Bodner, 1984; Bodner and Partom, 1975):

$$\dot{\epsilon}_i^p = \Lambda s_i \quad (16)$$

where s_i is the deviatoric stress and Λ is a function of the second invariant of the deviatoric stress J_2 :

$$\Lambda = \frac{D_0}{\sqrt{J_2}} \exp \left[- \left(\frac{n+1}{2n} \right) \left(\frac{z^2}{3J_2} \right)^n \right] \quad (17)$$

The hardening yield stress z is given as a function of the plastic work W_p :

$$z = z_1 + (z_0 - z_1) \exp \left(-\frac{mW_p}{z_0} \right), \quad \dot{W}_p = \sigma_i \dot{\epsilon}_i^p \quad (18)$$

The material constants z_0 and z_1 are related to the yield and the ultimate stress, m controls the rate of work hardening, n controls the rate sensitivity of the material, and D_0 is the maximum plastic strain rate. Values of these parameters, shown in Table 1 for Lexan, have been chosen that reproduce the static stress curve provided by GE Plastics and give a reasonable estimate of the ultimate strength. The corresponding values shown for aluminum are taken from Bodner (1984) modified slightly for the T6 designation. The predicted stress as a function of strain for various strain rates, under uniaxial stress tests, is shown in Figure 6 for Lexan. It is evident from these curves that the 2% plastic yield

Table 1. Elastic-Viscoplastic Material Parameters

Material	E 10 ⁶ psi	ν	ρ lbm/in ³	CTE 10 ⁻⁶ °F ⁻¹	z_0 10 ³ psi	z_1 10 ³ psi	n	m	D_0 s ⁻¹
Lexan 500	0.5	0.38	0.045	17.9	12.0	38.0	1.5	200	1000
Aluminum 7075-T6	10.0	0.32	0.10	12.5	85.5	115.7	5	600	1000

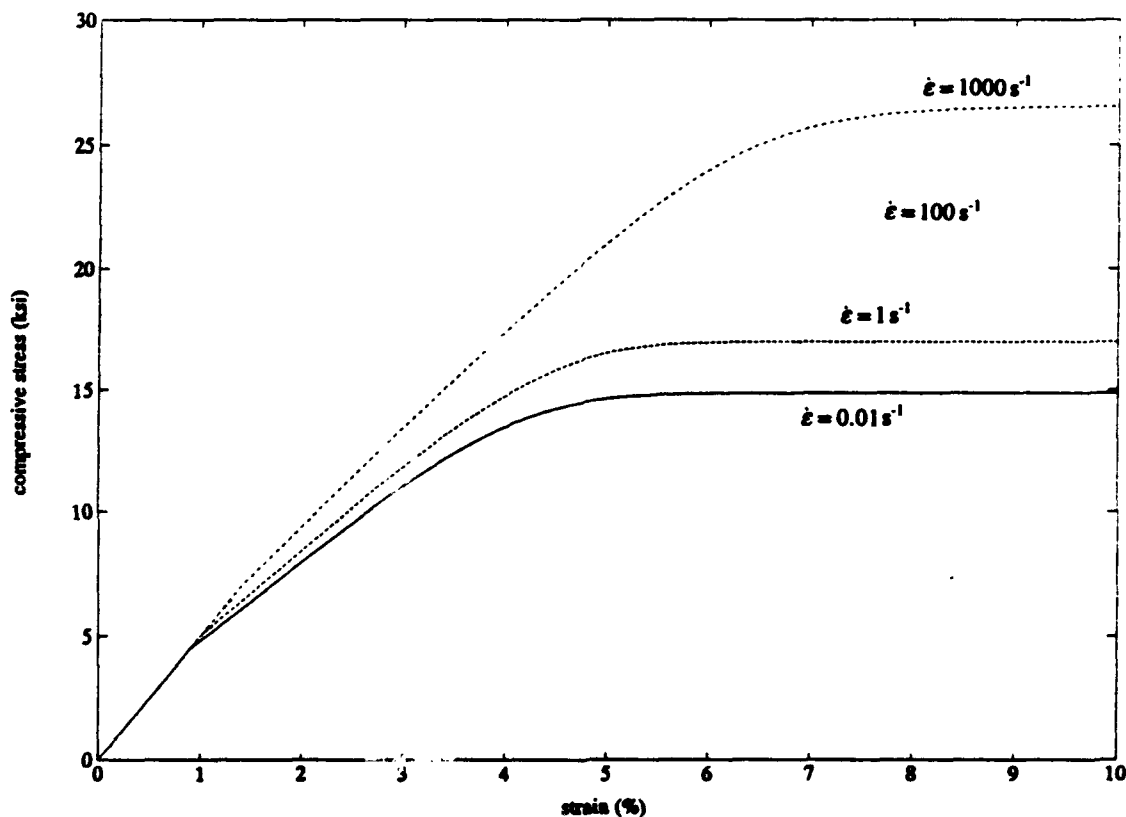


Figure 6. Elastic-Viscoplastic Strain Rate Sensitivity

stress varies approximately as a logarithm of the strain rate. Although the model predicts an increase in yield, it fails to reproduce the dependence of the stiffness on the strain rate.

3.3.2 Viscoelastic

A viscoelastic material exhibits a response that is dependent on its previous loading history. Under high strain rates, viscoelastic materials show an apparent stiffening. A linear viscoelastic model provides many of the essential features of this behavior:

$$\sigma = E\epsilon + \eta\dot{\epsilon} \quad (19)$$

or

$$\dot{\sigma} = E\dot{\epsilon} + \eta\ddot{\epsilon} \quad (20)$$

Assuming that the strain rate, strain, and stress are initially zero and the loading rate $\dot{\sigma}$ is constant, then the linear viscoelastic law may be solved to give the strain and strain rate:

$$E\epsilon = \sigma - \tau\dot{\sigma} \left[1 - \exp\left(-\frac{\sigma}{\tau\dot{\sigma}}\right) \right] \quad (21)$$

$$E\dot{\epsilon} = \dot{\sigma} \left[1 - \exp\left(-\frac{\sigma}{\tau\dot{\sigma}}\right) \right] \quad (22)$$

with $\tau = \eta/E$ the viscous relaxation time. As the stress rate approaches zero, the material behaves in an elastic manner, but with increasing stress rate, the strain and strain rate show an exponential decay. The strain rate approaches that implied by the elastic limit, and the effective stiffness

$$\frac{\partial \sigma}{\partial \epsilon} = \frac{E}{1 - \exp\left(-\frac{\sigma}{\tau\dot{\sigma}}\right)} \quad (23)$$

is, initially, infinite and asymptotically approaches the elastic modulus. In multidimensions, this linear elastic law can be expressed as

$$\dot{\sigma}_i = D_{ij}\dot{\epsilon}_j + N_{ij}\ddot{\epsilon}_j \quad (24)$$

If we further assume an isotropic material and that Poisson's ratio is unaltered by the viscous terms, then the relation can be further reduced to

$$\dot{\sigma}_i = D_{ij}(\dot{\epsilon}_j + \tau\ddot{\epsilon}_j) \quad (25)$$

which is the viscoelastic model used in this study.

3.3.3 Viscoelastic-Viscoplastic

It is rather straightforward to combine the viscoelastic and the elastic-viscoplastic strain laws into a unified viscoelastic-viscoplastic model stated simply as

$$\dot{\sigma}_i = D_v(\dot{\epsilon}_i + \tau \ddot{\epsilon}_i - \dot{\epsilon}_i^p) \quad (26)$$

This model is characterized by a total of eight parameters including two elastic constants, E and ν , the viscous relaxation time τ , and the five viscoplastic parameters described earlier. With the best estimates, from the available data, the material parameters for Lexan are shown in Table 2. Note that the viscoplastic parameters are different from those derived for the elastic-viscoplastic model in Table 1.

The rate dependence of Lexan is shown in Figure 7 under constant-stress-rate uniaxial loading. The curves are labeled in terms of a strain rate that is the stress rate divided by the elastic modulus, but the strain rate varies significantly over the duration of the test. The prediction of the viscoelastic-viscoplastic model compares favorably with the results of Tardif and Marquis (1963), as seen in Figure 4a. The Lexan used in the Tardif and Marquis study has a lower elastic modulus ($E = 200,000$ psi) than that quoted by GE Plastics, so a one-to-one comparison is not possible. Figure 8 shows a comparison of the viscoelastic, elastic-viscoplastic, and viscoelastic-viscoplastic material modes at a constant stress rate using the identical set of material parameters of Table 2.

The stress-strain curves of Tardif and Marquis are deduced in part with the help of an elastic wave model and may suffer from this incorrect paradigm. A more consistent approach to evaluate the viscoelastic-viscoplastic material parameters would be to compare and fit the results of this model to various loading rate tests.

By accurately representing the geometry and boundary conditions of the material test conditions (such as in the drop tester or the water cannon tester), the finite element model offers a powerful means to evaluate the material parameters. The relaxation time may also be related to the Q damping factor (Vassiliou et al., 1984).

Table 2. Viscoelastic-Viscoplastic Material Parameters for Lexan

E 10 ⁶ psi	ν	ρ lbm/in ³	CTE 10 ⁻⁶ °F ⁻¹	τ μs	z_o 10 ³ psi	z_i 10 ³ psi	n	m	D_o s ⁻¹
0.5	0.38	0.045	17.5	0.5	15.0	25.0	1.5	300	10 ⁵

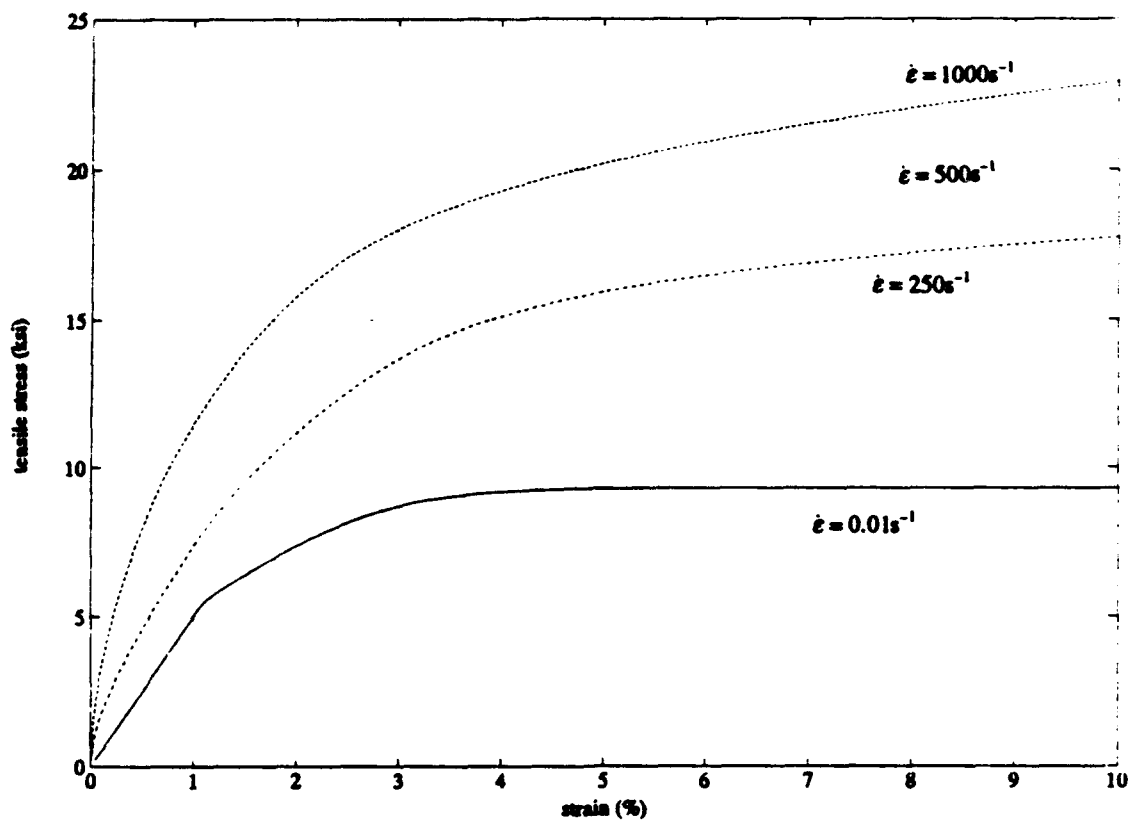


Figure 7. Viscoelastic-Viscoplastic Strain Rate Sensitivity

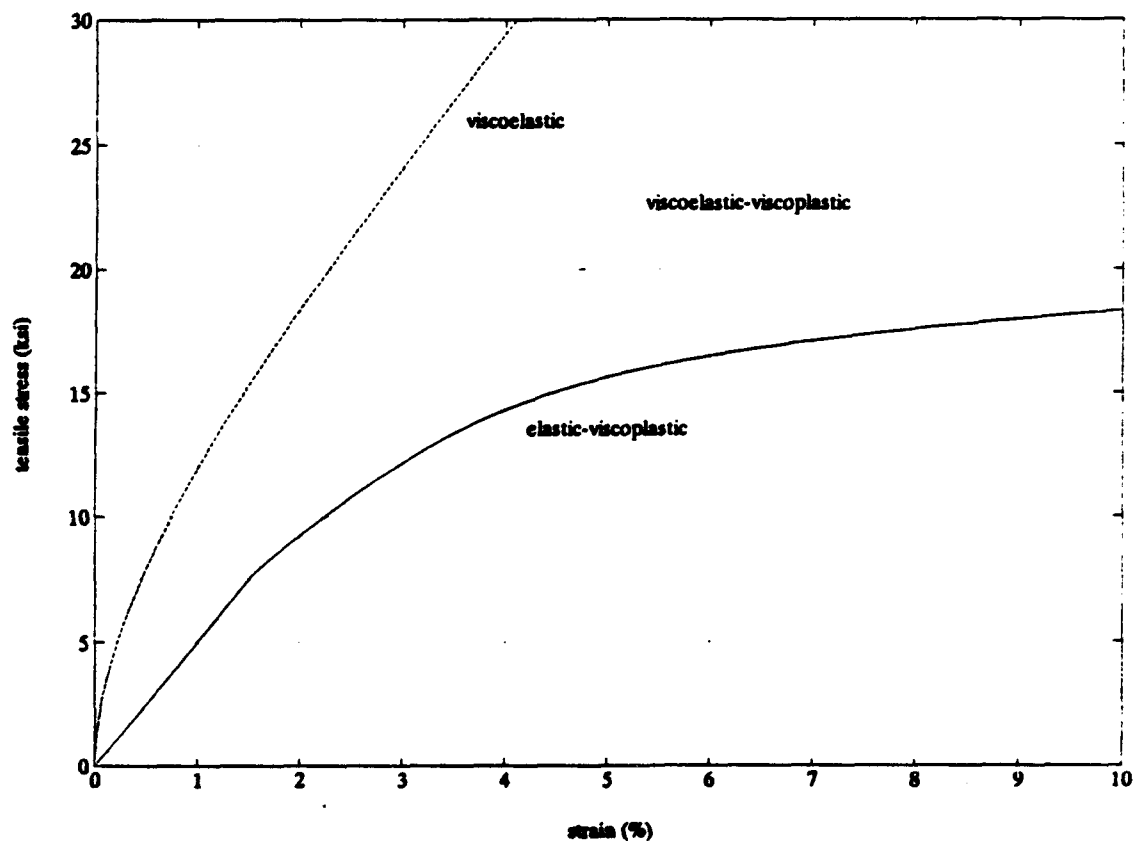


Figure 8. Material Model Comparison ($\dot{\epsilon} = 1000 \text{ s}^{-1}$)

3.3.4 Failure

The constitutive model presented provides a means to predict the relation between stress and strain but does not define the point at which failure is expected to occur. Tensile failure is usually defined in terms of ultimate stresses or a maximum elongation. A more exacting measurement can be determined from the fracture toughness and the size of the flaws in the material. Compression failure (shear failure) is generally defined by an ultimate compressive stress. The problem with these failure definitions is that they are strain-rate-dependent and generally only known for static tests. It would be desirable to have a strength measurement that is independent of the strain rate, but such a measure is not obviously clear. Two possible candidates would be plastic work or the value of the pseudo yield stress z , as defined in the Bodner-Partom model in Equation (18). Since plastic work is a result of the integration of the history of the yielding, it is less likely to be strain-rate-dependent.

3.4 Boundary Conditions

3.4.1 Base Pressure

At the base of the sabot, a pressure boundary condition is imposed. The pressure is assumed to be a given function of time, which must be determined either experimentally or via another model, such as the AEDC launch code.

3.4.2 Contact Friction Model

The friction model differentiates between three possible states:

- (1) No contact (free)
- (2) Sliding contact
- (3) Sticking contact

In this axisymmetric setting, the boundary conditions at $x^o = (r^o, z^o)$ for each state are as given below.

No Contact (Free)

The shear stress τ and normal stress σ acting on the sabot are zero, and the deformed radius of the material point is less than the radius of the bore, R , which can be a function of z if the barrel is tapered.

$$\tau = 0, \sigma = 0; r(r^o, z^o, t) < R \quad (27)$$

Sliding Contact

The deformed radius of the material point is equal to the bore radius, and the shear stress is equal in sign to the dynamic friction stress and points in the opposite direction of the axial velocity. The

normal stress exerted on the sabot must be greater than zero.

$$r(r^o, z^o, t) = R, \tau = -\text{sign}(v_z)\mu_s\sigma; \sigma > 0 \quad (28)$$

Sticking Contact

The material point is fixed to the barrel wall. The magnitude of the induced shear stress is less than the static friction, and the normal stress is greater than zero.

$$r(r^o, z^o, t) = R, z(r^o, z^o, t) = z^o; |\tau| < \mu_s\sigma, \sigma > 0 \quad (29)$$

Sticking contact occurs only at the initial stages of the launch and quickly moves to sliding contact when the shear stress induced by the sticking is larger than the static friction stress.

3.4.3 Side Pressure

3.4.3.1 Mean Side-Pressure Distribution

As the sabot erodes, an annulus gap between the sabot and the barrel wall will develop, allowing the gas to exert a side-pressure load. The approach taken here is a greatly simplified one, with the prime objective being to obtain an estimate of the pressure distribution along the annulus with limited availability of data. An idealized representation of the gap between the projectile and the gun barrel is sketched in Figure 9. It is assumed that the gap width is uniform circumferentially around the projectile and that the gap has a constant cross-sectional area in the longitudinal direction. The Eulerian coordinate system used has its origin based at the center of gravity of the projectile. It is further assumed that the projectile travels at a constant velocity V and is not accelerating.

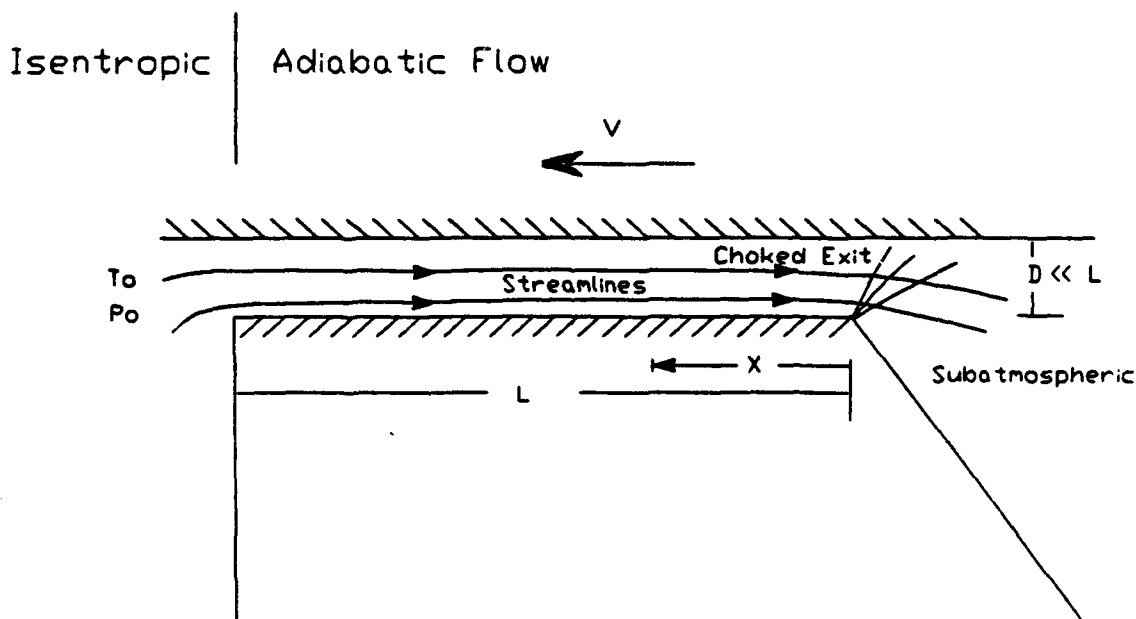


Figure 9. Gas Flow in the Annulus

At the base of the projectile, the pressure and temperature are denoted by p_0 and T_0 , respectively. Ahead of the projectile the very low gun-barrel pressure is denoted by p_b . We analyze the gas motion in the annulus using a one-dimensional approach. The gas flow is considered to be an adiabatic flow of a perfect gas, and the only overall effect of viscosity is considered to be a net drag force on the gas. The pressure differential across the two ends of the annulus is sufficiently high that the gas flow will be choked at the exit and, furthermore, the flow within the annulus will be completely subsonic. The pressure at the exit of the annulus is determined by the amount of frictional effects within the annulus (Shapiro, 1953, Ch. 6, Vol. II). The one-dimensional analysis used here assumes that the only effect of the translating wall (see Figure 9) is an increase in the net wall friction.

In order to obtain qualitative estimates of the pressure variation within the annulus, two more assumptions are necessary. These assumptions are:

- (1) The surfaces of the annulus are completely rough.
- (2) The friction factor is constant along the annulus.

The first assumption is probably quite justified due to the scouring of the gun barrel by the high-speed projectile and the narrow annulus width. It is shown later that the pressure distribution along the annulus is not significantly affected by the choice of the friction factor, which is an a posteriori justification for the second assumption. With these assumptions, the analysis is identical to the classical analysis of adiabatic (constant enthalpy) flow in a constant-area duct. The flow properties anywhere along the constant-area duct turn out to be solely a function of the local Mach number of the flow and the conditions at the choking point (exit of the duct). Denoting the values of velocity v , Mach number M , pressure p , stagnation pressure p_0 , and density ρ at the choking point by a superscript asterisk, the local flow properties may be expressed in a nondimensional manner by (see for example, Shapiro, 1953, Vol. I).

With the definition

$$\beta = 1 + \frac{\gamma - 1}{2} M^2 \quad (30)$$

The required compressible relations are

$$4f \frac{z}{D} = \frac{1 - M^2}{\gamma M^2} + \frac{\gamma + 1}{2\gamma} \ln \frac{(\gamma + 1) M^2}{2\beta} \quad (31)$$

$$\frac{p}{p^*} = \frac{1}{M} \sqrt{\frac{\gamma + 1}{2\beta}} \quad (32)$$

$$\frac{v}{v^*} = M \sqrt{\frac{\gamma + 1}{2\beta}} \quad (33)$$

$$\frac{T}{T^*} = \frac{\gamma + 1}{2\beta} \quad (34)$$

$$\frac{\rho}{\rho^*} = \frac{1}{M} \sqrt{\frac{2\beta}{\gamma + 1}} \quad (35)$$

$$\frac{p_o}{p_o^*} = \frac{1}{M} \sqrt{\left[\frac{2\beta}{\gamma + 1} \right]^{\frac{\gamma + 1}{\gamma - 1}}} \quad (36)$$

$$\frac{T_o}{T} = \beta \quad (37)$$

Here, z is the distance from the local point to the location where choking occurs. The dependence of these nondimensional ratios on the local flow Mach number is shown graphically in Figure 10. From this figure and an assumed friction factor f throughout the annulus, it is possible to obtain the Mach number and static pressure distributions along the annulus. The solution strategy is as follows. First, from an assumed friction factor and the known annulus hydraulic diameter (gap) and length, the factor $4fL/D$ is determined. From this value and Figure 10, the Mach number at the inlet to the annulus is determined. It is assumed that the flow upstream of the annulus entrance point is isentropic, i.e., no frictional entrance effects. Hence, knowing the entrance Mach number and the stagnation conditions upstream of the entrance, all flow quantities at the entrance to the annulus can be determined. From the now-known values of p_o/p_o^* and p_o at the entrance, p_o^* may be determined. The pressure distribution at any point along the annulus may then be evaluated by solving for the local Mach number using Equation (31) and inserting this value into Equation (32).

Since the flow is adiabatic, the stagnation temperature remains constant throughout the annulus. Using this fact and the known annulus end Mach number ($M^* = 1$) at the annulus exit, T^* may also be determined if T_o is provided. From p^* , M^* , and T^* , all flow quantities at the annulus exit may then be determined. Figure 10 may now be used to determine all flow quantities at any point within the annulus. For example, it is known that the Mach number within the annulus increases from the inlet value to the exit value.

Graphs of the Mach number, static pressure, and wall friction variation within the annulus are shown in Figures 11a through 11c for several choices of friction factors. In order to obtain these values, it has been assumed that the annulus is 0.005 in. wide and 3 in. long and that the upstream stagnation pressure and temperature are 30,000 psi and 1200 K, respectively. These figures show that the overall pressure distribution within the annulus is not very sensitive to the choice of friction factor, which is an a posteriori justification for the assumption of a constant friction factor throughout the annulus.

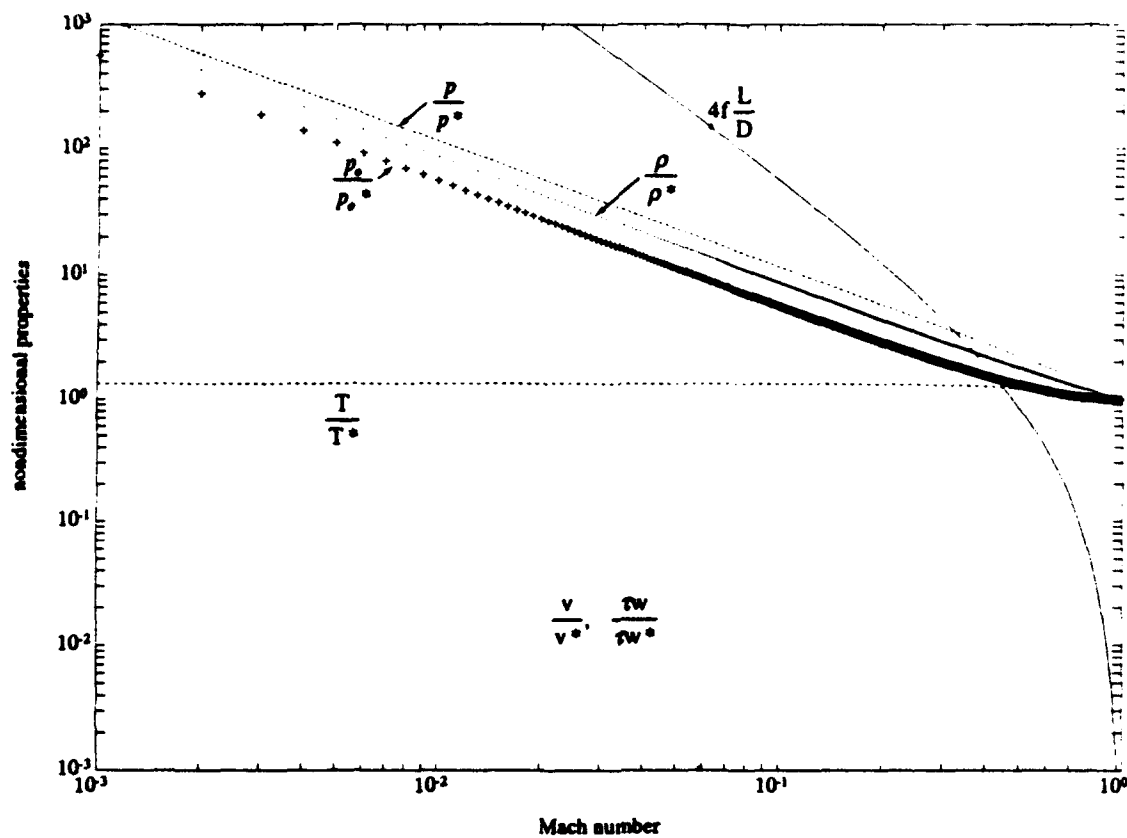
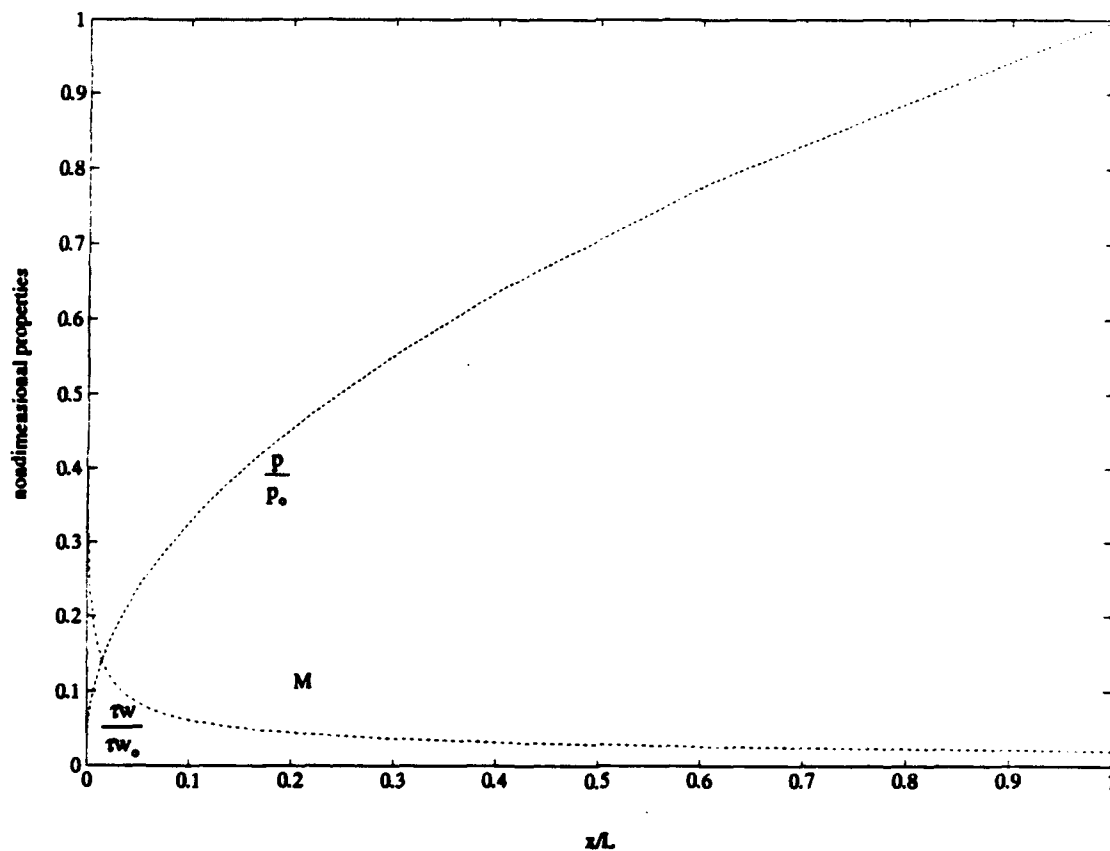
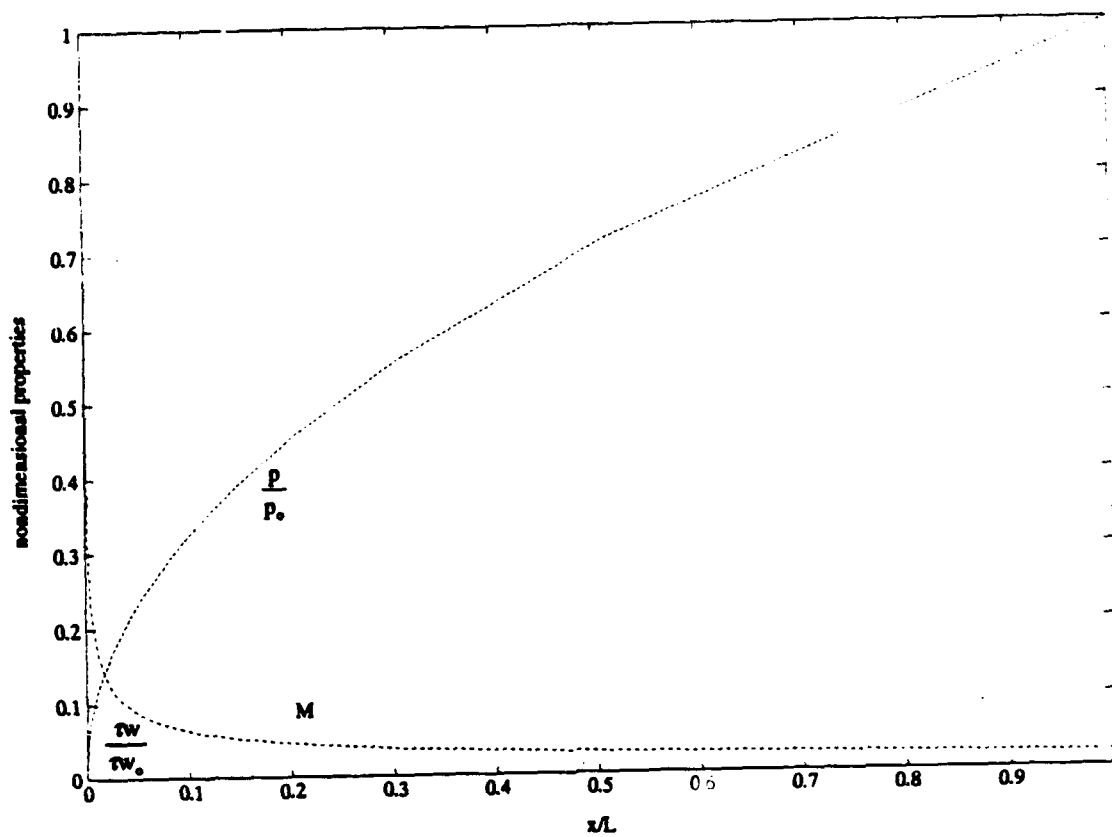


Figure 10. Variation of Gas State on Fanno Line

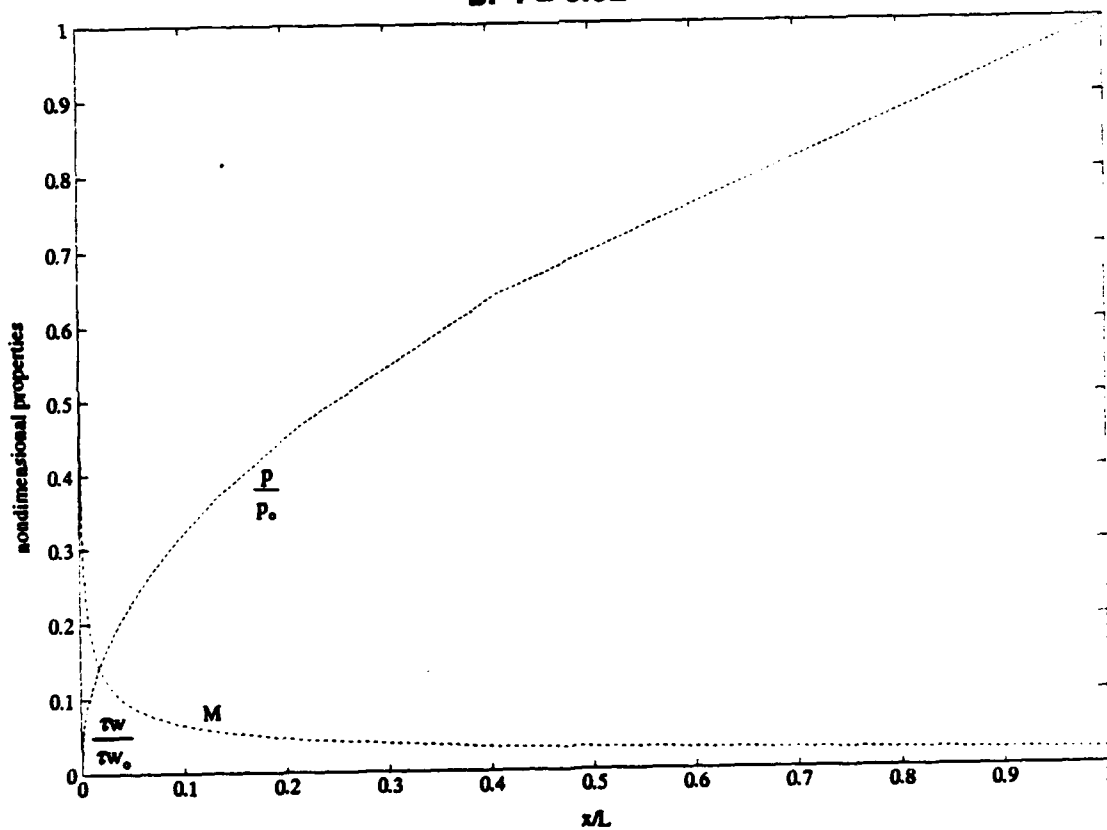


a. $f = 0.01$

Figure 11. Pressure and Mach Number Axial Distribution



b. $f = 0.02$



c. $f = 0.08$

Figure 11. Pressure and Mach Number Axial Distribution (Cont.)

It is difficult, without resorting to numerical gas simulations, to study the question of how the pressure distribution evolves in a dynamic sense. If the period of the pressure variations is rather long compared to the time required for sound to pass the length of the sabot (about 35 μ s), then the distribution behaves in a quasi-steady state. In this case, the time-dependent pressure distribution follows from the instantaneous pressure at the base. In situations in which this is not the case, a gross approximation is used in which the normalized distribution is the same as that used in the steady-state case but the p_o is taken at a time offset by the time required for the sound to reach the particular axial location.

3.4.3.2 Annulus Pressure Fluctuations

Based on these compressible expressions, the Reynolds number of the annulus flow ranges from 700 to 2000, and it is anticipated that the flow is either laminar or transitional. Thus, the main cause of the pressure fluctuations within the annulus flow will be due to shock waves that reflect off the base of the projectile. Knowing the strength of these impinging shock waves and the appropriate shock tube formulas, it is possible to relate the pressure fluctuation levels in the annulus to those occurring at the base of the projectile. A more detailed treatment of the shock tube problem and relevant formulas may be found in Anderson (1982).

3.5 Side-Wear Model

Due to the very short duration of the flight within the barrel, the heat generated by friction at the interface diffuses only slightly into the interior of either the sabot or the barrel. The diffusion time scales of Lexan, relative to the duration of the test, are near 10^{-7} , and for steel the ratio is much larger, 10^{-2} , but still quite small. Since little heat is dissipated, much of the friction energy goes into heating a thin surface layer of the sabot to its melting temperature and later to promoting the burning of the surface. One would expect that after an initial rise to the melting temperature, a pseudo-steady state will exist in which the heat that is not lost to dissipation goes into melting and ablating the sabot. The heat flows slightly into the sabot, and the new cool portion of the barrel wall is continually introduced to the interface. In the coordinate frame fixed to the sabot, this action will produce a thin thermal boundary layer in the barrel wall. This boundary layer grows from zero to some small thickness at the sabot base. Assuming such a steady state, we provide without proof the relation for the rate of ablation of the sabot \dot{r}_s :

$$\dot{r}_s = \frac{\mu \sigma v - \rho_b c_b v_b (T_m - T_o)}{\rho_s c_s (T_m - T_o) + \rho_s H_s} \quad (38)$$

Here the subscript b indicates barrel wall and the s is for sabot. The expression is derived from an energy principal. The first term in the numerator is the heat energy flux generated by the friction, and the second term is the energy flux dissipated into the barrel. The first term in the denominator is the

heat dissipated into the sabot, and the last term is the heat removed by the melting and ablating. The barrel velocity term derives from the boundary-layer growth and is given as

$$v_b(x) = \sqrt{\frac{\alpha_b v}{x\pi}} \quad (39)$$

where v is the speed of the sabot, x is the distance from the top of the sabot, and α_b is the thermal diffusion of the barrel wall. Although no data are available for the friction coefficient at these high speeds, Bowden and Tabor (1964) found that at speeds of up to 1800 fps, the friction between nylon and steel behaved as

$$\mu = 1.7 v^{-0.4} \quad (40)$$

A generalization of this expression will be used here:

$$\mu = \begin{cases} \mu_0 \left(\frac{v_0}{v} \right)^b & v > v_0 \\ \mu_0 & v \leq v_0 \end{cases} \quad (41)$$

This provides the same trend as that given by Bowden and Tabor but introduces a notion of the static coefficient of friction.

Finally, in this Phase I effort we have implemented only the primary term in the rate of ablation expression:

$$\dot{r}_s = \frac{\mu \sigma v}{\rho_s H_s} \quad (42)$$

That is, the sabot immediately begins to melt and all the heat generated by the friction goes into melting and ablating the sabot.

4. FINITE ELEMENT MODEL

4.1 FEAMOD Overview

FEAMOD is an inhouse finite element analysis software system developed over the past ten years at QUEST Integrated (Mueller, 1986). It is intended as a very flexible finite element analysis package that can be easily modified to include new elements. More than 29 element types are available, including elements for:

- (1) Isotropic, orthotropic, and anisotropic elasticity.
- (2) Elastic/plastic deformation with finite strain and incremental loading for large deformations with general yield functions and potentials.
- (3) Isotropic and orthotropic heat transfer.
- (4) Navier-Stokes laminar fluid flow.
- (5) Porous media flow.

FEAMOD comes equipped with a macro language to control and tailor the solution algorithm to specific applications. Special macros are available for time integration and incremental loading. FEAMOD also has translators for SUPERTAB, PATRAN, and NISA for interactive, menu-based, graphical pre/post processing. The software also includes state-of-the-art, preconditioned, sparse-matrix incore solvers suitable for both serial and vector processors (Oppe et al., 1988). FEAMOD has been successfully applied to a wide variety of engineering problems and will be used as the base program in this study.

The finite element method used in FEAMOD is that of Zienkiewicz (1977) and Bathe (1982), and the particular implementation found in FEAMOD is fully discussed in Mueller (1986). To support the further discussion, we describe here the result of the finite element discretization of the momentum equation:

$$\mathbf{r} = \mathbf{R} - \mathbf{P} - \mathbf{C}^T \mathbf{F} - \mathbf{M} \ddot{\mathbf{u}} = 0 \quad (43)$$

subject to constraints

$$\boldsymbol{\rho} = \boldsymbol{\Delta} - \mathbf{C} \mathbf{u} - \mathbf{D} \mathbf{F} = 0 \quad (44)$$

Here \mathbf{u} , \mathbf{R} , \mathbf{P} , and \mathbf{F} are, respectively, nodal displacements, applied boundary nodal forces, internal nodal forces, and nodal forces (Lagrange multipliers) induced to enforce the contact constraints. \mathbf{C} is the constraint operator, and \mathbf{D} is a diagonal matrix operating on the nodal constraint forces. $\boldsymbol{\Delta}$ is an initial nodal gap between contacting surfaces, and \mathbf{r} and $\boldsymbol{\rho}$ are the out-of-balance nodal residuals in the momentum and the constraint equations. The nodal displacement \mathbf{u} is based on the inertial frame, as discussed in Section 3.1.

4.2 Numerical Time Integration Method

FEAMOD offers two choices for the integration scheme: the central difference method, which is explicit with a step size stability limit of the time required for the sound wave to traverse the element, or the Wilson- θ method, which is implicit and is absolutely stable. An aluminum 1-in. slug with 25 elements across the slug will have an explicit time step size limit of near $0.1 \mu\text{s}$ to remain stable. If the slug is 3 in. long, then the elastic wave will travel from the base to the top in about $15 \mu\text{s}$ or about 150 steps. This is not an inordinately large number of steps if one is interested in phenomena in which the wave traverses and reflects only a few times. But, if one is studying the physics over the length of the shot, approximately 3 ms, the explicit scheme will not be efficient. For these reasons, we have chosen the implicit Wilson- θ method for this study. The drawback to the implicit scheme is that an algebraic system of equations must be inverted. The implicit time stepping will require repeated solutions to a linear system of equations, and the cost of these solutions must be minimized. More discussion of this point will follow under the linear solver section.

The Wilson- θ method assumes that the acceleration is a linear function in the time interval $(t, t + \theta\Delta t)$. With this assumption, the change in the displacement and the change in the velocity can be evaluated. The scheme used here has been modified to incorporate the constraint equations with the assumption that the constraint forces also behave linearly over this interval. The momentum and constraint equations are evaluated at time $t + \theta\Delta t$, and the change in the displacement and the constraint forces over this interval may be solved via Newton's iteration

$$\hat{\mathbf{K}}\delta\mathbf{u}^o + \mathbf{C}\delta\mathbf{F}^o = \mathbf{r}(t + \theta\Delta t) \quad (45)$$

$$\mathbf{C}\delta\mathbf{u}^o + \mathbf{D}\delta\mathbf{F}^o = \mathbf{p}(t + \theta\Delta t) \quad (46)$$

Here $\hat{\mathbf{K}}$ is the effective stiffness matrix. The interpolation of the displacement, velocity, and acceleration to the new time $t + \Delta t$ is described in Bathe (1982), and the nodal constraint forces at the new time are simply linear interpolations of the nodal constraints at times t and $t + \theta\Delta t$.

4.3 Linear Solver

FEAMOD offers two types of solvers. One is the standard direct solver based on Gaussian elimination and on a matrix in skyline storage (Zienkiewicz, 1977). Since the elimination is without pivoting, it is important that any nodal constraint forces be arranged after the nodal displacements to help any ill conditioning resulting from the zero entries in the D matrix [Equation (44)]. In two dimensions with $n \times n$ quadratic elements, it can be shown that the direct solver will require about $5n^4$ operations to eliminate, $4n^3$ operations to forward and back solve, and use about $4n^3$ words of storage. As n grows, the operations and storage rise dramatically. In three dimensions, the problem is even more severe. The elimination is the most costly and is required only once for linear problems. For nonlinear problems, the computation of the stiffness matrix and its elimination may be required as much as once

each time step. The backward and forward elimination is carried out at least once a time step regardless of linear/nonlinear.

To reduce this cost, FEAMOD offers an iterative solver based on a preconditioned conjugate gradient method (Oppe et al., 1988). Only the nonzeros of the matrix are stored along with some pointing arrays. For the same $n \times n$ quadratic elements the operations to solve a linear equation in k iterations are about $50kn^2$ and the storage is about $50n^2$ words. Generally the number of iterations is much less than n . This implies that, for sufficiently large problems, the iterative solver will be much more efficient in terms of both computer speed and storage. Experience shows this break-even point to be around $n = 10$ or a total of 100 quadratic elements for nonlinear problems. There is, however, a restriction on the iterative solver. The solver is guaranteed to converge only if the matrix is symmetric positive definite. With the Lagrange multipliers included in the problem, such a condition is not met.

To avoid this problem, a new conjugate gradient solver that treats the Lagrange multiplier terms has been formulated and coded. The method uses a preconditioning similar to that of the previous method but includes terms based on the penalty method to handle the Lagrange multiplier. Since this penalty is only in the preconditioner and is not reflected in the solution itself, we expect no stability problems. Indeed, in stand-alone tests, this new solver appears to perform as well on problems with multipliers as the old method does on problems without the multipliers. However, because of time limitations, this new solver has not been implemented in the FEAMOD structure. For this reason, the contact friction element has been used only in conjunction with the direct solver.

4.4 Discrete Constitutive Model

The finite element model must evaluate the stress at the current time at the Gauss points. Applying a second-order-accurate implicit scheme to the viscoelastic-viscoplastic law, Equation (26), the stress at time $t + \theta\Delta t$ may be written as

$$\sigma_i^{t+\theta\Delta t} = \sigma_i^t + D_{ij} \left\{ \Delta \epsilon_j + \tau \Delta \dot{\epsilon}_j - \theta \Delta t \Lambda \dot{\epsilon}_j^p \left[\frac{1}{2} (\sigma_i^{t+\theta\Delta t} + \sigma_i^t) \right] \right\} \quad (47)$$

This implicit algebraic equation is solved using a Newton's iteration. The finite element must also evaluate the tangent stiffness matrix at each Gauss point. Differentiating Equation (47) gives an implicit linear equation for the tangent stiffness:

$$\frac{\partial \Delta \sigma_i}{\partial \Delta \epsilon_j} = D_{ij} \left(1 + \frac{3\tau}{\theta \Delta t} \right) - \frac{\theta \Delta t}{2} D_{ik} \frac{\partial \dot{\epsilon}_k^p}{\partial \sigma_m} \frac{\partial \Delta \sigma_m}{\partial \Delta \epsilon_j} \quad (48)$$

4.5 Boundary Conditions

4.5.1 Pressure Loading

The nodal boundary load, due to the gas pressure acting on the sabot base or sides, is given by the usual inner product of the pressure stress and the shape functions:

$$P_i(t) = \int_{\partial\Omega} p(t, \mathbf{x}^o) \mathbf{n} \cdot \mathbf{N}_i \, ds \quad (49)$$

The pressure acting on the base is assumed homogeneous, while on the sides the pressure is taken from Equations (31) and (32). Because of the spatial dependence of these side pressures, the inner products are carried out on an element written explicitly for this effort.

4.5.2 Friction Model

In the literature, the free/contact friction boundary conditions are generally handled by either a Lagrange multiplier approach or using a penalty method (stiff element method). The Lagrange multiplier approach offers a more general treatment of the problem but calls for the solution of additional unknowns. The penalty method does not introduce any additional unknowns, but the penalty poorly conditions the matrices to be inverted, and a loss of precision is expected. With single precision arithmetic and large matrices, the penalty method may have potential stability problems. After some initial experimentation (see ELMT12 in Appendix A) with the penalty approach, we elected to take the more rigorous and general Lagrange multiplier approach and accept the additional work to implement this approach. This decision also implied that the current iterative solver would not be applicable and would require a modified formulation.

The free/contact friction boundary conditions are enforced using a Lagrange multiplier technique with the constraints being the normal and tangential gaps between a boundary nodal point and the barrel wall. The multipliers are the nodal forces required to impose the boundary displacement constraint. The development follows Katona (1983) except that the constraints are dynamic. With the normal and tangential gaps defined for node i as

$$\delta_{ni} = R - r_{ni} - u_{ni} \quad (50)$$

$$\delta_{ti} = -u_{ti} \quad (51)$$

The nodal contributions to the constraint residuals and the C and D matrices and any explicit boundary loads \mathbf{P} for each contact state are as given below.

Sticking contact

The Lagrange multipliers at node i , F_n and F_t , are both nonzero and defined by the constraints

$$\rho_n = \delta_n = 0 \quad (52)$$

$$\rho_t = \delta_t = 0 \quad (53)$$

$$C_i = \begin{bmatrix} 1 & 0 \\ 0 & 1 \end{bmatrix} \quad D_i = \begin{bmatrix} 0 & 0 \\ 0 & 0 \end{bmatrix} \quad P_i = \begin{Bmatrix} 0 \\ 0 \end{Bmatrix} \quad (54)$$

Sliding contact

The Lagrange multiplier in the normal direction is defined by the normal constraint. The magnitude of the tangential constraint force is the frictional force with a sign defined by the local velocity. The treatment of the friction is explicit. In other words, the tangential forces of the current step are related to the friction force based on the normal force of the previous step.

$$\rho_n = \delta_n = 0 \quad (55)$$

$$\rho_t = \mu \operatorname{sign}(v_t) F_n^* - F_t = 0 \quad (56)$$

$$C_i = \begin{bmatrix} 1 & 0 \\ 0 & 0 \end{bmatrix} \quad D_i = \begin{bmatrix} 0 & 0 \\ 0 & 1 \end{bmatrix} \quad P_i = \begin{Bmatrix} 0 \\ -\mu \operatorname{sign}(v_t) F_n^* \end{Bmatrix} \quad (57)$$

Free

The normal and tangential forces are zero.

$$\rho_n = -F_n = 0 \quad (58)$$

$$\rho_t = -F_t = 0 \quad (59)$$

$$C_i = \begin{bmatrix} 0 & 0 \\ 0 & 0 \end{bmatrix} \quad D_i = \begin{bmatrix} 1 & 0 \\ 0 & 1 \end{bmatrix} \quad P_i = \begin{Bmatrix} 0 \\ 0 \end{Bmatrix} \quad (60)$$

The logic for moving from one state to another is shown in the decision matrix of Table 3. Some of the entries in the matrix are not self-evident. The decision matrix does not allow a state to go directly from a free to a sticking contact. Also, if the body is in sliding contact at the current time but the direction of the motion has changed, it is assumed that the body must go into sliding contact.

Table 3. Free/Contact Decision Matrix

Next time step $k+1 \rightarrow$ Current time $k \downarrow$	free	sliding contact	sticking contact
free	$\delta_n > 0$	$\delta_n \leq 0$	
sliding contact	$F_n < 0$	$F_n \geq 0, u_z^k u_z^{k-1} > 0$	$F_n \geq 0, u_z^k u_z^{k-1} \leq 0$
sticking contact	$F_n < 0$	$F_n \geq 0, F_s > \mu F_n$	$F_n \geq 0, F_s \leq \mu F_n$

As a final note, the contact forces have been normalized with a spring constant so that they have the same units as displacement. In subsequent numerical tests, a stability problem arose when the sabot came in recontact with the rigid barrel wall. This problem was effectively eliminated by allowing the barrel wall to have a large, but not infinite, spring constant.

4.6 Side-Wear Model

The expression for the rate of ablation involves the local normal stress acting on the sabot due to the barrel wall constraints. The equivalent finite element representation of Equation (42) is

$$M_y \dot{r}_j = \int_{\partial\Omega^c} \mu \sigma v_i N_i \, ds \quad (61)$$

with the mass matrix simply the inner product of the shape functions

$$M_y = \int_{\partial\Omega^c} \rho H N_i N_j \, ds \quad (62)$$

Now the right-hand side can be related to the nodal normal Lagrange multiplier giving

$$M_y \dot{r}_j = \mu_i F_n v_i \quad (63)$$

The system is solved by first-order explicit time integration, and a lumped mass is used to facilitate the computations. These expressions are included in the contact friction element.

5. EXAMPLE SIMULATIONS AND RESULTS

To test and demonstrate the different capabilities of the finite element model, two different geometries and loading conditions are simulated. In the first simulation set, a simplified model of the pyro model and a Lexan sabot is analyzed. In the second set, a Lexan slug, undergoing loadings similar to that in an impulsive pressure test apparatus under development in a parallel project (Kollé, 1991). These tests document the evolution of the total finite element model over the course of the study.

5.1 Aluminum Pyro Model/Lexan Sabot

The geometric model is a simplified representation of the pyro model and a Lexan sabot. The dimensions and outline of the geometric model are the same, but the pyro model is considered to be a single piece of aluminum. In reality, the pyro model is made up of many separate parts and materials and contains some gaps between parts. We expect the finite element model will tend to underpredict the true stress in the pyro model because of the additional bulk. In all the following cases, the interface between the aluminum and the Lexan is frictionless and allowed to slip. It is also assumed that the sabot remains in contact with the pyro model and the barrel wall for the duration of the test.

In the initial simulations, the barrel wall is also assumed to be frictionless, allowing the usual boundary restraint conditions offered with FEAMOD to be applicable. The normal constraint between the sabot and the pyro model was handled by a multipoint constraint (MPC). At the base of this interface, the MPC forces the axial displacement of nodes on either side of the interface to be the same. On the side interface, the MPC enforces the radial displacement to be the same. This incurs a slight error, as the side is shifted from vertical by about 10° , but simplifies the solution algorithm because interfaces aligned with cylindrical coordinates do not require the solution of Lagrange multiplier constraints.

The model consisting of 413 elements and 1368 nodes for a total of 2736 degrees of freedom is shown in Figure 2. A fine grid is used near the large cavity to resolve the large stress gradients. The elastic model behaves properly if the grid is coarse in these regions, but the nonlinear models fail to converge if these regions are not resolved. This will be true of any regions containing reentrant corners or cavities. This finite element model requires about 1.2 Mbytes using the iterative solver and 5.1 Mbytes with the direct solver. The generation of the geometry, nodes, elements, and boundary restraints and constraints is carried out with the NISA II preprocessor. The NISA file is then translated into the SUPERTAB universal file, which is the standard FEAMOD file. The FEAMOD output file is translated back into a NISA file for postprocessing. The storage requirements of the direct solver are dependent on the numbering scheme. NISA does not offer a utility for renumbering to minimize the storage, like some packages such as SUPERTAB. For this reason, the storage for the direct solver is higher than its optimal value.

The load history on the sabot base assumes a linear rise of pressure from 0 to 38 ksi in about 150 μ s and then a slower linear drop to 24 ksi in 230 μ s for a total simulation period of 380 μ s. This is the

duration and magnitude of a typical spike produced by a shock wave reflecting off the sabot, as predicted by the AEDC launch code.

Initially the entire body is at rest. The initial stresses within the model are related to the slight 1-mil fit of the sabot and the barrel wall. These initial stresses are predicted by first executing the finite element code with a macro command structure for static loading, representative of placing the model/sabot into the bore of the barrel.

5.1.1 Elastic/Frictionless Barrel

The model predicts that both the pyro and the sabot remained almost entirely in compression the entire duration of the spike and the maximum compression loads occurred near the peak loads. The von Mises stress on an exaggerated deformation plot is shown in Figure 12. The stresses are very high near the cavity/Lexan/aluminum junction and also near the side wall/base of the aluminum. The Lexan is severely strained, especially near the cavity, with strains over 10%. It appears that for the bulk of the Lexan, the von Mises stress is between 10 and 20 ksi. This indicates that most of the Lexan would not yield if the compressive strength at these strain rates (500 s^{-1}) is near 20 ksi. As expected, simulations in which the sabot is unconstrained produce much higher von Mises stresses, but such an unconstrained compression is not likely to occur. If the sabot erodes away, then the gas pressure leaking into the side will serve to constrain the model.

No significant tensile loads appear in the download. The base of the aluminum model experiences some tensile warping, but this is small, less than 10 ksi. The period for which an elastic wave propagates from the base to the top of the sabot is about $50 \mu\text{s}$. The time for the elastic wave to propagate across the aluminum pyro model is near $15 \mu\text{s}$. These times are rather short compared to the $230 \mu\text{s}$ drop in the pressure spike, and so the model behaved almost quasi-statically.

The pressure spikes are a result of shock waves impinging and reflecting off the base of the sabot. Since these shock waves are on the order of a few molecules thick, there is reason to believe that the upsides of these pressure spikes are of very short duration. Numerical simulations of the gas dynamics will inevitably smear the shock. The question is whether the downside, or a portion of the downside, is just as steep. A careful examination of the results of the AEDC launch code is shown in Figure 3. This figure shows as little as nine points in a typical spike, so there may be some numerical damping on the downside (if each point is a time step). If the downsides are steeper than predicted by the gas model, then what effect will this have on the dynamics of the model/sabot? To examine the relation between tensile stresses and the ratio of the download time to the time for sound to cross the model/sabot, another elastic case was conducted in which the duration of the spike is cut in half and by fourth. Significant tensile waves appeared in both simulations with the largest tensile stress in the aluminum. Figures 13a and 13b show the axial stress contours at a time in which the tensile stresses peak in the simulation for pressure spike durations of 190 and $95 \mu\text{s}$. The tensile stress in the aluminum is near the maximum static tensile strength. Viscoelastic damping will reduce these loads

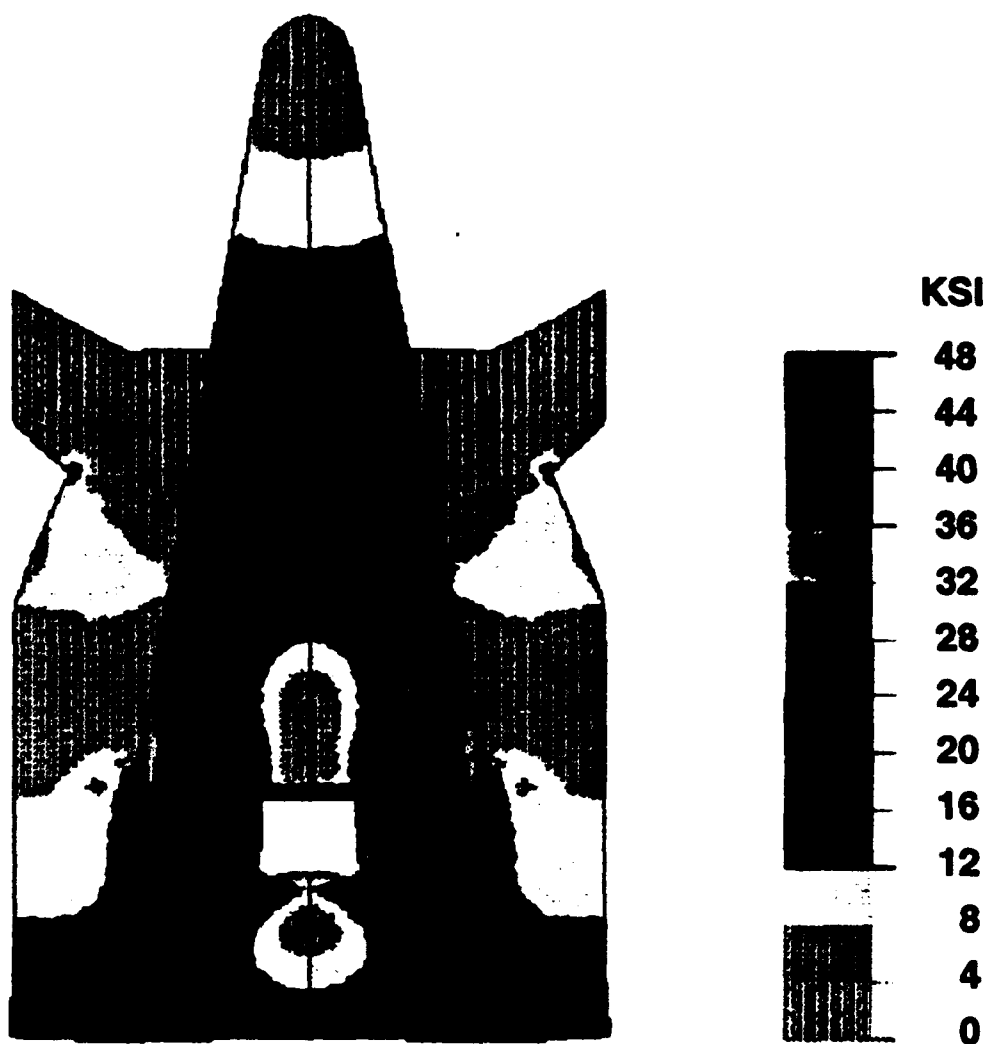
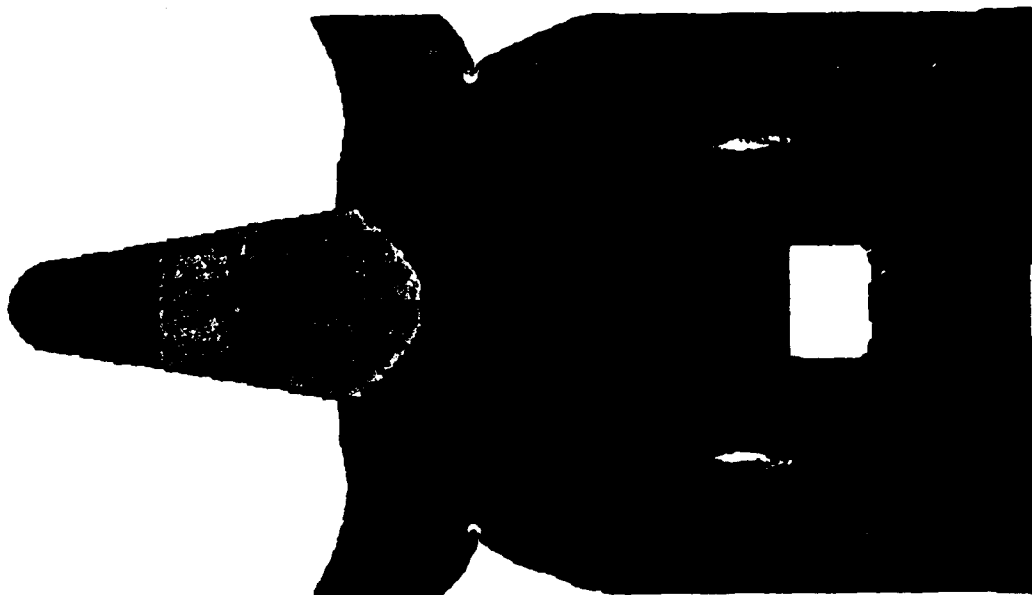
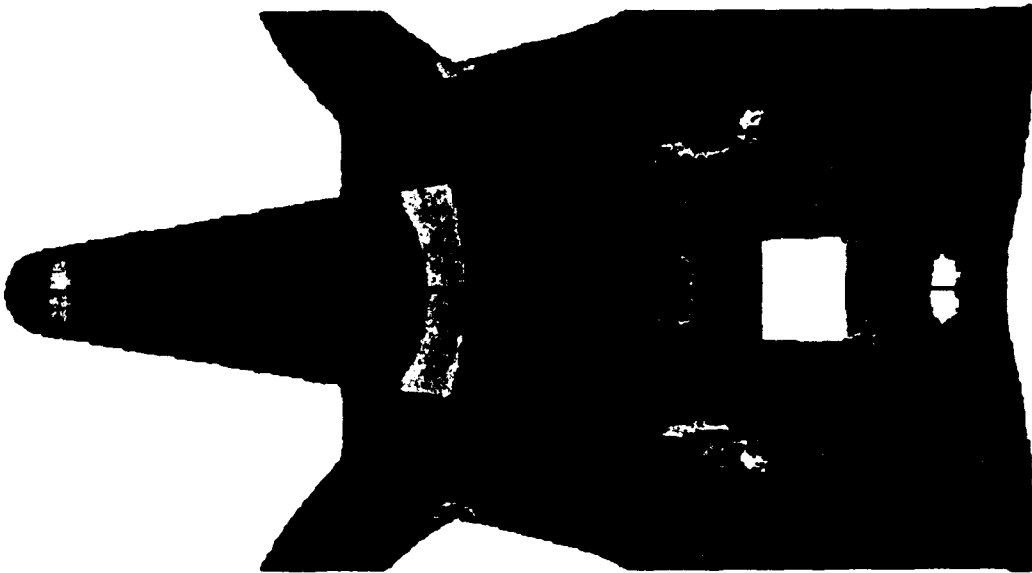


Figure 12. Maximum Load Von Mises Stress Contours (Elastic Simulation)



a. Peak tensile stress contours for pressure spike duration of 190 μ s



b. Peak tensile stress contours for pressure spike duration of 95 μ s

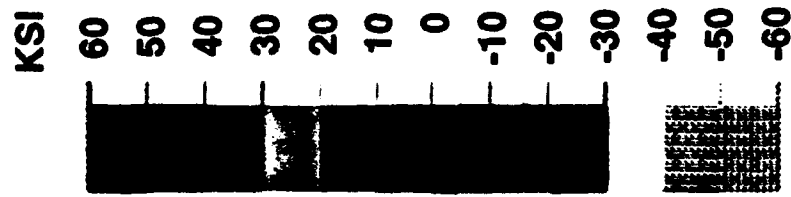


Figure 13. Peak Tensile Stress Contours for Pressure Spike Duration

somewhat, but the model demonstrates that the appearance of these tensile loads is sensitive to the duration of these spikes.

5.1.2 Elastic-Viscoplastic/Frictionless Barrel

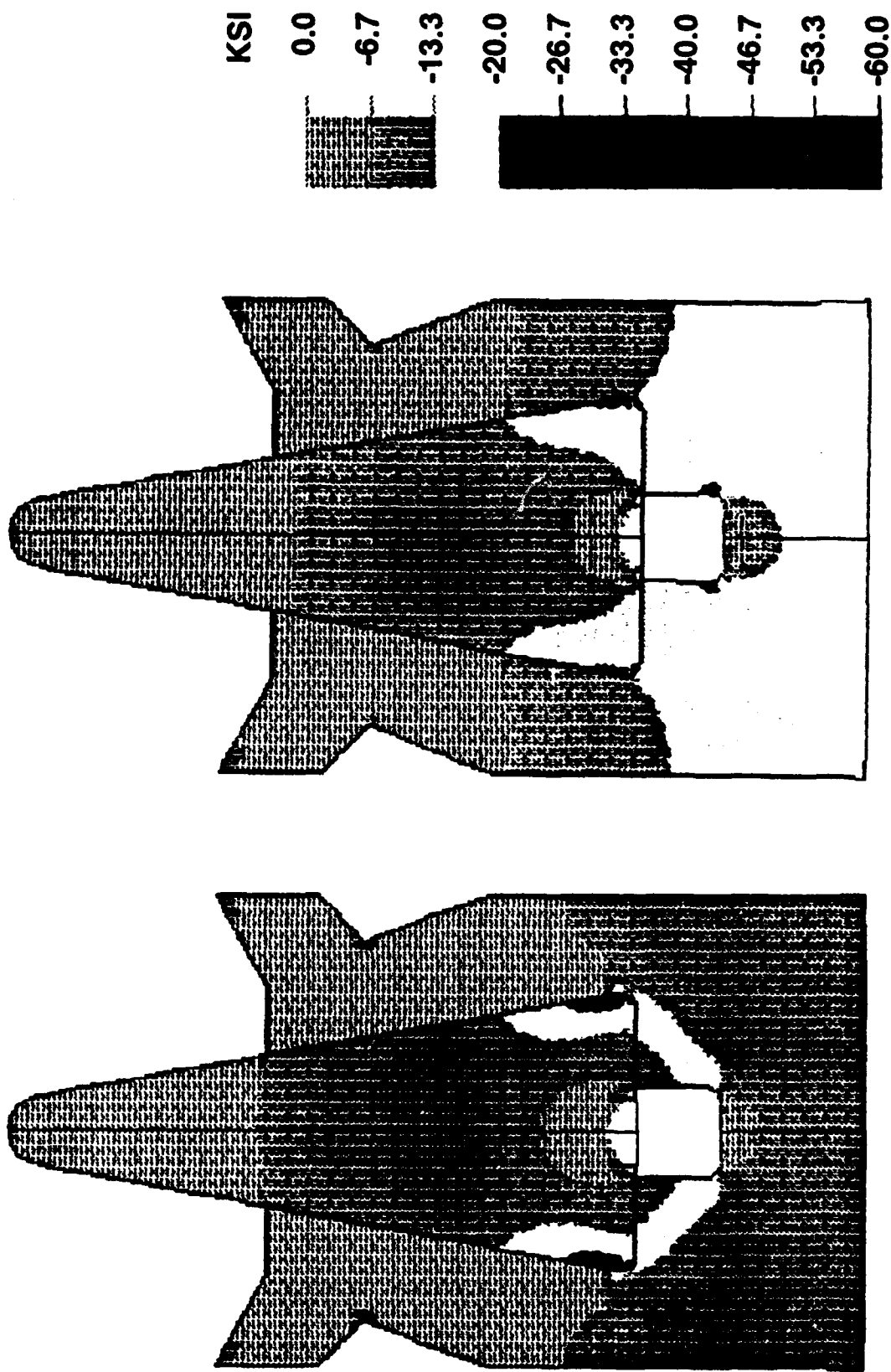
To examine the effects of adding viscoplasticity and geometric nonlinearities, the simulations are repeated with the nonlinear model. To give an indication of the dynamic nature of the stresses, the axial stresses at equal intervals of time are shown on an exaggerated deformation plot in Figures 14a through 14n. Here we see how in the initial stages the stress field is uniform, but then it becomes quite complicated as the Lexan and sabot interact. In Figure 14b we see how the stress wave has propagated much faster in the aluminum than in the Lexan. The results of the elastic-viscoplastic model agree qualitatively with the elastic runs, but the maximum stresses tend to be reduced as the yielding redistributes the load. The contours of plastic work, shown in Figure 15a through 15k show how the failed region grows in the vicinity of the cavity. Most of the yielding has occurred shortly after the time of maximum pressure. The maximum contour is set to the approximate plastic work at failure in compressive uniaxial static tests so that the white region has failed. The Lexan is expected to maintain its integrity because the failed region does not span the diameter.

5.1.3 Elastic/Friction Side Wall

In this simulation, the friction between the barrel and the sabot and the sabot and the pyro model is considered. The coefficient of friction between the barrel and the sabot is 0.5. This coefficient is a severe test of the robustness of the friction model, but it is probably a large overestimate of the actual friction. The coefficient of friction between the sabot and the pyro model is 0.2. The contact and friction are determined via one-dimensional friction elements along the interfaces, but it is assumed that the interfaces are always in slipping contact. Because no sticking contact is included, the initial pressure applied at the base is about 2 ksi to overcome the friction of the lip seal. Unlike the previous calculations, the 13-mil lip seal is considered in these friction simulations.

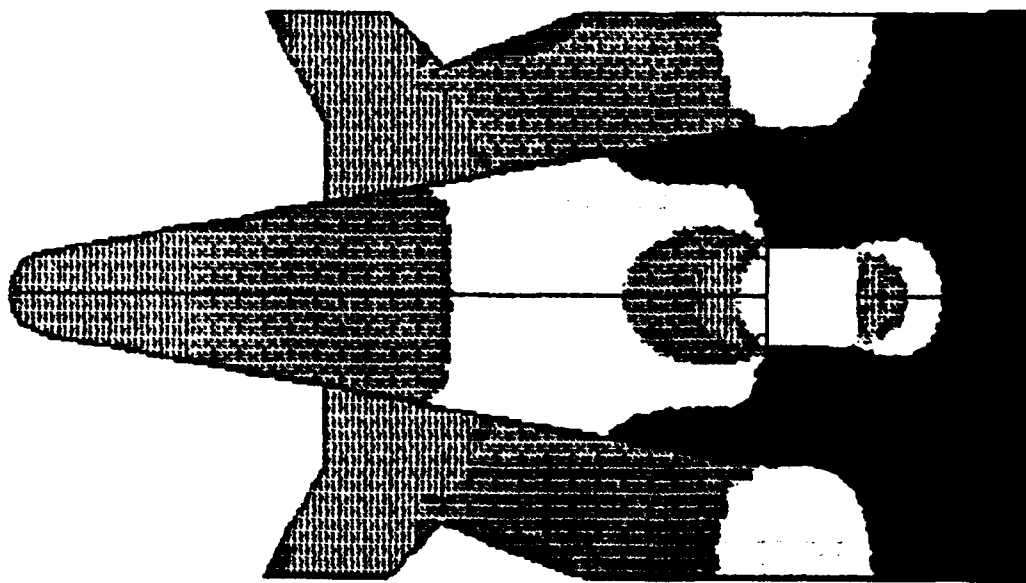
In Figure 16, the von Mises stress contours at the time of maximum pressure are shown in an exaggerated deformation plot. The friction tends to increase the overall magnitude of the von Mises stresses in the sabot. The warping of the sabot base, because of the action of friction, is evident in the plots. The lip seal at the base of the sabot appears to be skewed, but this is an artifact of exaggerating the severe deformation of the lip. In reality, all points at the barrel interface are at the same radius.

This large friction also affects dramatically the acceleration of the center of mass. The acceleration as a function of time is plotted in Figure 17. The acceleration for a frictionless barrel, which follows from the pressure loading history, is also shown for comparison. The friction acceleration exhibits periodic oscillations as the compressive stress waves move through the sabot.

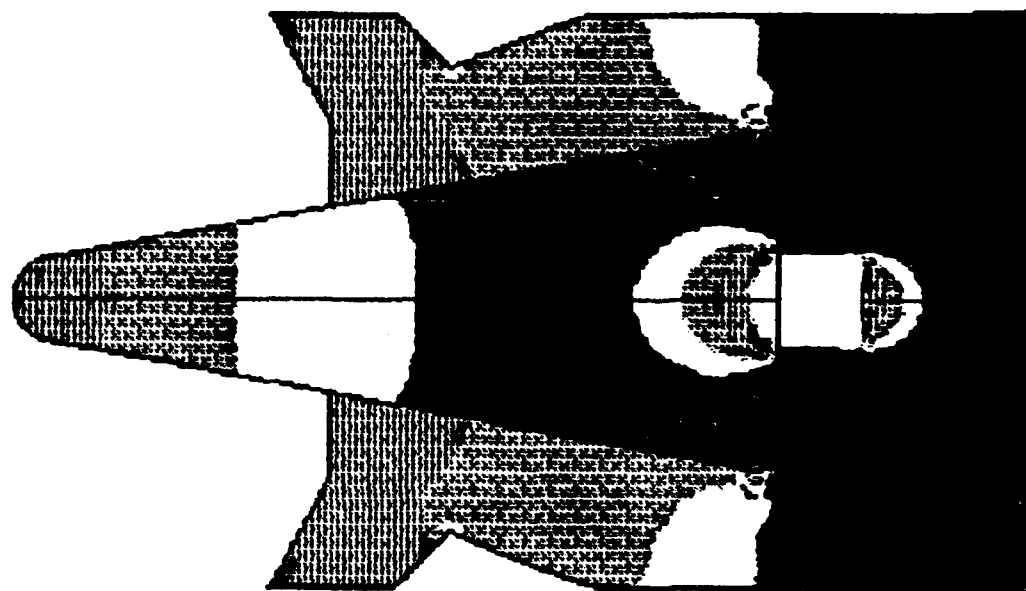


a. $t = 50 \mu s$ b. $t = 75 \mu s$

Figure 14. Axial Stress Contours (Elastic-Viscoplastic Model)



c. $t = 100 \mu s$



d. $t = 125 \mu s$

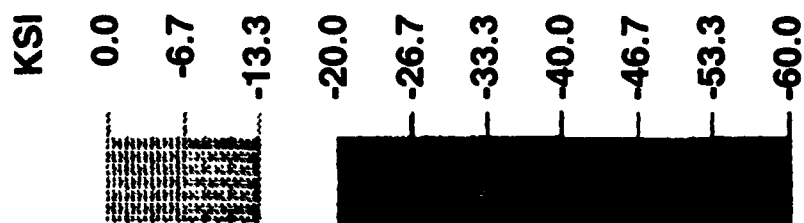
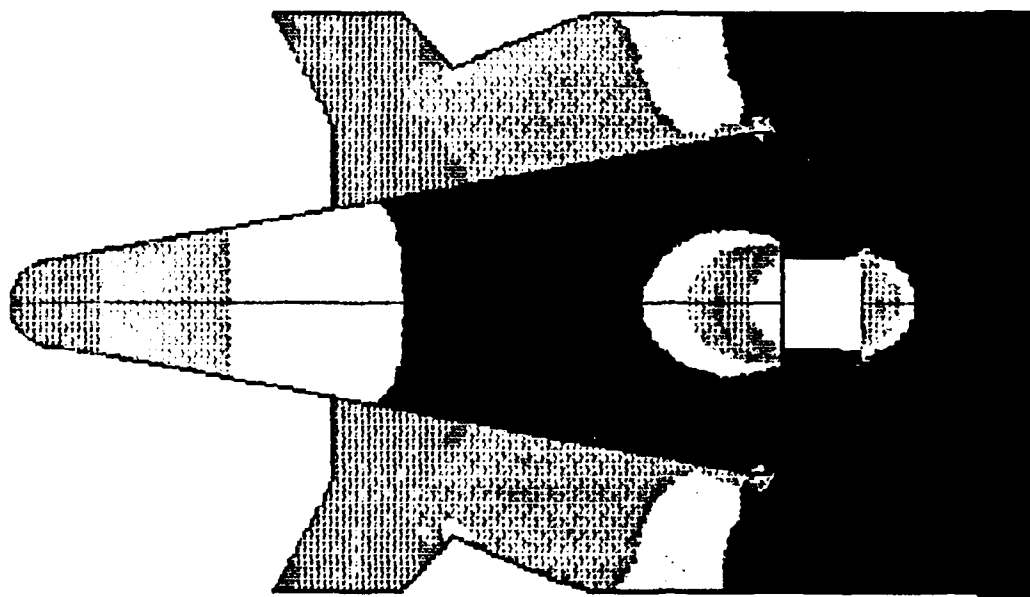
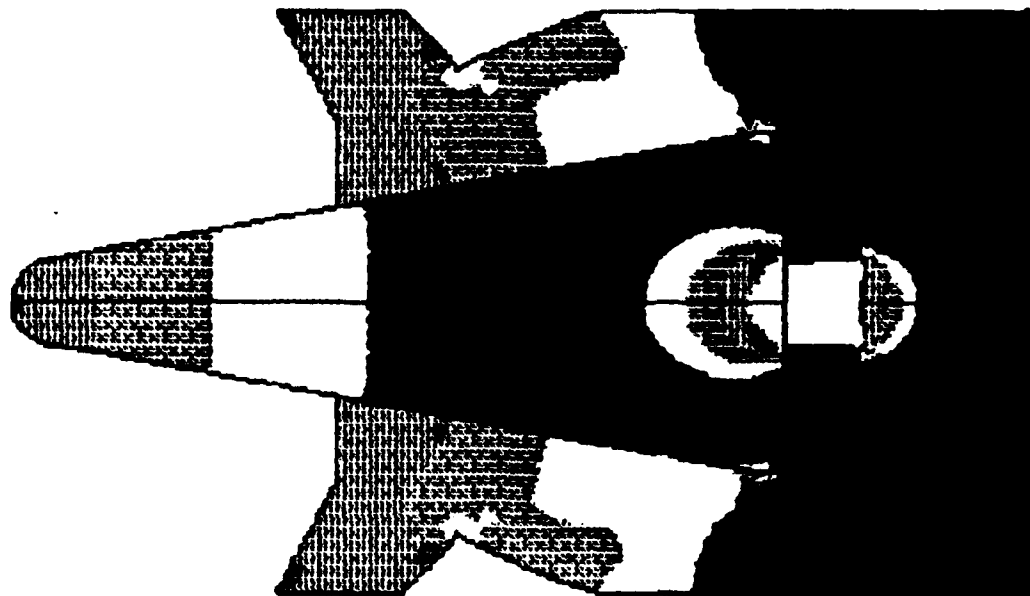


Figure 14. Axial Stress Contours (Elastic-Viscoplastic Model) (Cont.)



e. $t = 150 \mu s$



f. $t = 175 \mu s$

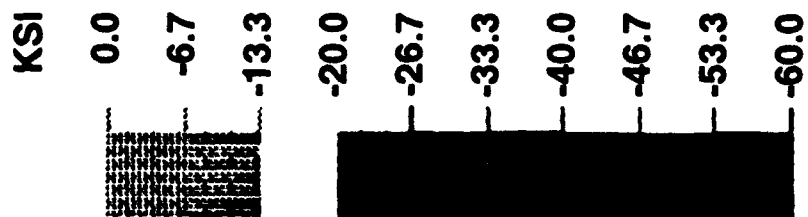
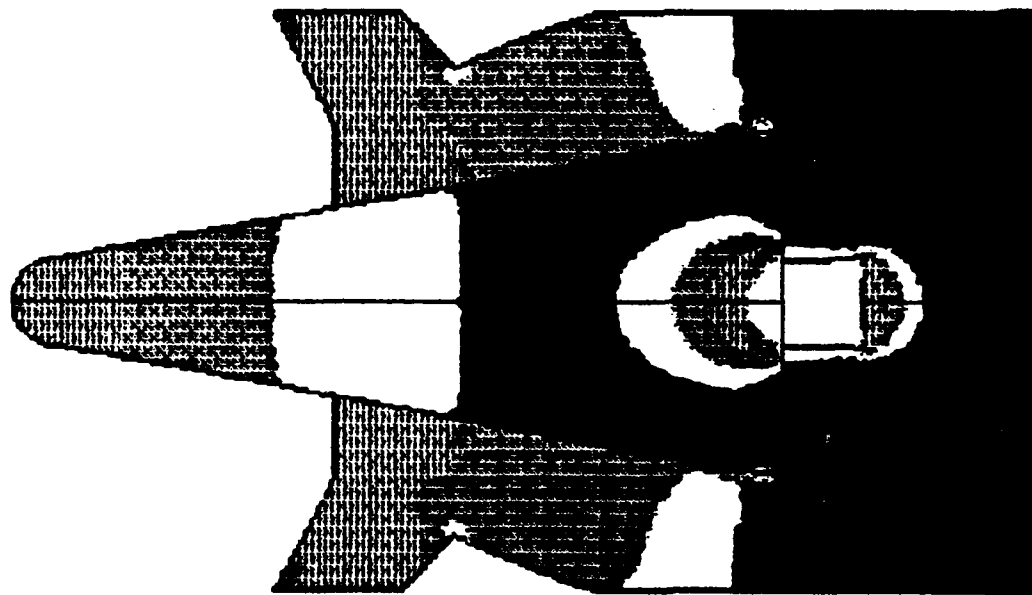
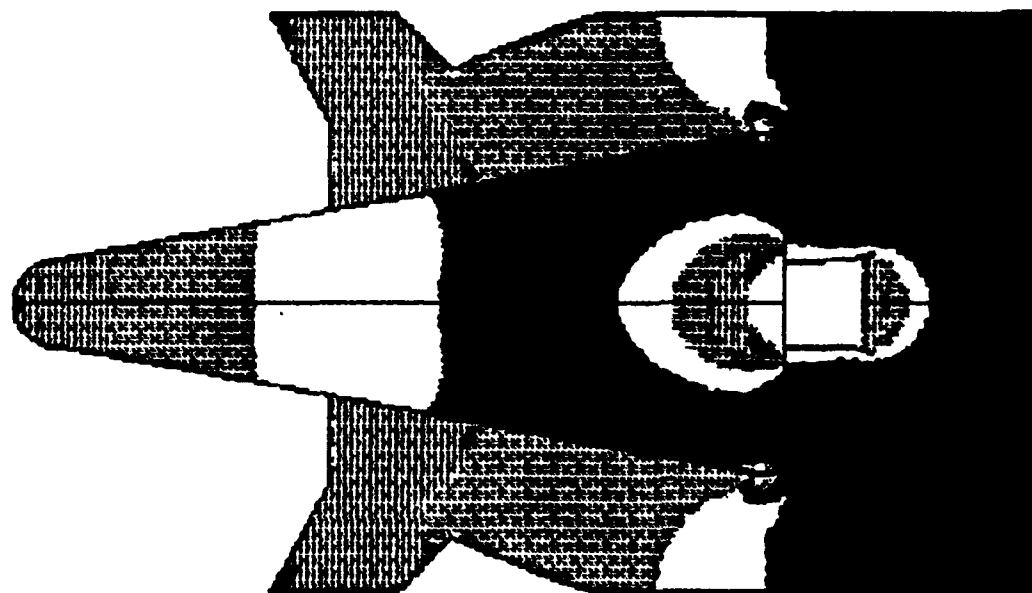


Figure 14. Axial Stress Contours (Elastic-Viscoplastic Model) (Cont.)



g. $t = 200 \mu s$



h. $t = 225 \mu s$

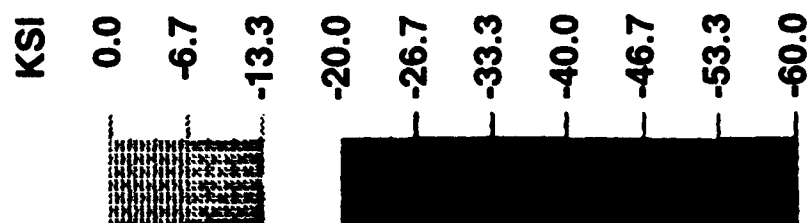


Figure 14. Axial Stress Contours (Elastic-Viscoplastic Model) (Cont.)

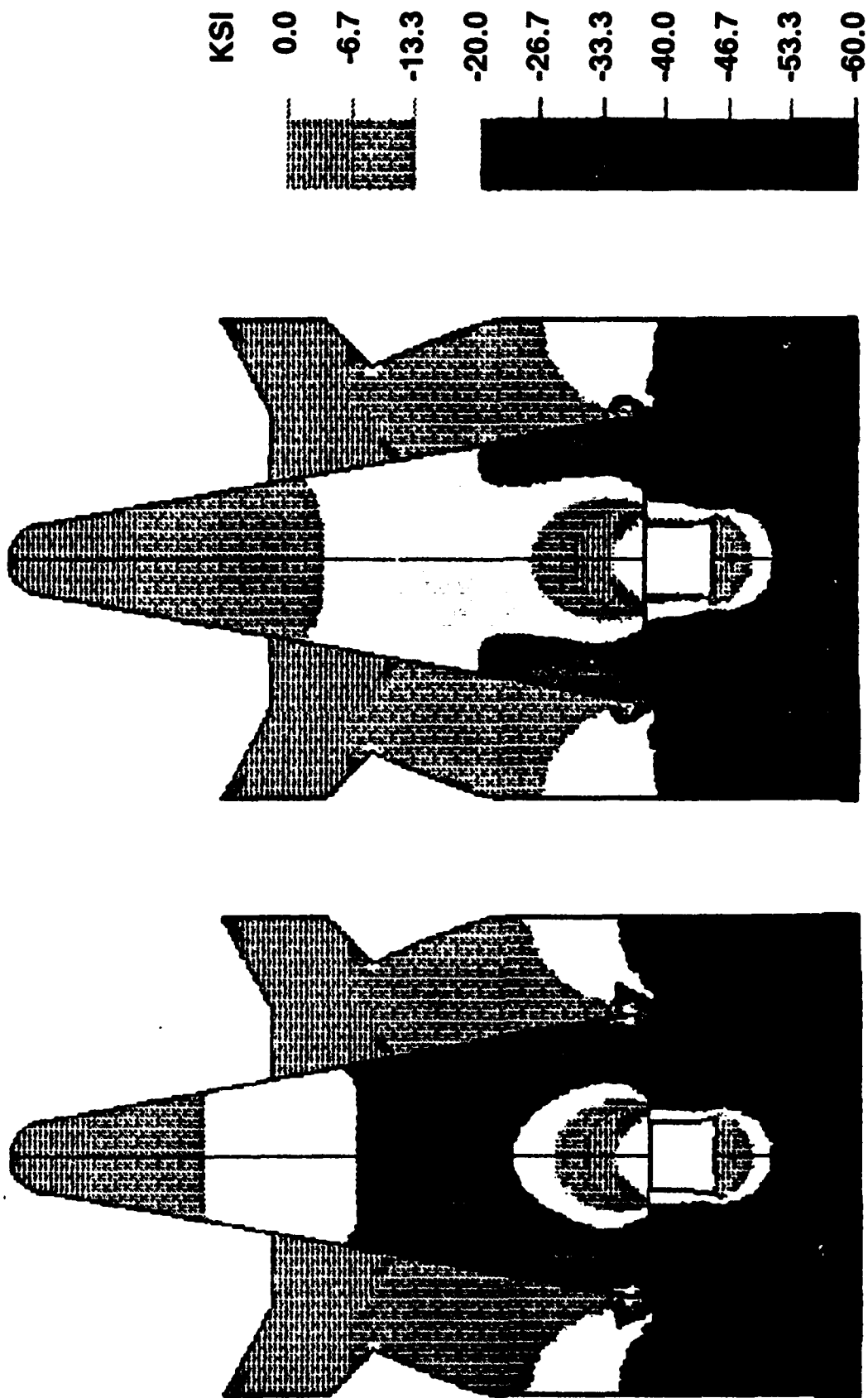


Figure 14. Axial Stress Contours (Elastic-Viscoplastic Model) (Cont.)

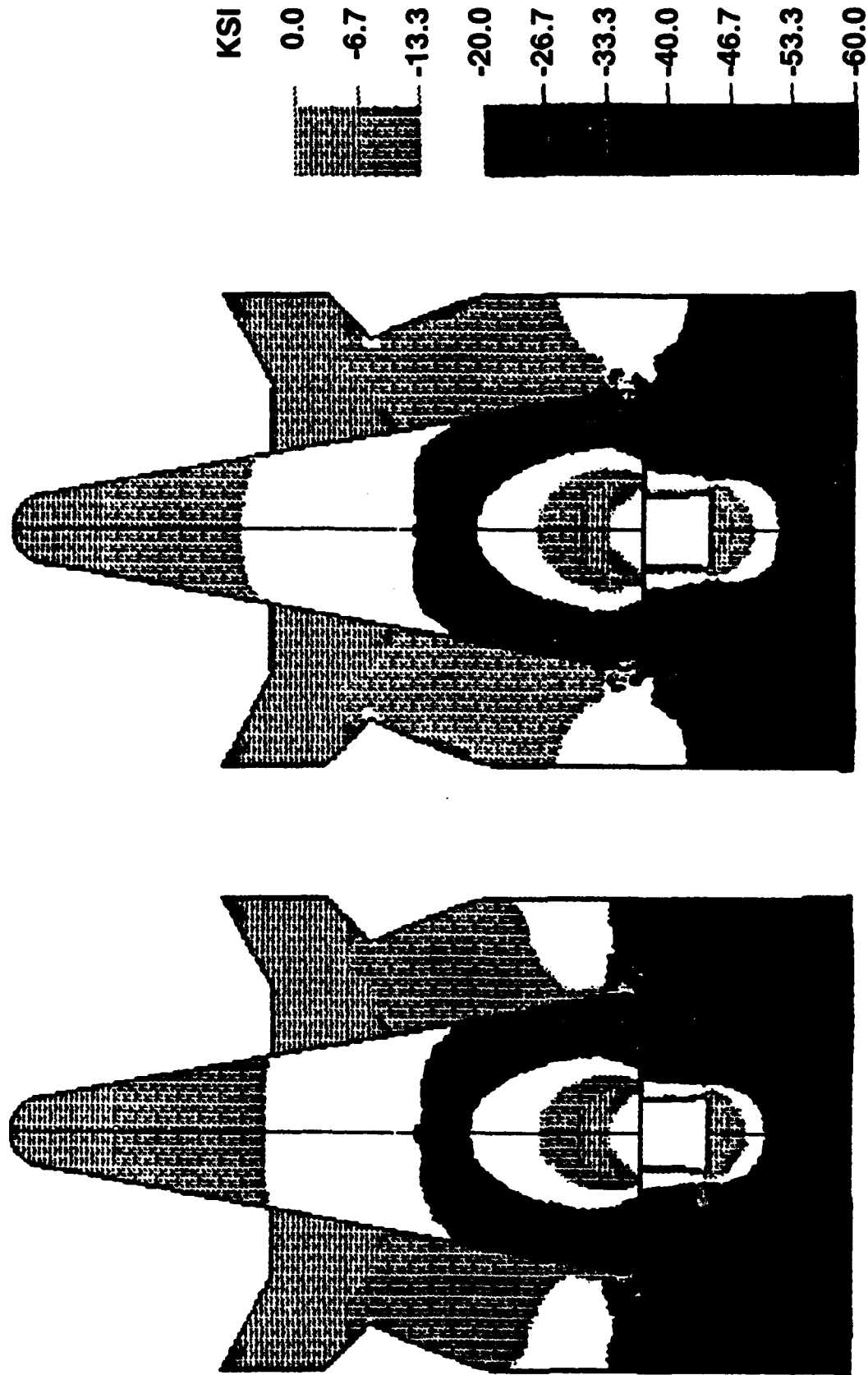
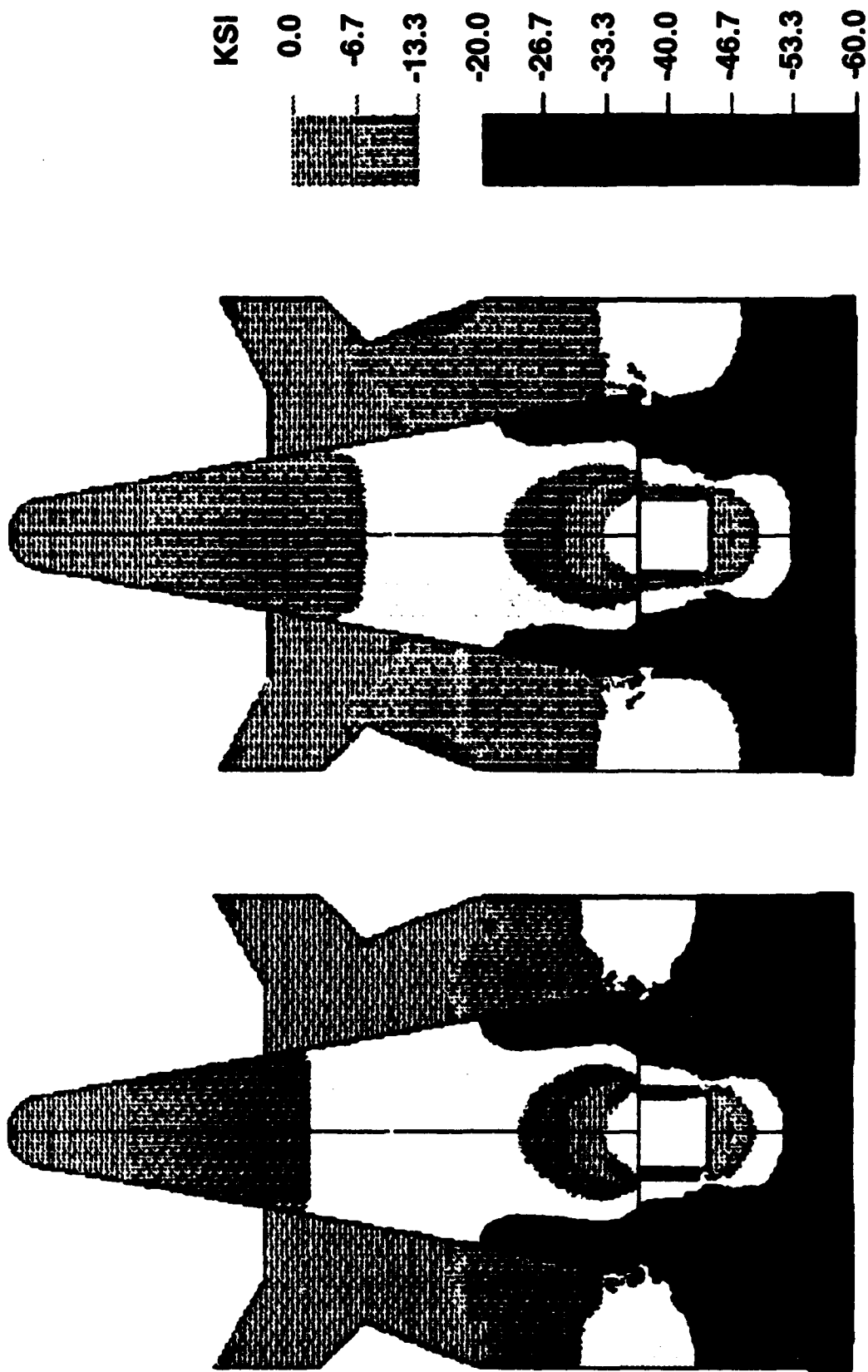
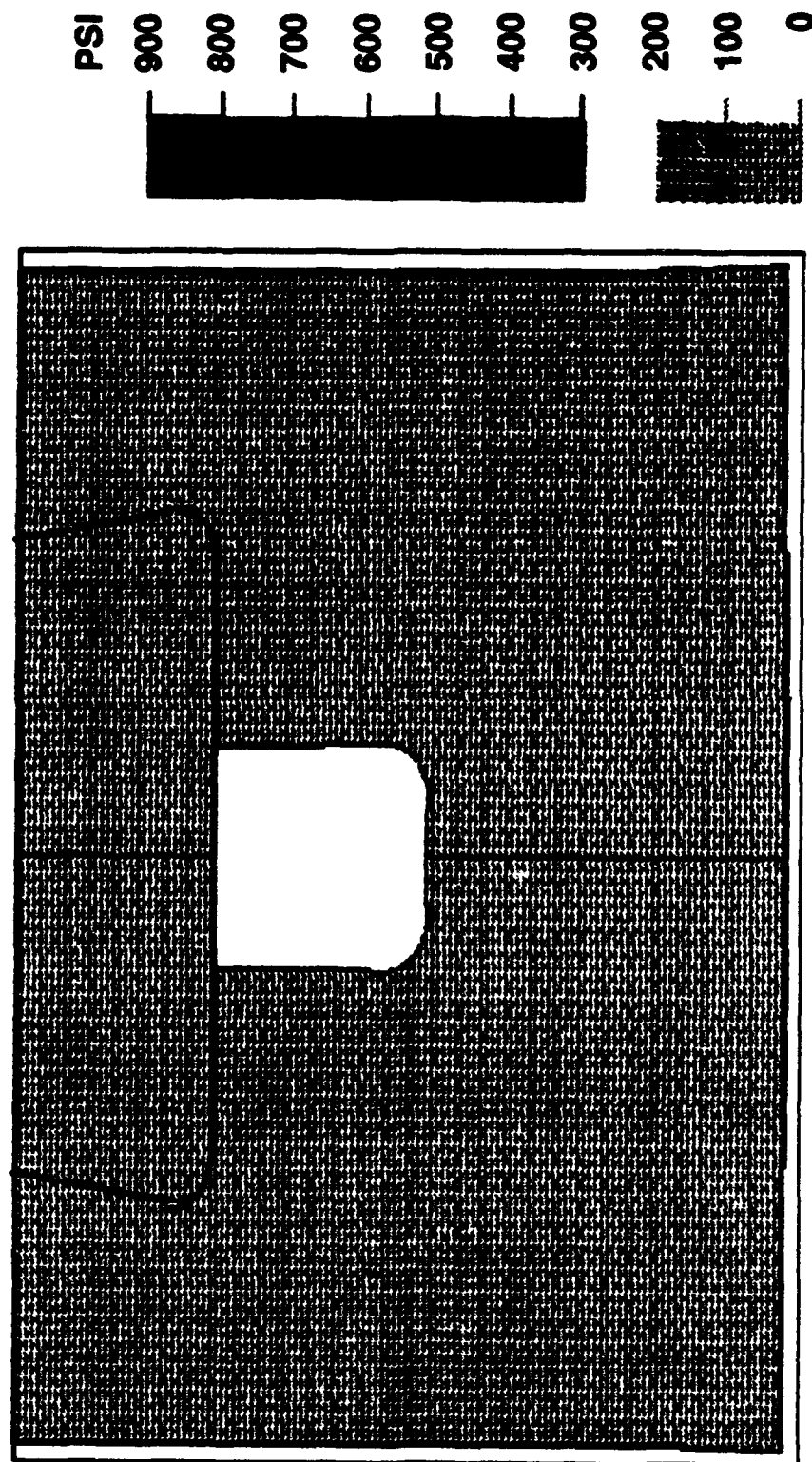


Figure 14. Axial Stress Contours (Elastic-Viscoplastic Model) (Cont.)



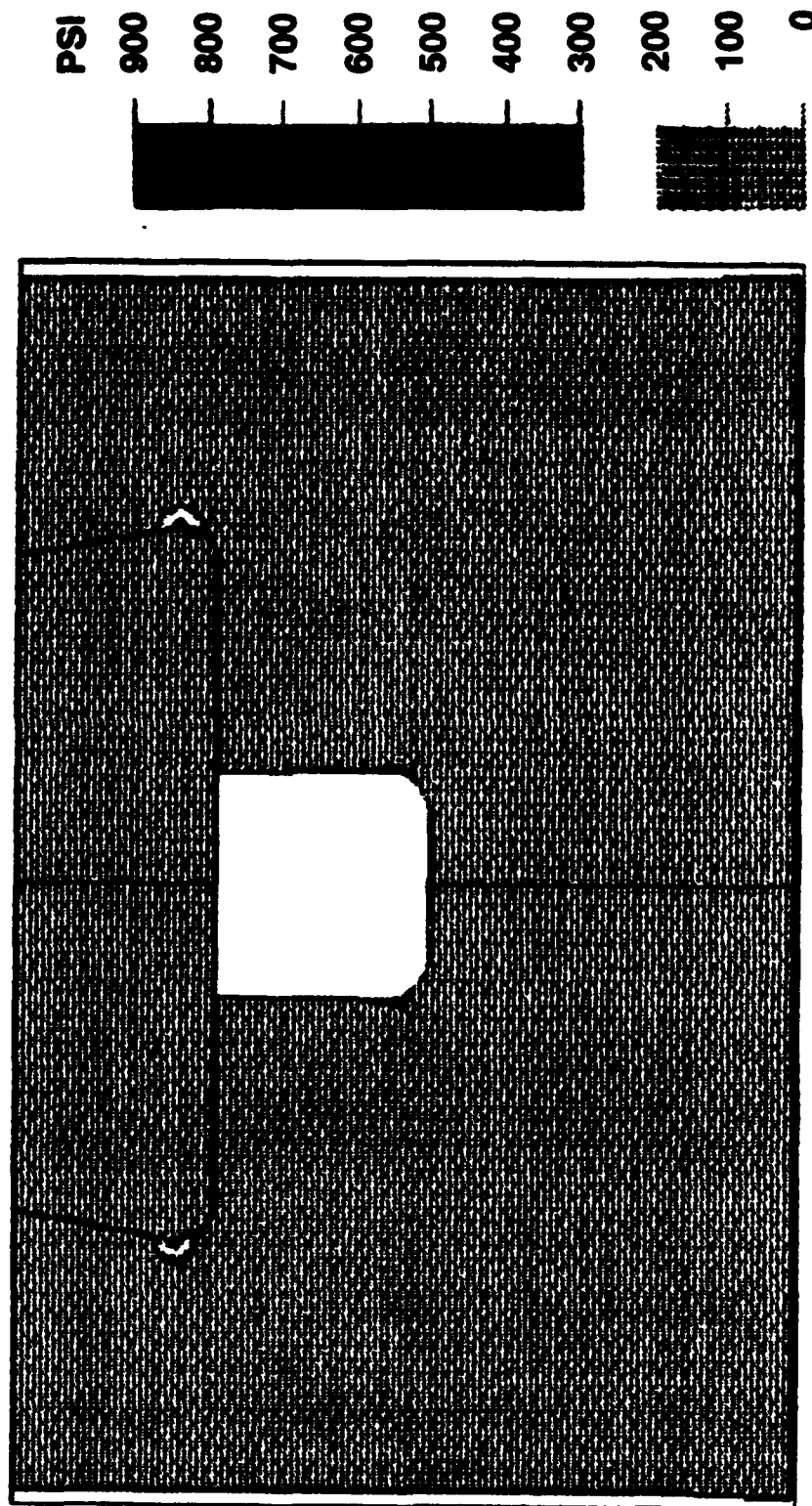
m. $t = 350 \mu s$ n. $t = 375 \mu s$

Figure 14. Axial Stress Contours (Elastic-Viscoplastic Model) (Cont.)



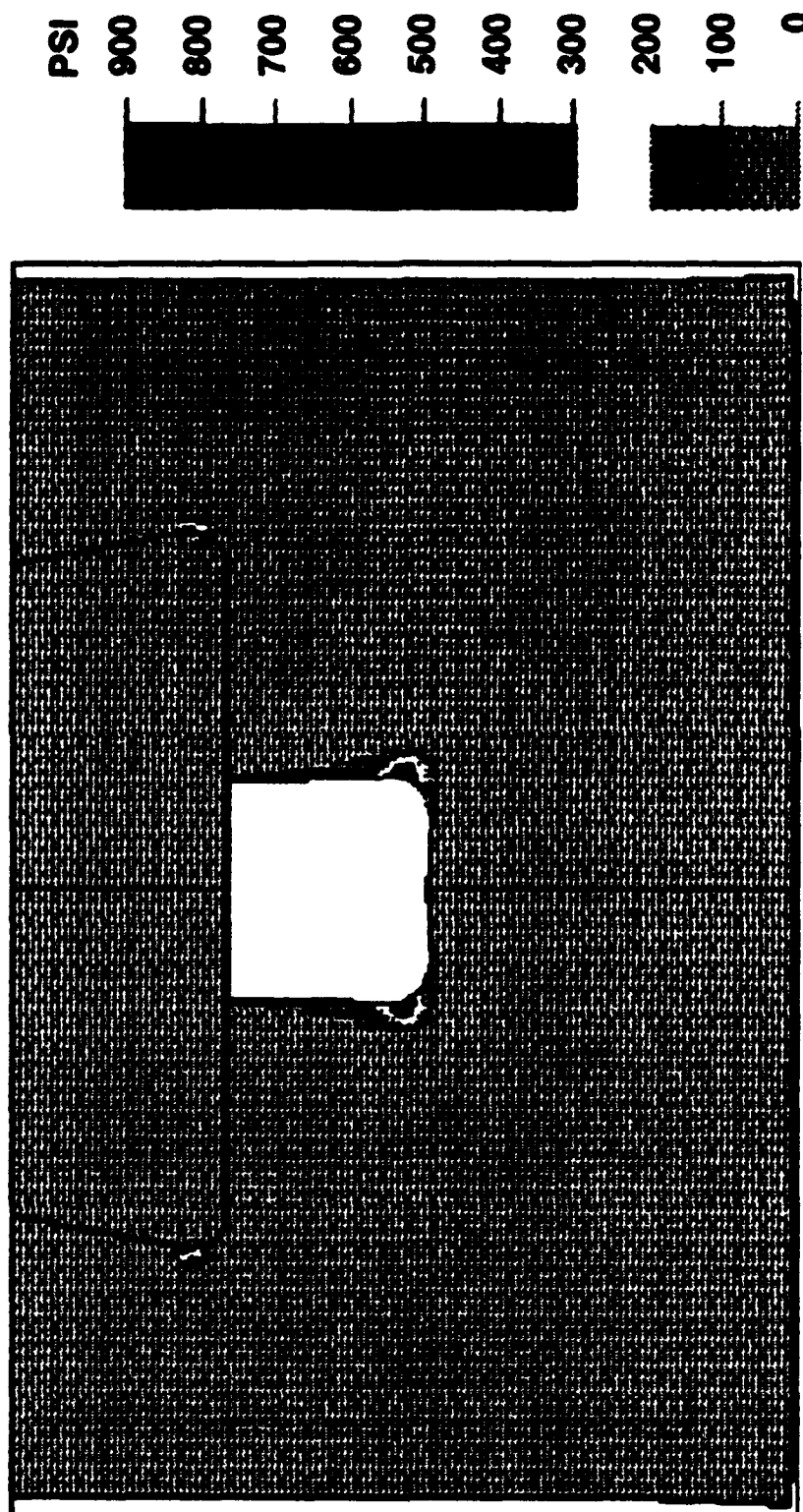
a. $t = 50 \mu s$

Figure 15. Plastic Work Density Contours (Elastic-Viscoplastic Model)



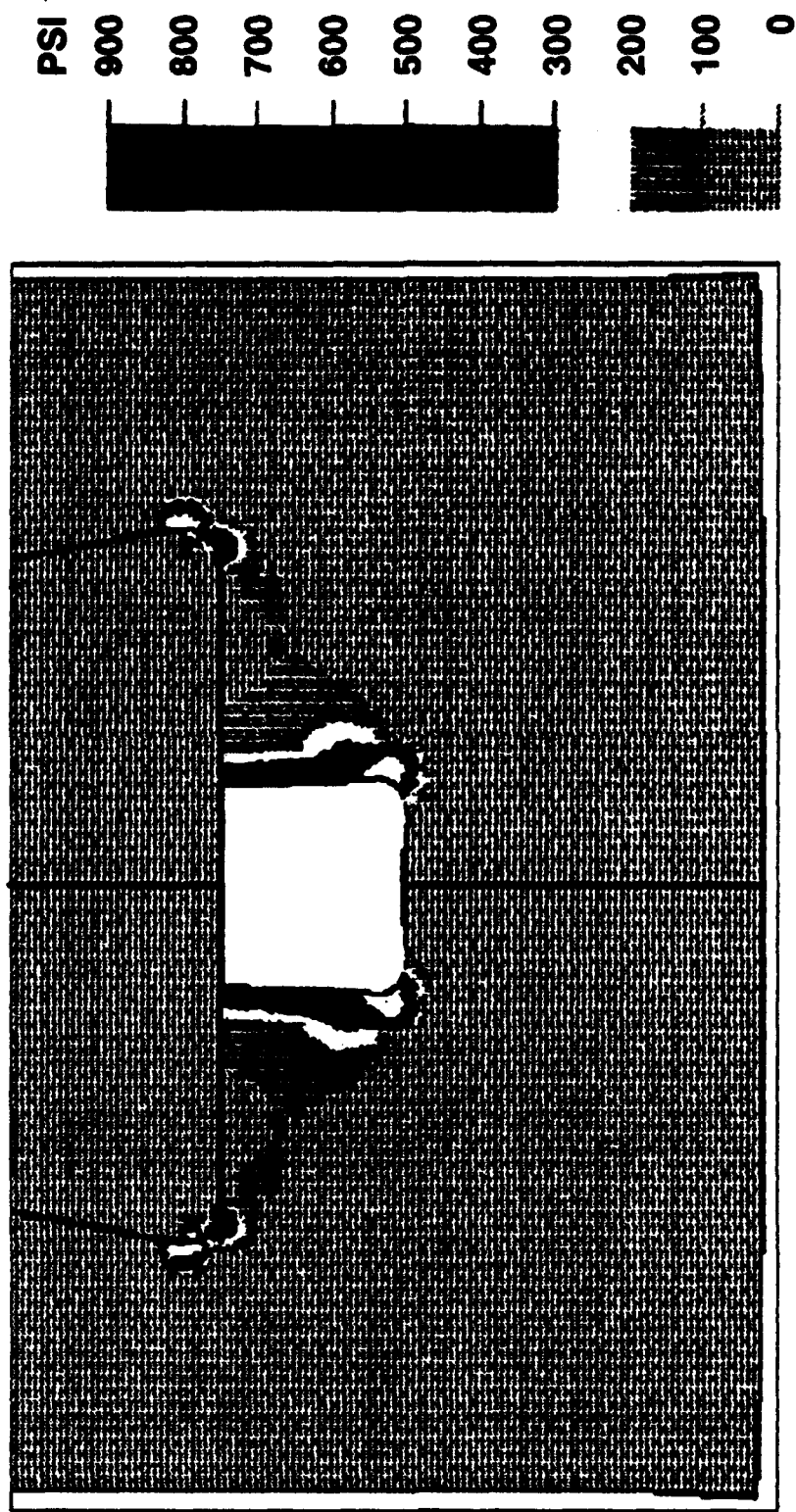
b. $t = 75 \mu s$

Figure 15. Plastic Work Density Contours (Elastic-Viscoplastic Model) (Cont.)



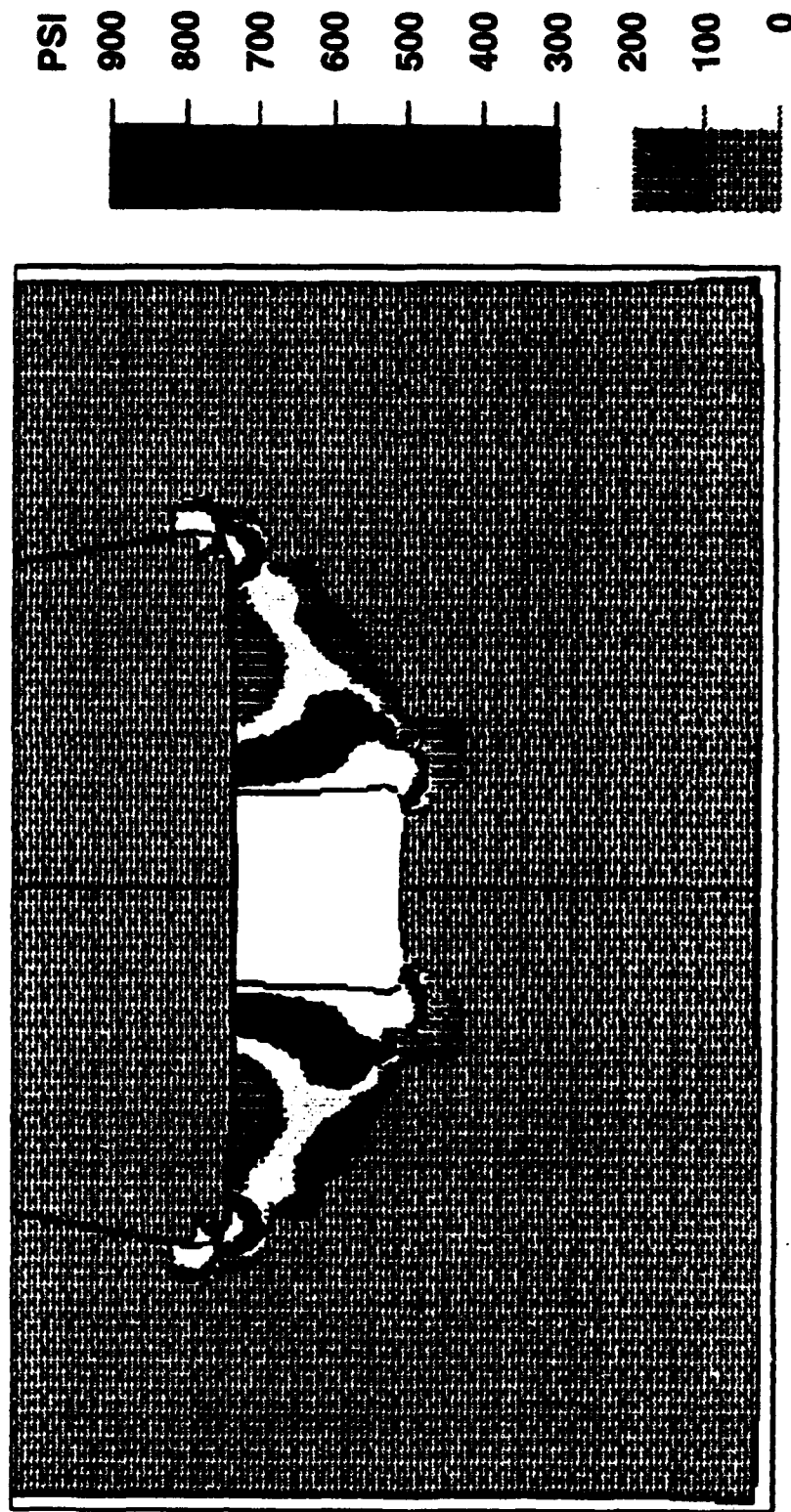
c. $t = 100 \mu s$

Figure 15. Plastic Work Density Contours (Elastic-Viscoplastic Model) (Cont.)



d. $t = 125 \mu s$

Figure 15. Plastic Work Density Contours (Elastic-Viscoplastic Model) (Cont.)



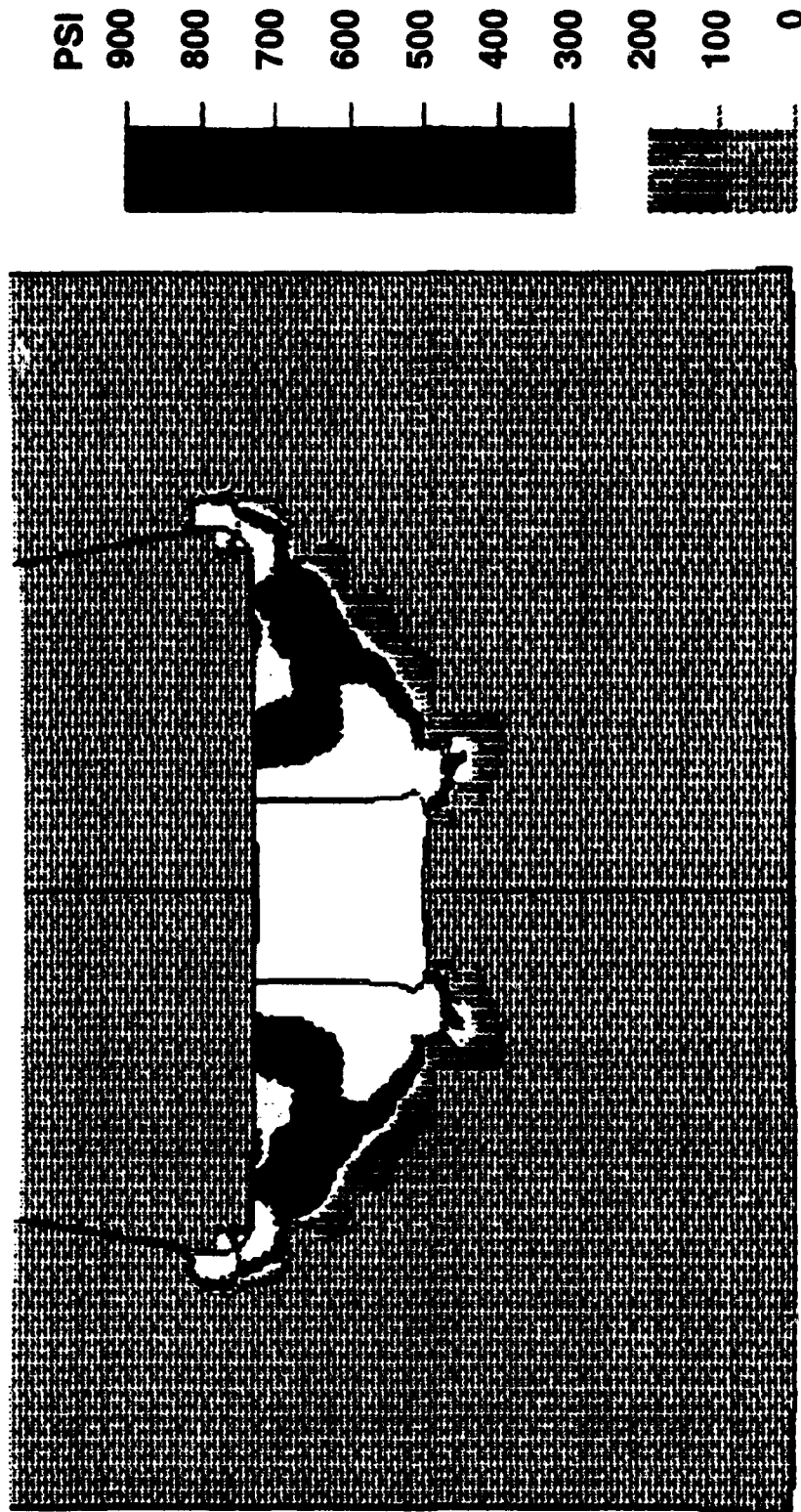
e. $t = 150 \mu s$

Figure 15. Plastic Work Density Contours (Elastic-Viscoplastic Model) (Cont.)



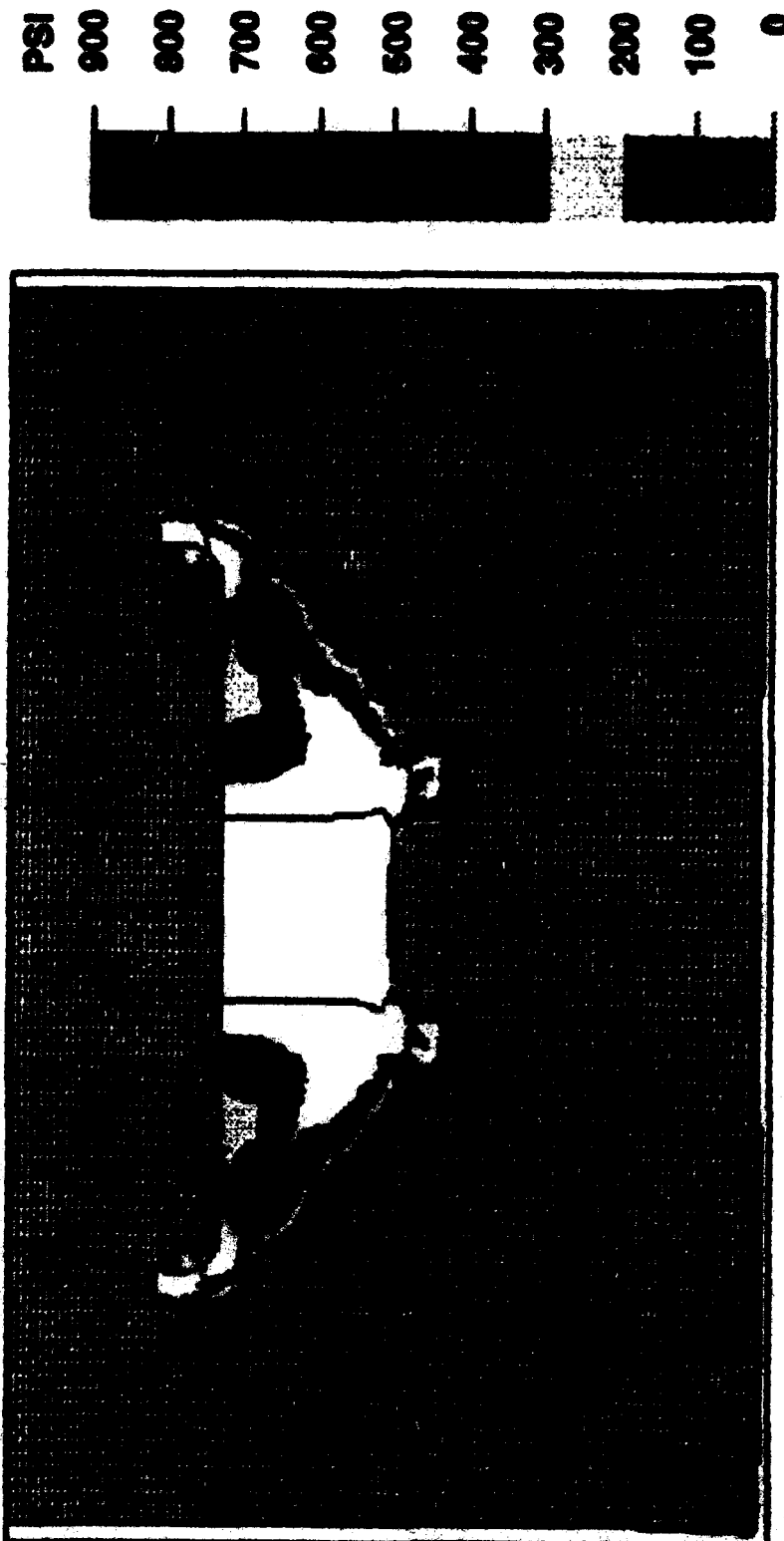
$t = 175 \mu s$

Figure 15. Plastic Work Density Contours (Elastic-Viscoplastic Model) (Cont.)



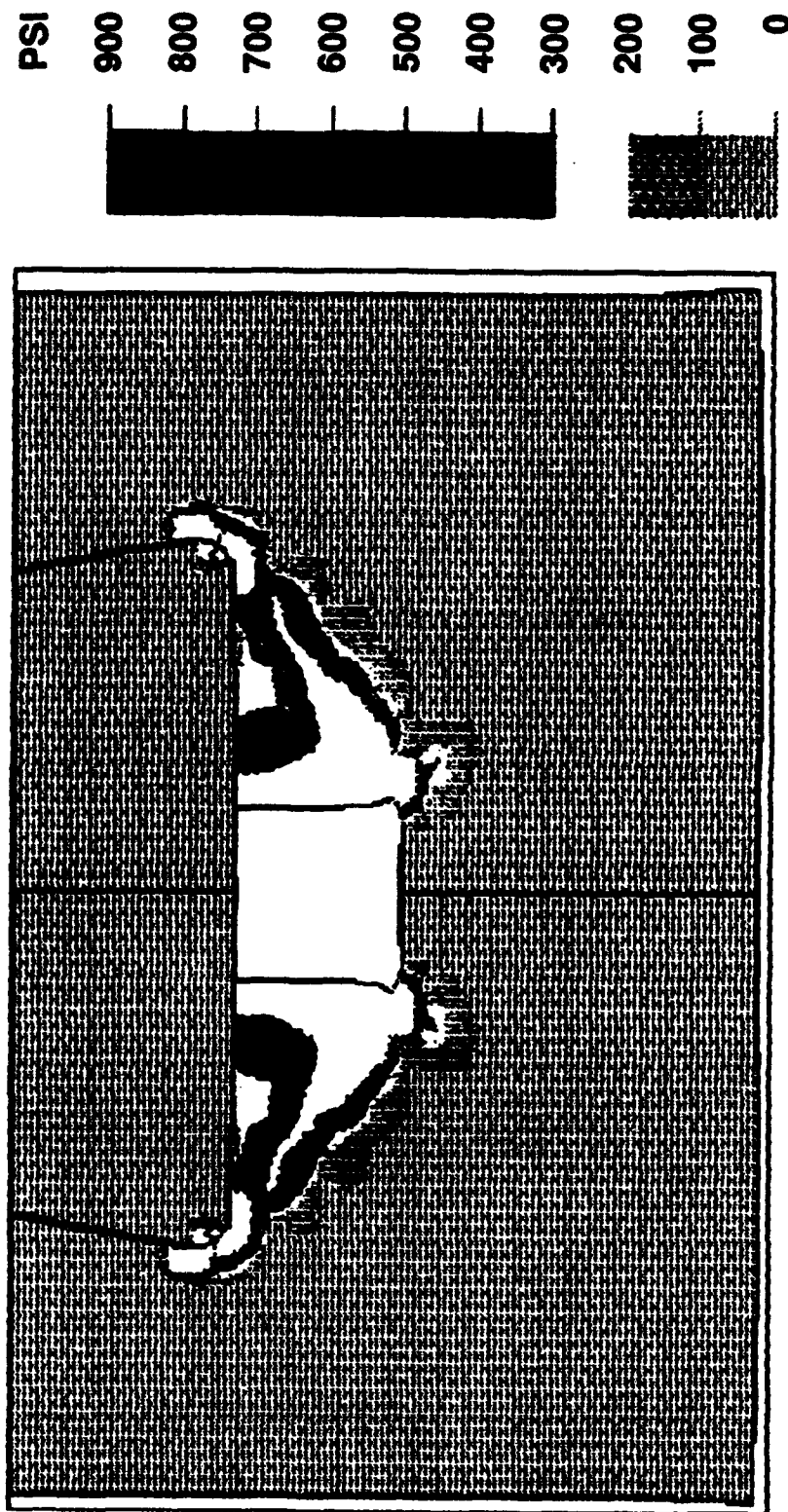
g. $t = 200 \mu s$

Figure 15. Plastic Work Density Contours (Elastic-Viscoplastic Model) (Cont.)



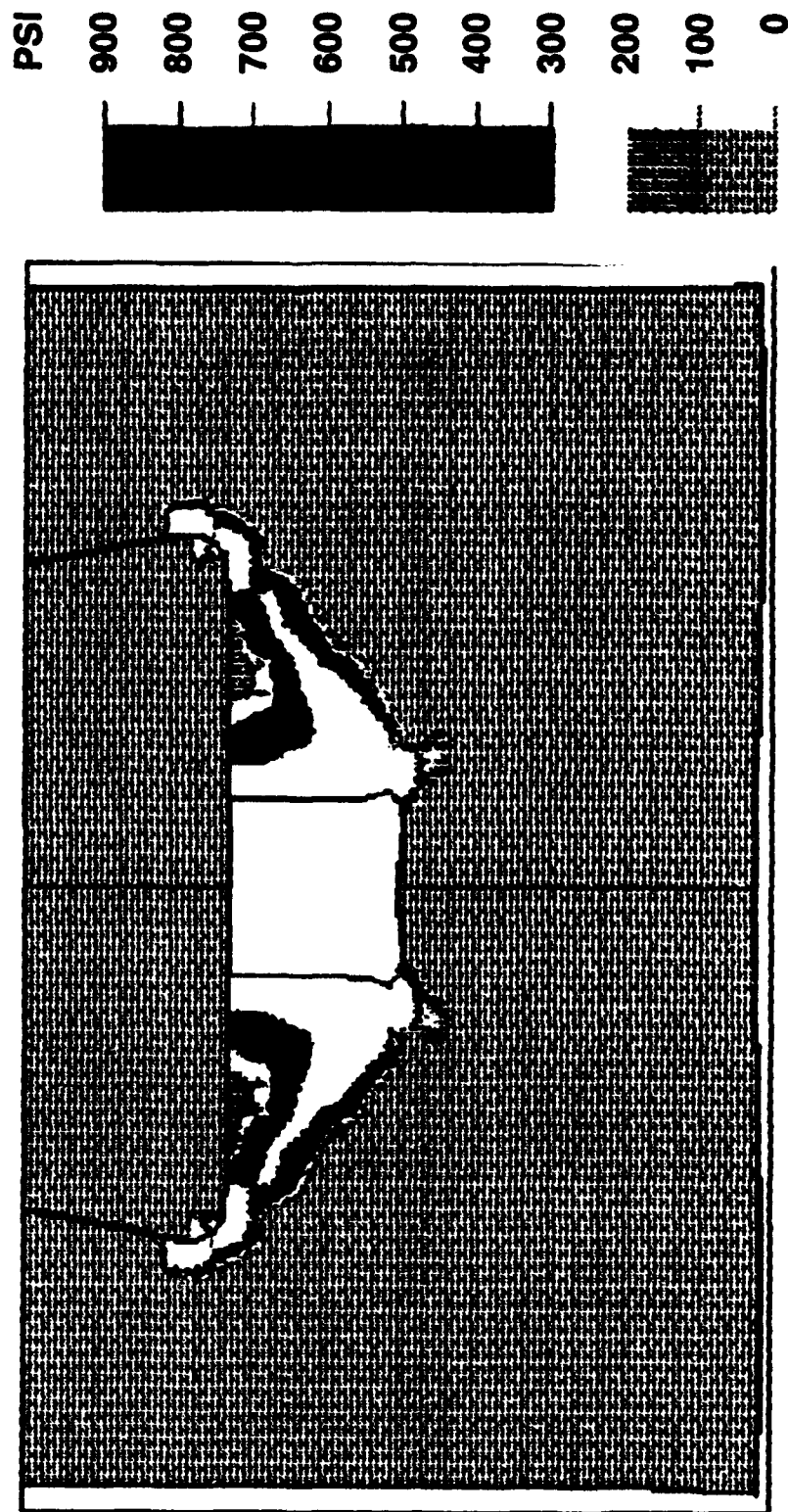
h. $t = 225 \mu s$

Figure 15. Plastic Work Density Contours (Elastic-Viscoplastic Model) (Cont.)



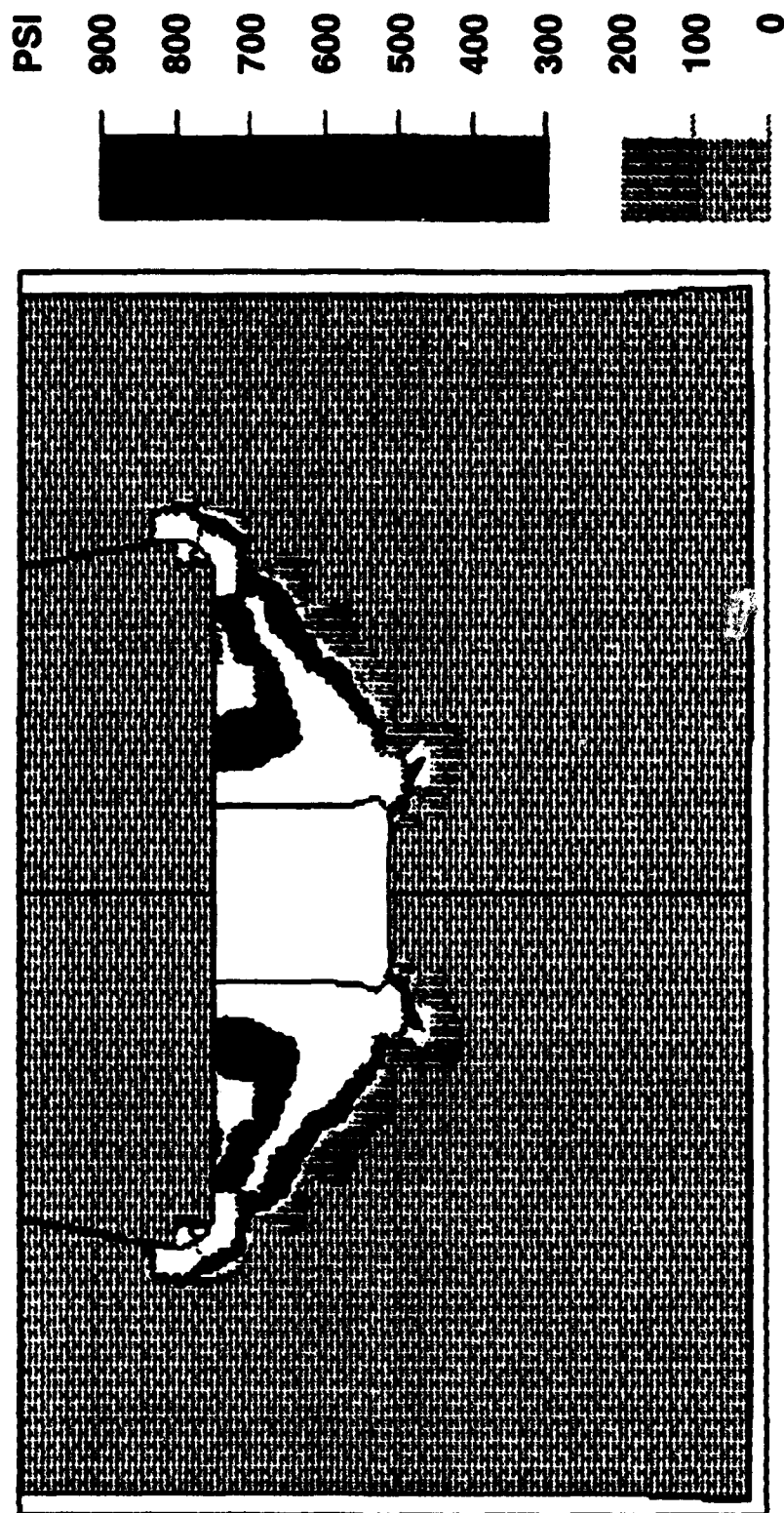
I. $t = 250 \mu s$

Figure 15. Plastic Work Density Contours (Elastic-Viscoplastic Model) (Cont.)



j. $t = 275 \mu s$

Figure 15. Plastic Work Density Contours (Elastic-Viscoplastic Model) (Cont.)



k. $t = 300 \mu s$

Figure 15. Plastic Work Density Contours (Elastic-Viscoplastic Model) (Cont.)

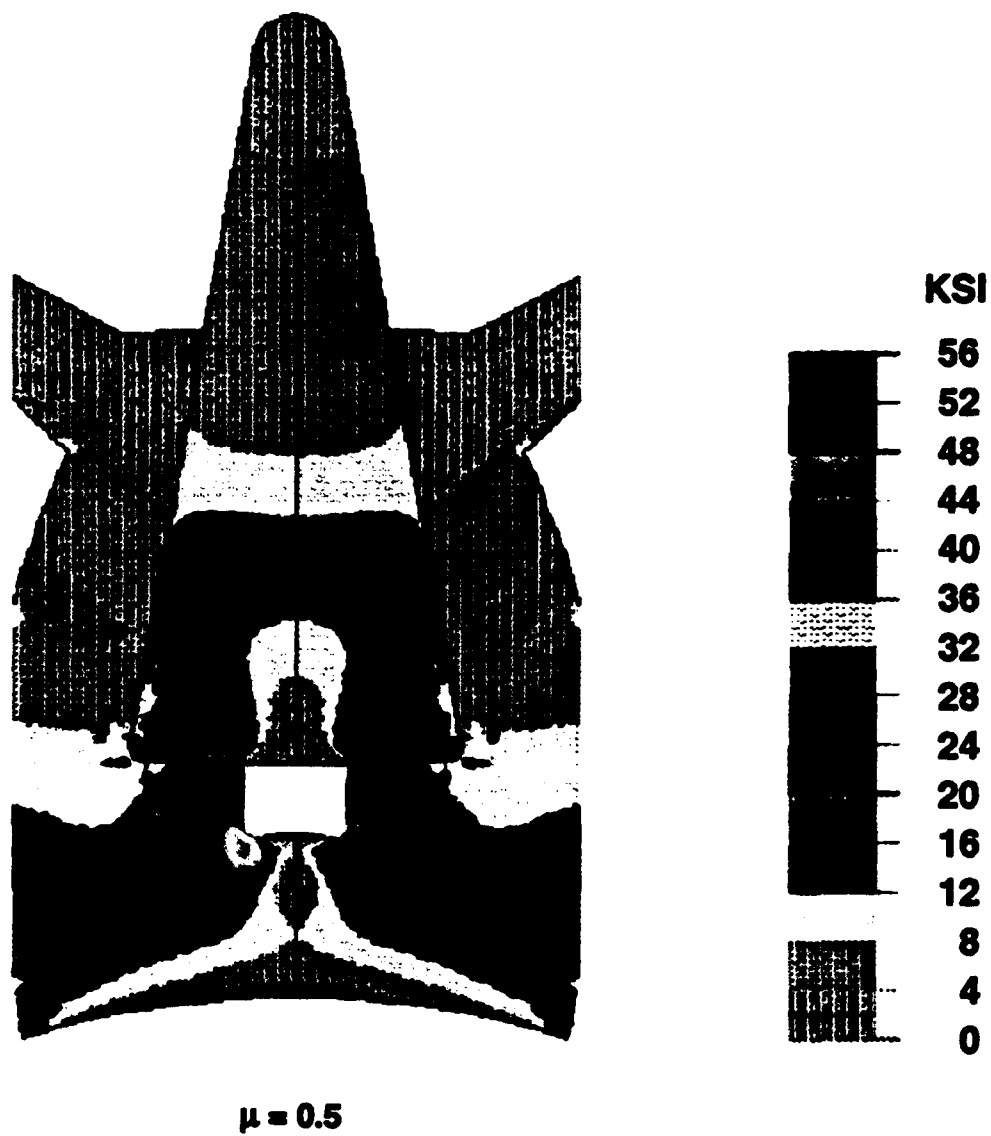


Figure 16. Maximum-Load Von Mises Contours with Friction at the Interfaces

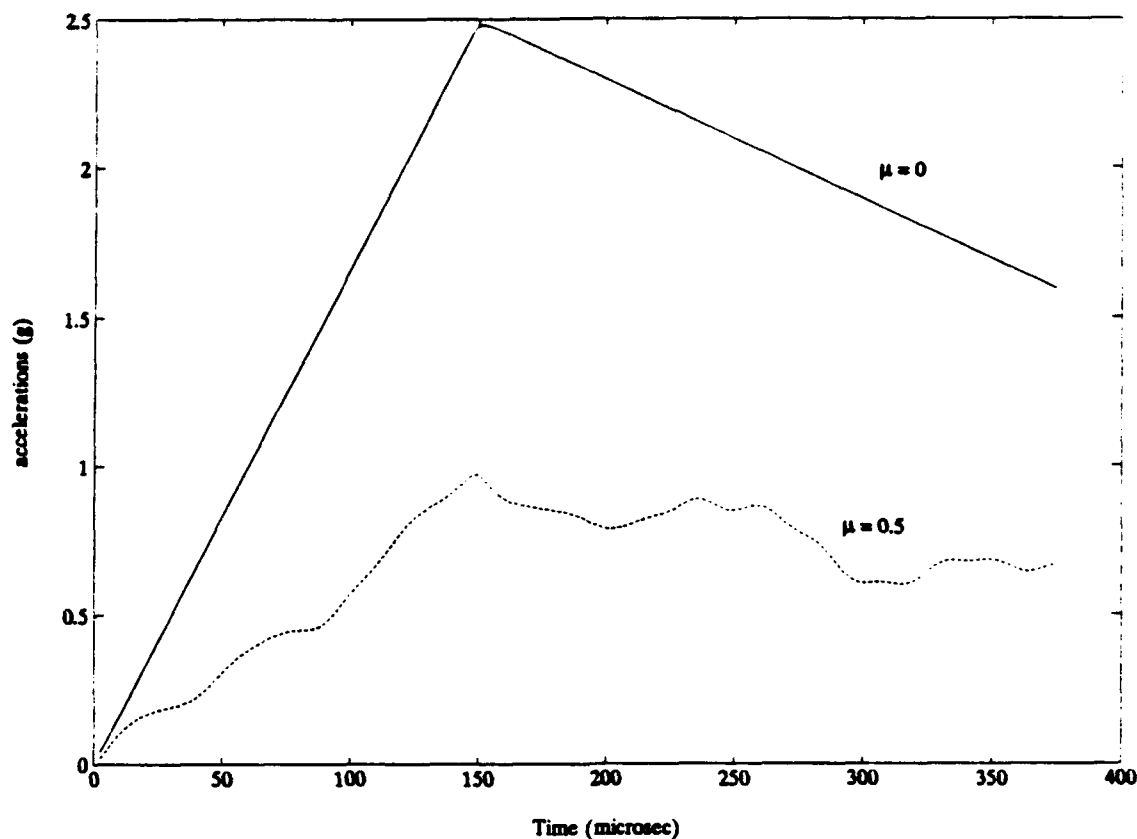


Figure 17. Acceleration of the Center of Mass with Friction

5.1.4 Elastic/Side Pressure

This simulation is identical to that described in Section 5.1.1 except that the side loads are a result of the mean gas pressure in a 5-mil gap between the sabot and the barrel wall instead of the constraint of the rigid wall. The von Mises stress at the maximum load is shown in Figure 18, which corresponds to Figure 12 in the rigid-wall constrained case. The side-pressure loads have the effect of decreasing the deviatoric loads near the sabot base but increasing the deviatoric loads near the top of the sabot and model. This can be explained qualitatively by examining the effect on a slug. As one can see from Figure 11a, the side-pressure load axial drop is far from linear, with little pressure drop occurring in the first half of the annulus. On the other hand, the axial loads vary somewhat linearly, and as a result the deviatoric stresses are low at the base and higher as one moves to the top of the sabot. In the constrained case, the side loads vary almost linearly, since they are related to the axial loads via Poisson's ratio. Therefore, the deviatoric stress will be highest where the axial loads are largest at the base.

5.1.5 Elastic/Erosion

To validate the erosion model, a 2.5-in.-diameter, 5-in.-long, cylindrical elastic Lexan slug is subjected to an idealized smooth pressure history as it travels down the 2.498-in. bore in an untapered barrel. The duration of the simulation is 5 ms with a linear load peaking at 40 ksi at 2 ms before dropping to zero. The history of the diameter of the slug, as a function of axial coordinate, is shown in Figure 19. To be precise, this is the rebound diameter of an elastic Lexan slug if at that point in

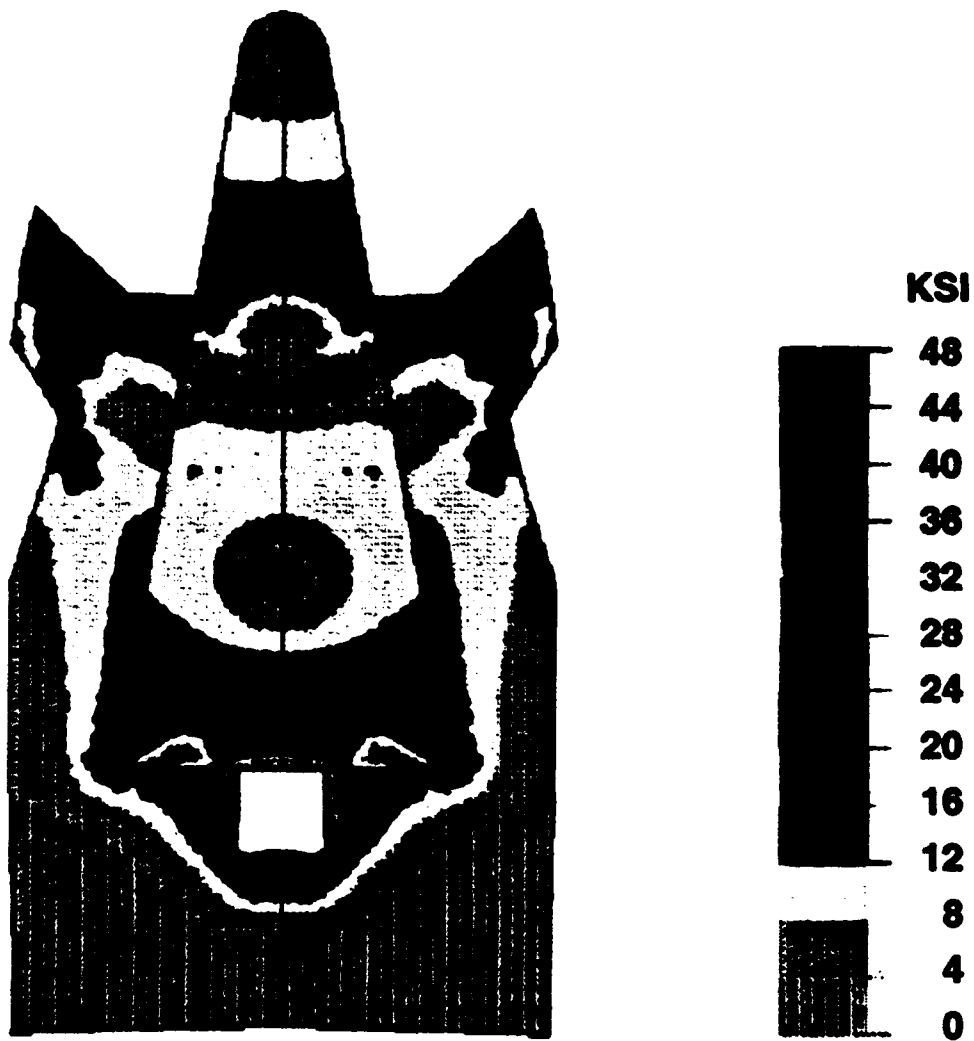


Figure 18. Maximum-Load Von Mises Contours with Side-Pressure Loads

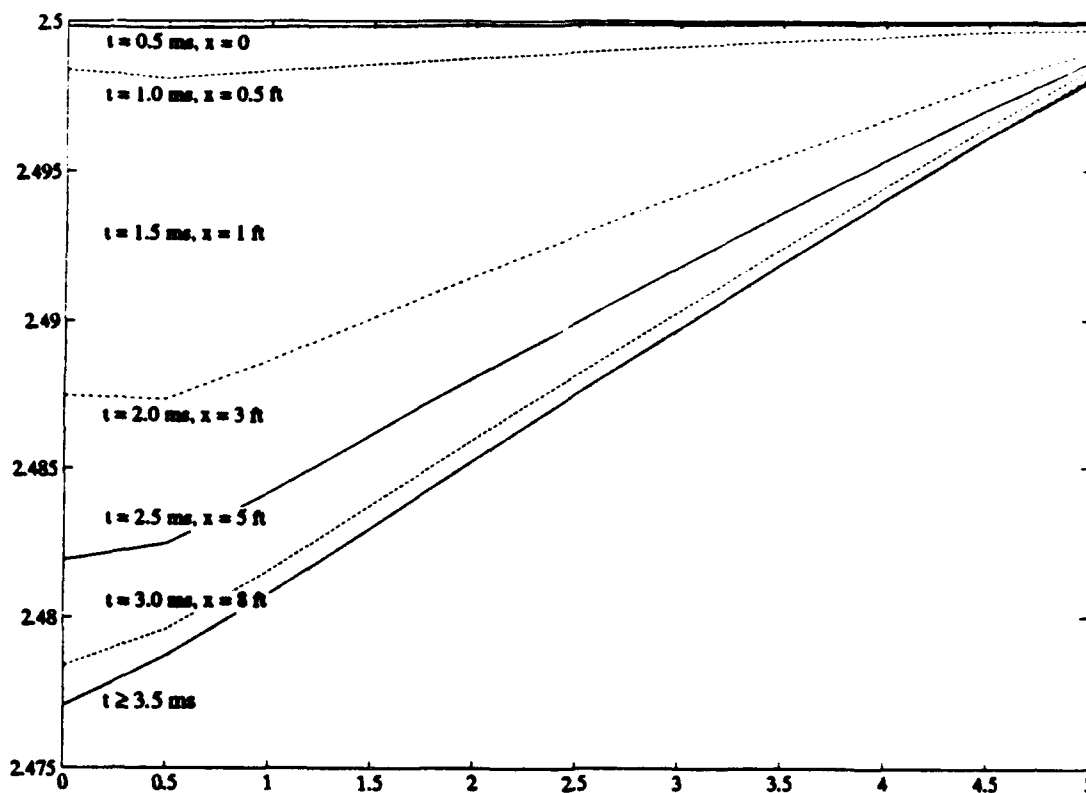


Figure 19. Lexan Slug Erosion History

time the pressure and the barrel wall are removed. The diameter curves are at equal intervals of time, and the location of the slug down the barrel is also labeled. Several things are evident from this plot:

- Not surprisingly, the model predicts that the most wear occurs at the base where the compressive forces are largest.
- The wear is not a linear function of time and reaches a limit diameter in which enough material has eroded that the axial compressive stresses are not sufficient to expand the slug into the barrel wall. In the last stages, the slug is primarily in free flight. This limit diameter (0.02 in. wear at base) is probably somewhat insensitive to the erosion rate since, if it eroded faster initially, it must eventually slow down because the compressive stress can expand out only so much material. The peak pressures and the material's Poisson's ratio, on the other hand, most likely have a strong influence on this limit diameter.
- The wear is far from linear along the barrel and most occurs in the first 8 ft. A linear tapering of the bore 0.04 in./68 ft would not be sufficient to hold the base in place but would certainly give rise to additional wear to the front. Eventually, the wear at the base of the slug would increase as it recontacted the barrel.
- The wear predicted by the model does not lead to the football shapes observed in experiments (Powell et al., 1985). The observed front end wear is a good clue that ballating does occur, giving rise to the wear at the extremities.

Before one can make any firm conclusions from this wear model, more realistic geometries and loading should be used and the effects of the taper and the material parameters should be examined closely.

5.2 Water Cannon Tests on a Lexan Slug

5.2.1 Test Conditions

A 6-in.-long, 2.5-in.-diameter Lexan slug, which is about 1 mil larger than the bore of the test chamber, is accelerated by impact with an aluminum piston. The mass and stiffness of the piston is such that the Lexan experiences a pressure history that has a very sharp rise and then relaxes slowly until the induced stress wave passes through the length of the slug, reflects, and returns to the base. At this point, the piston and the slug separate and the pressure drops to zero. In the test apparatus, the piston strikes a disk of water held in place by the slug and a thin diaphragm. The water serves to smooth out the impact on the Lexan and provides a medium to measure the pressure with a pressure transducer. A typical measured pressure history is shown in Figure 20. This pressure history is idealized as a pulse that has a linear rise time of 20 μs and then drops linearly over a period of 130 μs for a total duration of 150 μs . The measured rise time is closer to 10 μs , but the contact elements behaved erratically because the grid is not sufficiently fine to resolve the short impulse. Regardless, the measured rise time may be in error because of the limited frequency response of the transducer.

The finite element grid consists of 250 solid elements with another 25 contact elements. There are 821 nodes and 1774 degrees of freedom including the constraint forces. The friction elements model the full range of possible states: free, sliding contact, and sticking contact. Much of the essential dynamics are represented here. In loading the Lexan slug into the chamber, a lubricant is used to reduce the friction. Based on the required load to push the Lexan slug into the chamber, a coefficient of friction of 0.1 is estimated and used in the model. As before, the initial stresses in the Lexan are determined by a static simulation.

5.2.2 Elastic

Using the static value of the elastic modulus, an elastic simulation has been conducted for over a 160- μs time frame with a peak pressure of 25 ksi. In Figures 21a through 21h, a series of snapshots of the axial stress at different times is shown on an exaggerated deformation plot in which the scale of the exaggeration is held constant. The stress wave has moved little by the time of the maximum pressure shown in Figure 18a. The contraction of the slug is very evident and some slight deviation from one dimension is observed because of the friction. At $t = 80 \mu\text{s}$, shown in Figure 21d, the wave reaches the top of the slug and, in the next figure, a tensile wave begins to develop on reflection. As this tensile wave grows, the Lexan pulls away from the barrel wall with the evident contraction in the middle. At $t = 160 \mu\text{s}$ the Lexan is stretched to a maximum and the maximum tensile stresses are near 23 ksi with tensile stresses spanning the diameter as high as 13 ksi.

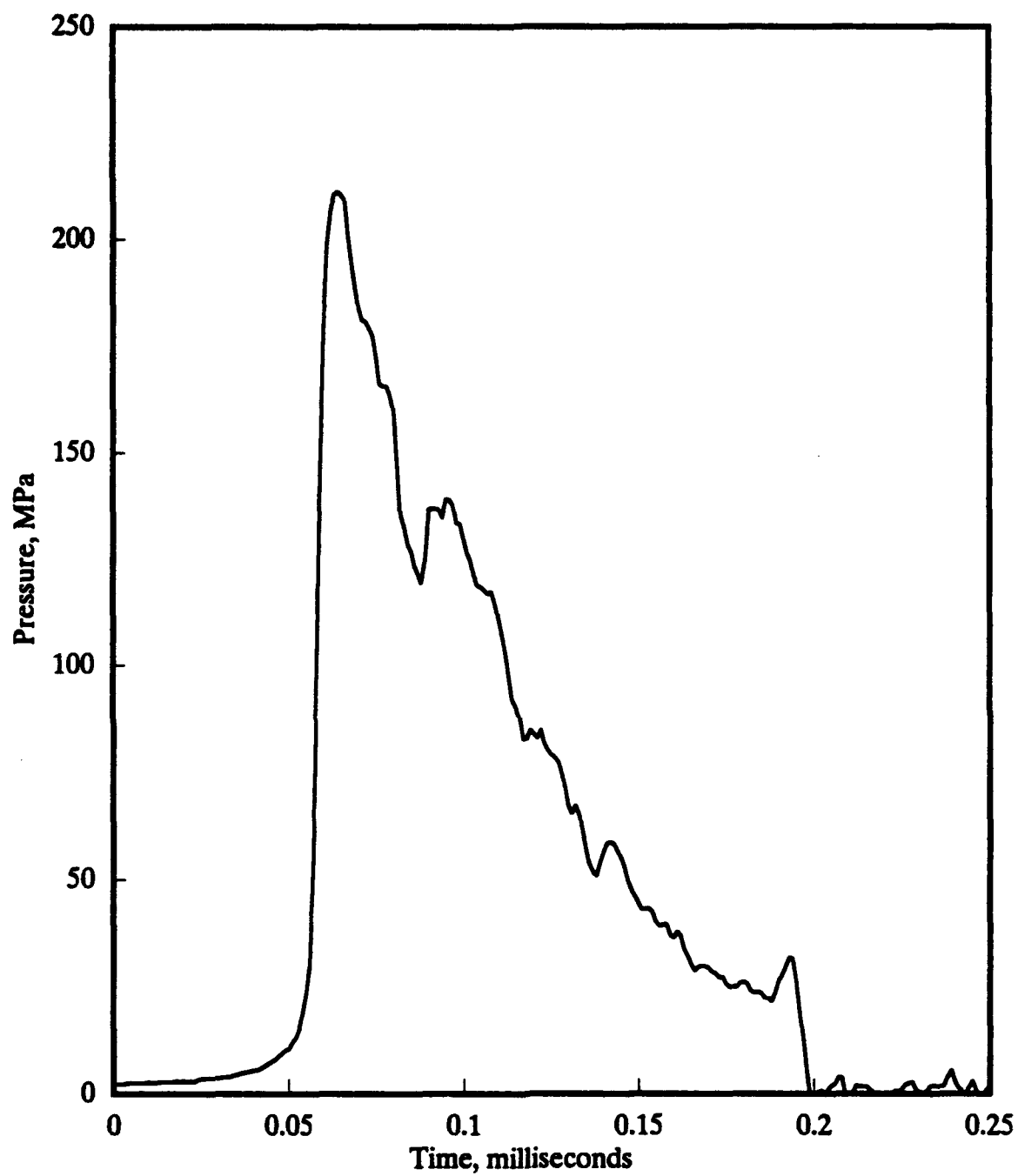


Figure 20. Typical Water Cannon Pressure Pulse History

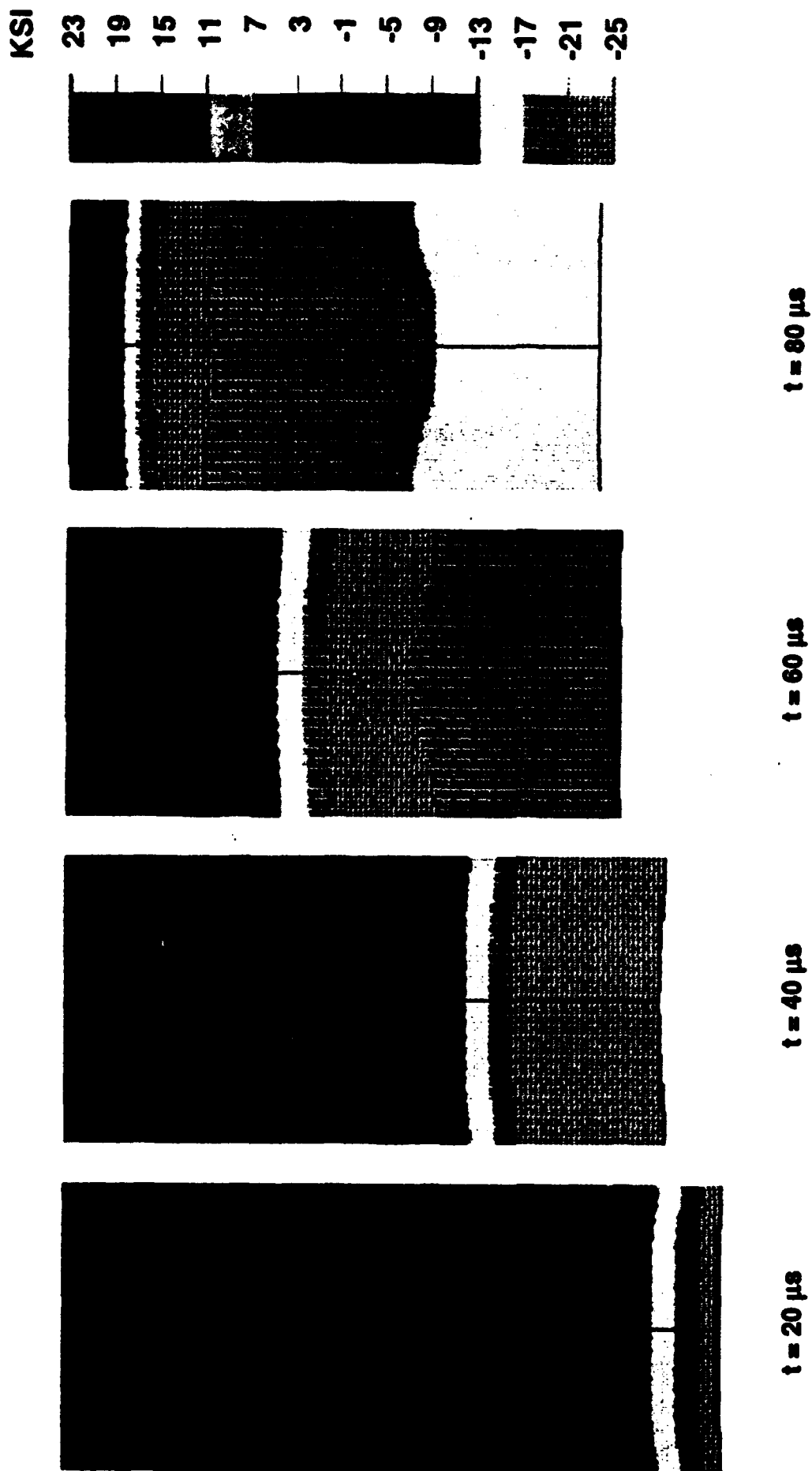


Figure 21. Elastic Lexan Slug Axial Stress History ($p_{max} = 25 \text{ ksi}$)

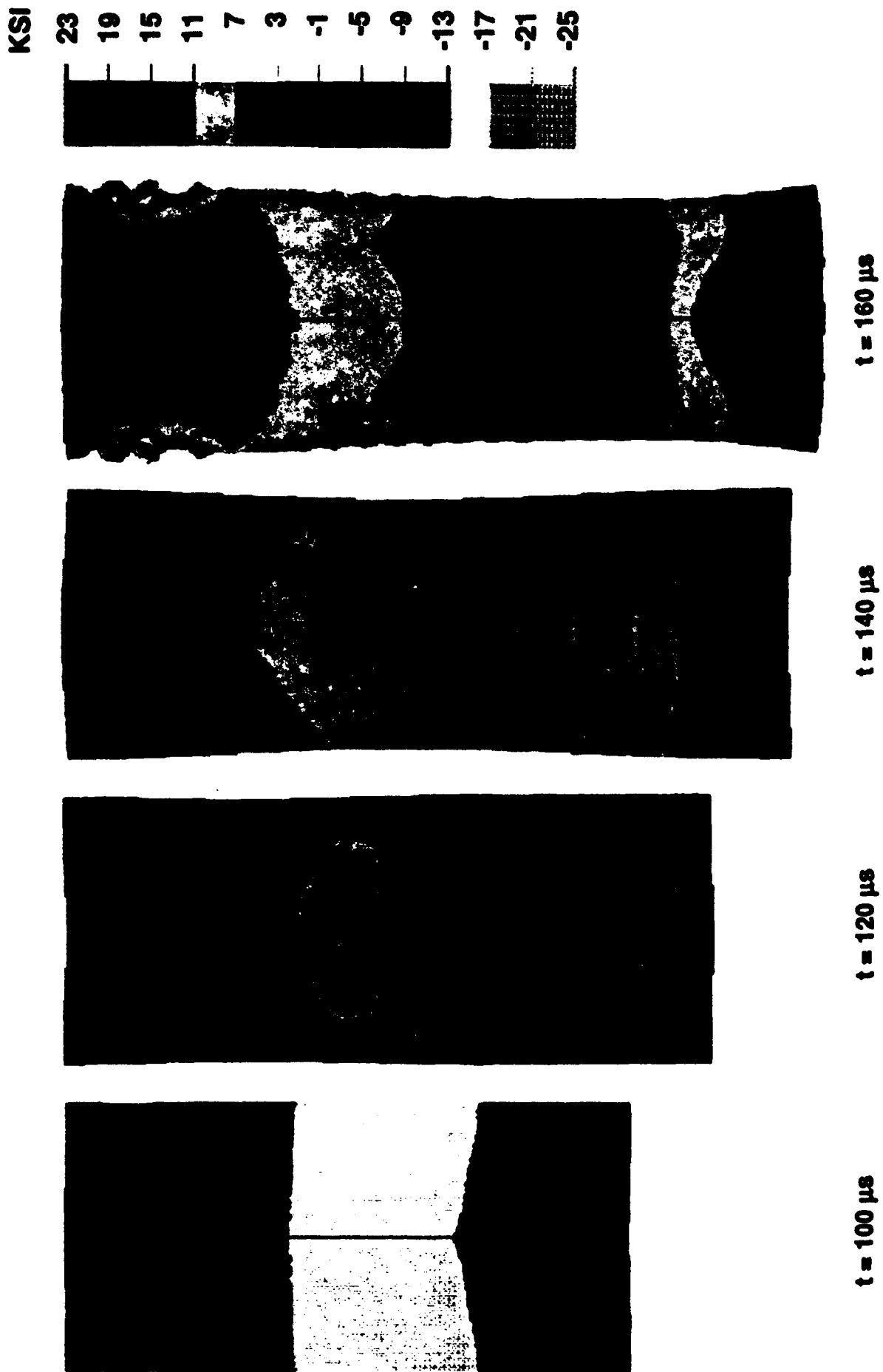


Figure 21. Elastic Lexan Slug Axial Stress History ($p_{max} = 25 \text{ ksi}$) (Cont.)

The garbage at the top of the Lexan near the interface is a result of the slug returning to contact with the rigid barrel wall. The local radial velocities at the point of recontact are on the order of 150 fps, so the impact is quite energetic, but since the wall does not give, the contacting sabot bounces back off in the next time step. The momentum pushes the Lexan section back into the wall, setting up the oscillations. The integration method assumes continuous accelerations, but the rigid wall produces a radical change in the radial acceleration. To eliminate this problem, the wall is allowed to deform based on a stiffness that is about 10 times larger than the sabot. This effectively smooths the accelerations and gives a more realistic model of the barrel wall.

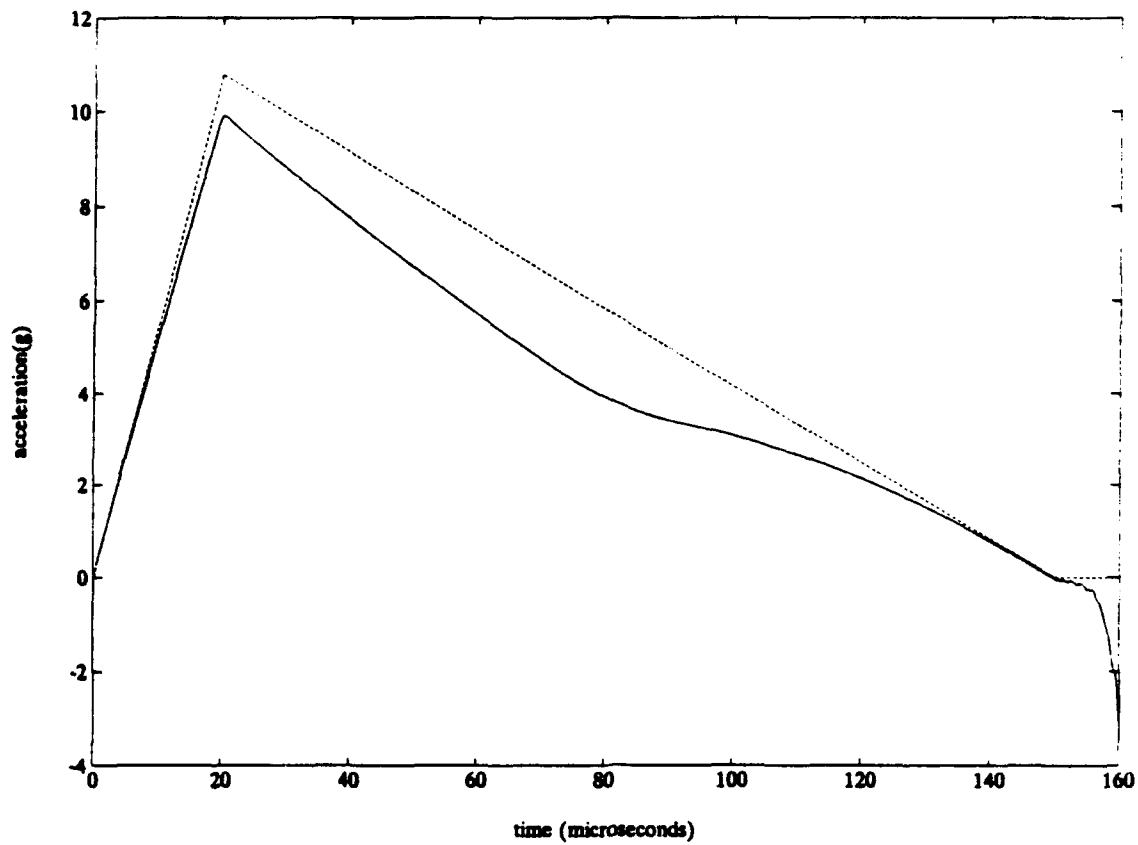
Figure 22a shows plots of the acceleration of the center of mass along with the acceleration if the slug were frictionless. The deviation from the frictionless case is most pronounced as more of the slug goes into compression and expands against the barrel wall, producing more friction. In the later stages, as the Lexan under tension pulls away from the barrel wall, the acceleration approaches the frictionless value. In Figure 22b, the velocity of the center of mass and the point at the base adjacent to the barrel wall are plotted. The material point quickly rises to a peak velocity and then falls back to a value less than zero before rising again. If the model is propagating the signal at the correct speed, then the wave reflecting off the base should be occurring at the same time that the pressure history goes to zero at 150 μ s. The fact that this elastic model is representing the transfer time to within about 10 μ s implies that the addition of viscoelastic and viscoplastic effects should not greatly alter this time.

The axial stress at 160 μ s for a peak load of 40 ksi is shown in Figure 23 with the contour scales based on the range of stress at this time. Here, the peaks are near 33 ksi with the tensile stresses near 21 ksi over the diameter. These tensile loads are quite high and, since the Lexan slug did not fail at these loads, either the tensile strengths are quite high or this elastic simulation, which has no damping, predicts too large of a tensile stress.

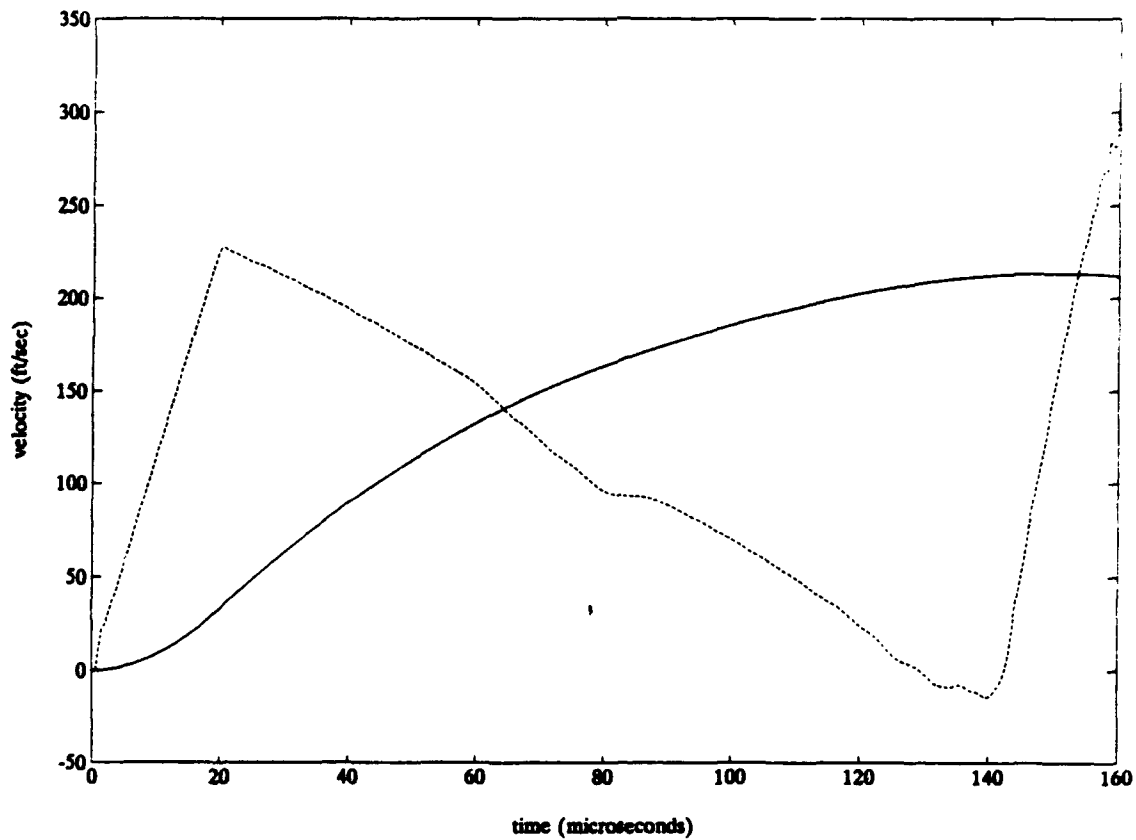
5.2.3 Elastic-Viscoplastic

Simulations similar to those in the previous section have been carried out using the elastic-viscoplastic model. Qualitatively, the results are similar to the elastic simulations, but the peak stresses are not as large because of the redistribution to yielding. Figure 24 corresponds to Figure 23 except for the change in material model. The peak axial tensile stresses are about 26 ksi with 23 ksi stresses across the diameter. The plastic work, shown in Figure 25, indicates that most of the failure yielding that has occurred is associated with the tensile load. Although the axial compression loads are higher, the barrel wall constrains the expansion to reduce the von Mises stresses. The tensile stress is unconstrained, so the deviatoric stress is larger.

Figures 26 and 27 are similar plots to Figures 24 and 25 except that peak pressures are at 50 ksi.



a. Acceleration ($p_{\max} = 25$ ksi)



b. Velocity ($p_{\max} = 25$ ksi)

Figure 22. Acceleration and Velocity of the Center of Mass (Elastic Model)

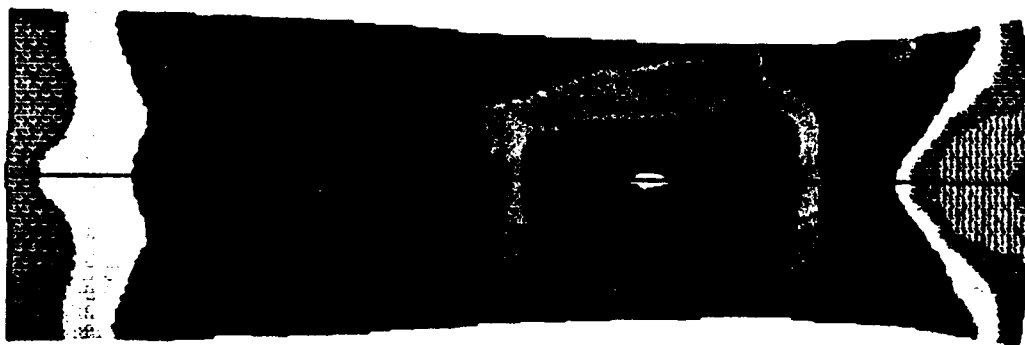


Figure 23. Elastic Lexan Slug Axial Stress at $t = 160 \mu s$ ($p_{max} = 40 \text{ ksi}$)



Figure 24. Elastic-Viscoplastic Lexan Slug Axial Stress at $t = 160 \mu s$ ($p_{max} = 40 \text{ ksi}$)

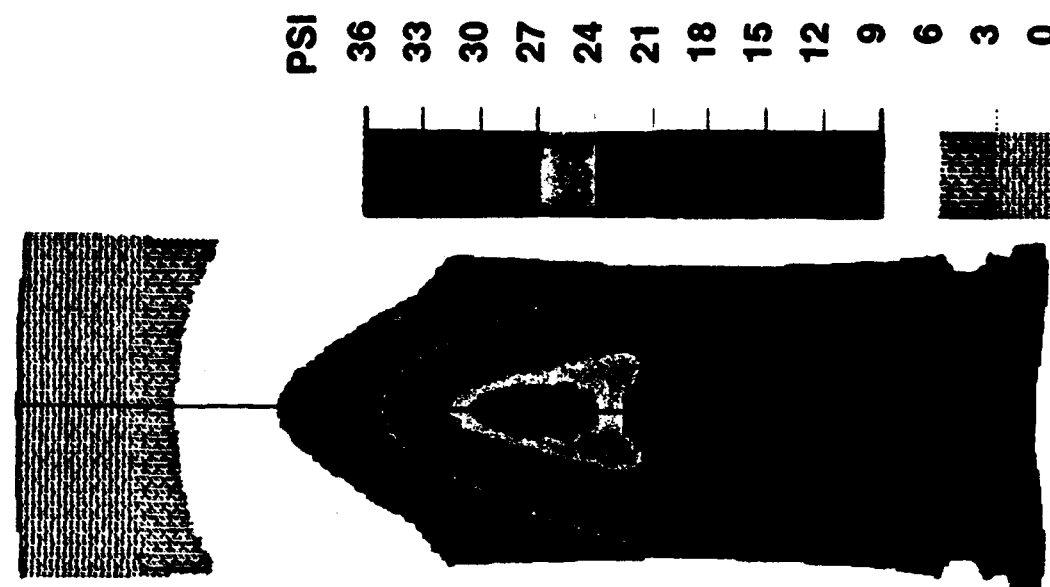


Figure 25. Elastic-Viscoplastic Lexan Slug Plastic Work at $t = 160 \mu s$ ($p_{max} = 40 \text{ ksi}$)

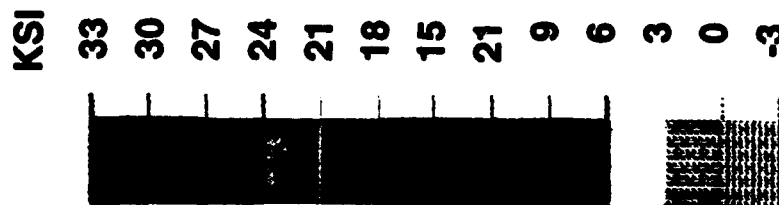
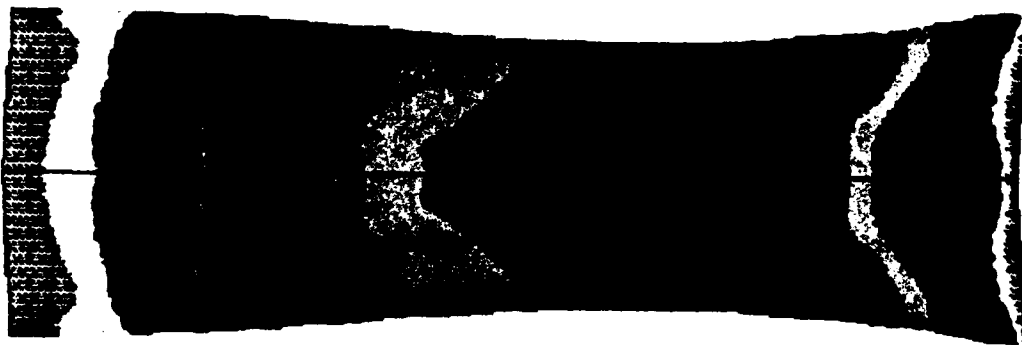


Figure 26. Elastic-Viscoplastic Lexan Slug
 Axial Stress at $t = 160 \mu s$ ($p_{max} = 50 \text{ ksi}$)

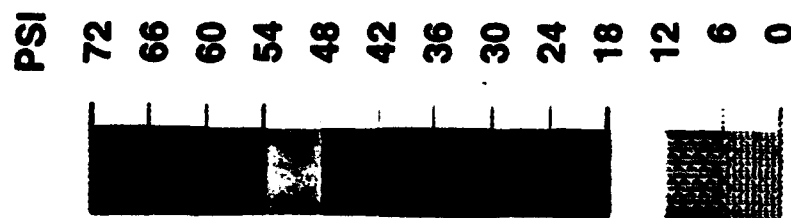
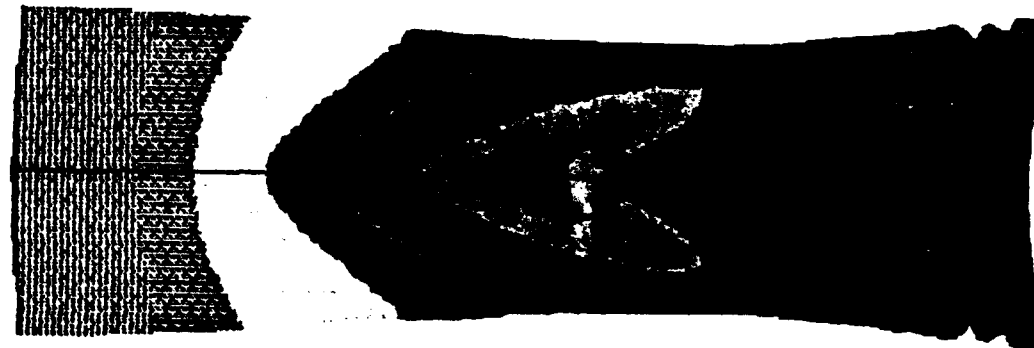


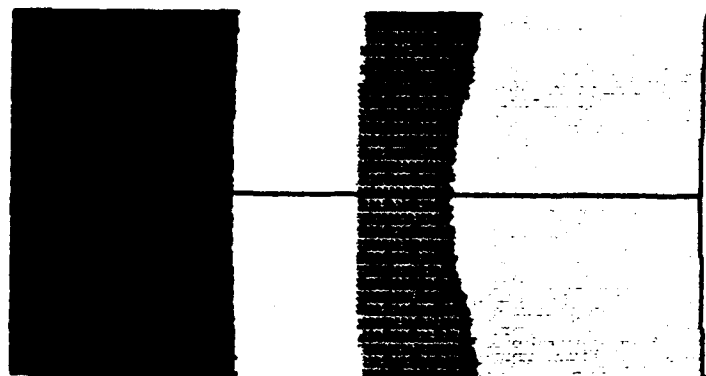
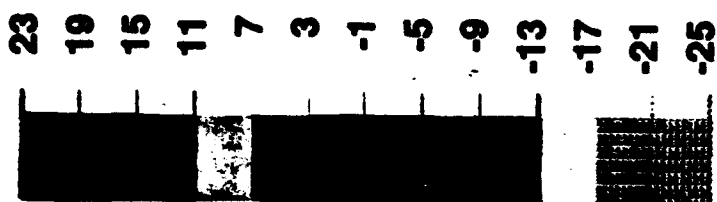
Figure 27. Elastic-Viscoplastic Lexan Slug
 Plastic Work at $t = 160 \mu s$ ($p_{max} = 50 \text{ ksi}$)

5.2.4 Viscoelastic-Viscoplastic

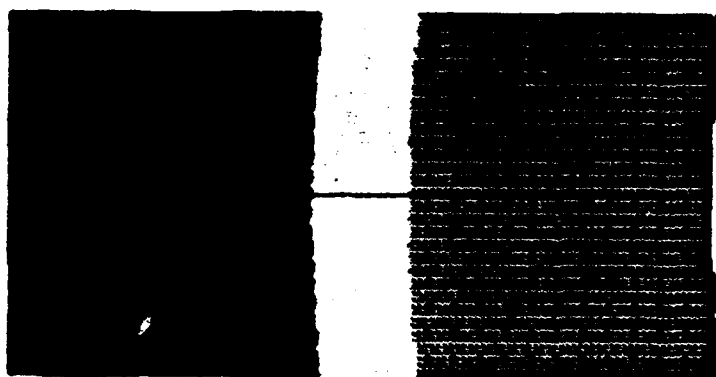
The simulation is again repeated but with the full viscoelastic-viscoplastic model. The additional damping significantly effects the results of these simulations. The time series of axial stress contours on the exaggerated deformation plots in Figures 28a through 28h show that the Lexan's elastic rebound is damped, with the result that a tensile wave appears only in the last stages of the deformation and is considerably smaller, peaking at around 7 ksi. This could explain why the Lexan slug never failed, even at peak loads of near 45 ksi. The speed at which the stress waves move across the slug also seems to be higher, but the reflected wave appears to have slowed somewhat. The plot of the acceleration and velocity of the center of mass in Figures 29a and 29b appear almost identical to the elastic case, indicating that the friction on the side wall changed only slightly. This is most likely due to the assumption the effective Poisson's ratio of the viscoelastic stiffness matrix is not changed. The velocity at the base of the sabot changes markedly, showing the expected damped behavior and only a slight change in the peak-to-peak period.

There is still some question of whether the timing of the reflection of the tensile wave is consistent with the duration of the pressure pulse. A definitive answer to this question could be carried out by using FEAMOD to model the entire system of the piston, water, and Lexan slug. This is certainly possible with the capabilities of FEAMOD, and we hope to examine this issue in the second phase of this effort. In addition, if the velocity or deformation history of the top of the sabot is measured, for example, with a fiber-optic interferometer in the brief time before the slug goes sailing, then a good measurement of the damping could be obtained with the help of the finite element model.

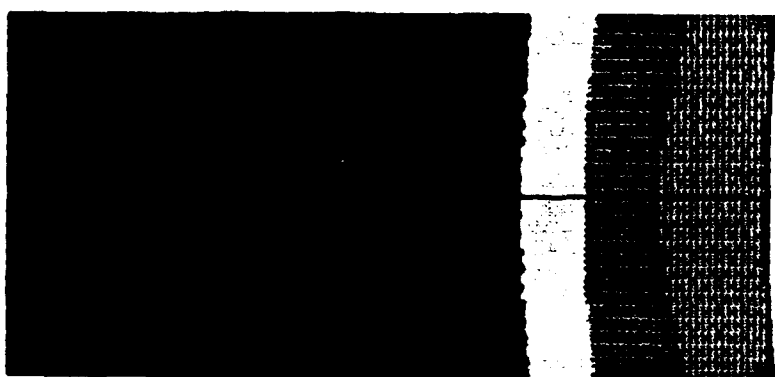
KSI



$t = 20 \mu s$



$t = 40 \mu s$



$t = 60 \mu s$



$t = 80 \mu s$

Figure 28. Viscoelastic-Viscoplastic Lexan Slug Axial Stress History ($p_{max} = 25 \text{ ksi}$)

KSI

23

19

15

11

7

3

-1

-5

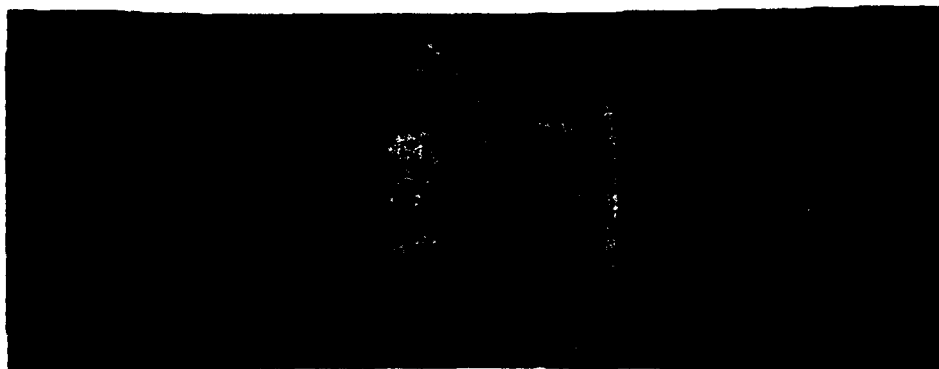
-9

-13

-17

-21

-25



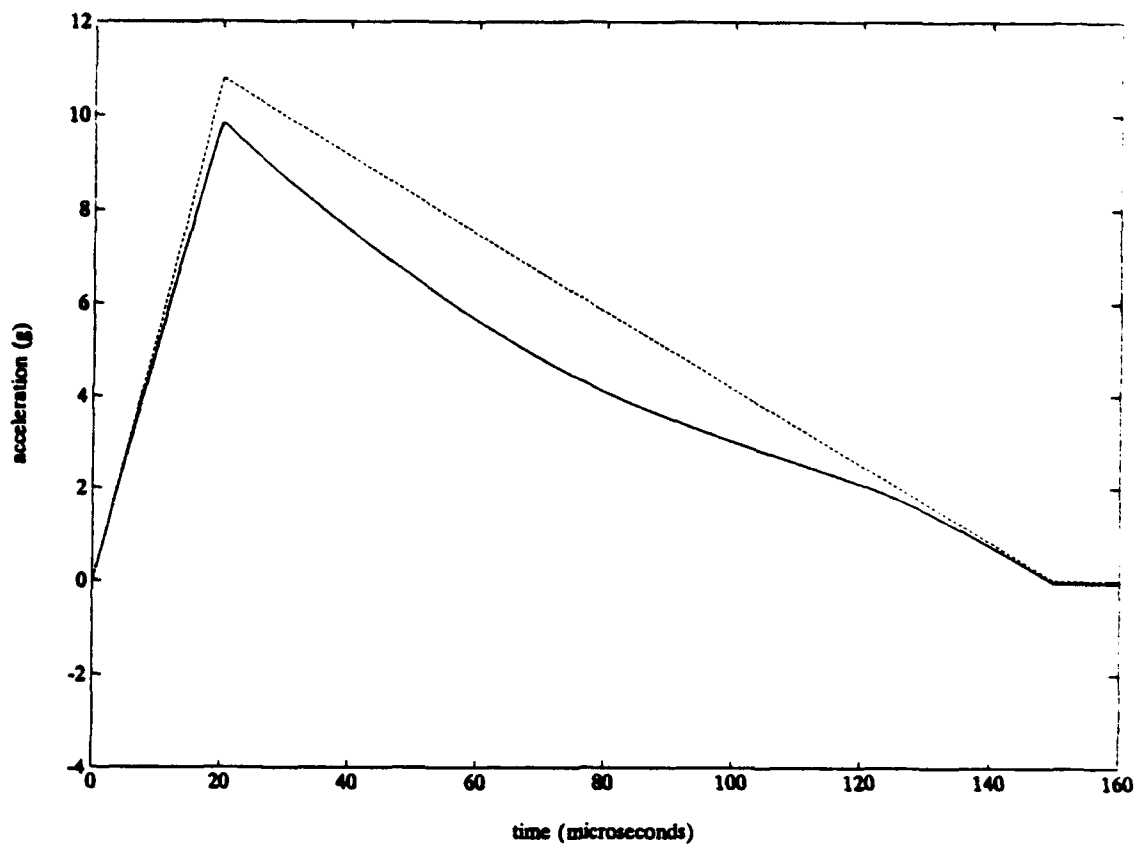
$t = 160 \mu s$

$t = 140 \mu s$

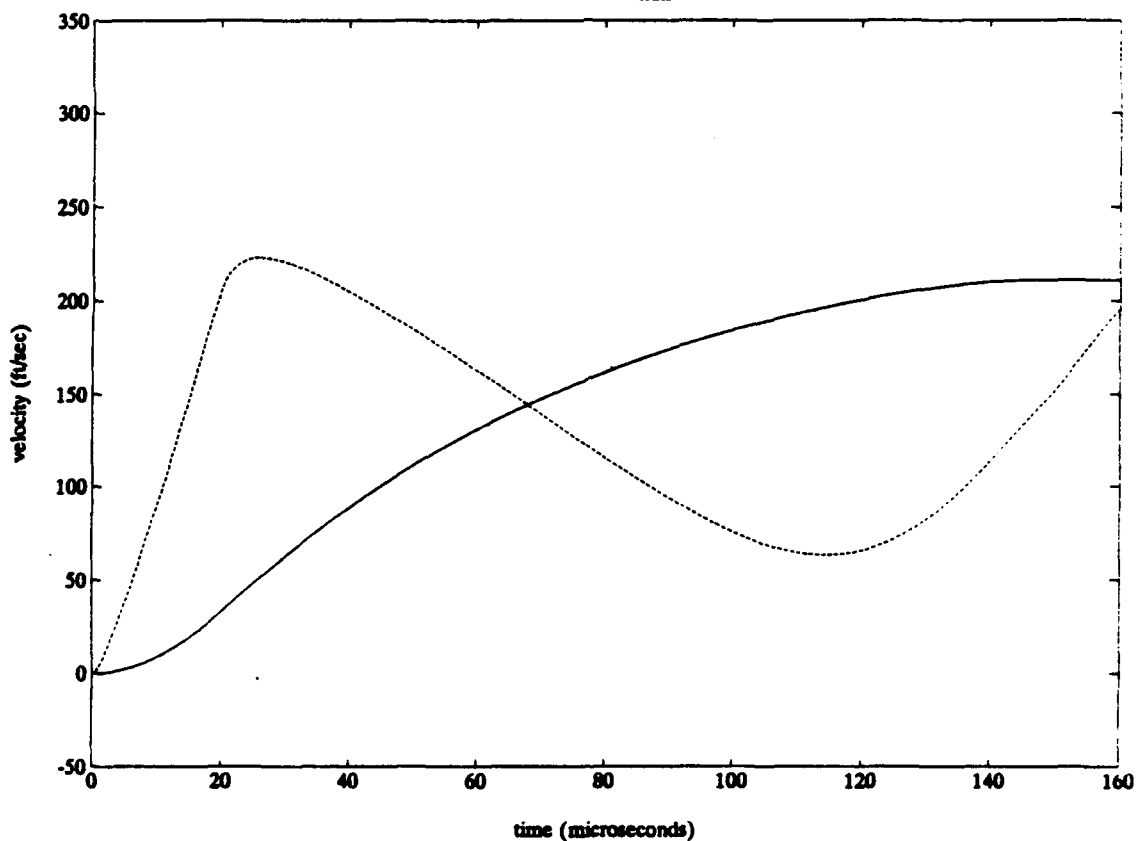
$t = 120 \mu s$

$t = 100 \mu s$

Figure 28. Viscoelastic-Viscoplastic Lexan Slug Axial
Stress History ($p_{max} = 25 \text{ ksi}$) (Cont.)



a. Acceleration ($p_{\max} = 25$ ksi)



b. Velocity ($p_{\max} = 25$ ksi)

Figure 29. Acceleration and Velocity of the Center of Mass (Viscoelastic-Viscoplastic Model)

6. CONCLUSIONS

A finite element model FEAMOD has been developed and tested. This model contains much of the essential physics for describing the dynamics of a projectile launched by a two-stage light-gas gun. In addition, FEAMOD may be used in conjunction with impact material tests to evaluate the material parameters important to the gas gun projectile dynamics. Capabilities added to FEAMOD under this effort include:

- A realistic constitutive model of the viscoelastic-viscoplastic behavior applicable to a variety of materials, including plastics and ductile metals. The viscoelastic-viscoplastic model accurately fits the experimental results of high-strain-rate impact tests of Lexan and aluminum.
- A contact friction element that differentiates between sticking contact, sliding contact, and no contact and comes with a decision matrix to move from one state to another. This contact element can be used to describe contact forces between the model/sabot and the barrel wall or between the interfaces within the model and the sabot. The contact friction element has been used to simulate a Lexan slug propelled by a water cannon tester. The model accurately describes the radial expansion of the Lexan surface into the bore, which in turn produces more friction. The model also accounts for the reduction of friction as the reflected tensile waves radially contract the Lexan, pulling the surface away from the bore.
- An erosion model to account for the ablating of the sabot surface at the barrel wall.
- A side-pressure-loading element that uses compressible flow relations to account for the pressure drop in any gas leaking around the ablated sides of the model/sabot.

FEAMOD comes with a stable time integrator for the temporal dynamics and state-of-the-art linear solvers for reducing the computation times and storage.

Several key issues identified in this effort are as follows:

- The duration of the spikes in the pressure history relative to the time required for sound to propagate through the solid projectile is an important factor in determining whether tensile waves will appear in the model. In an identical manner, the relative duration of the decompression ramp as the projectile exits the barrel determines if the projectile goes into tension. The spikes in the pressure history are related to gas shock waves impinging and reflecting off the base of the projectile. For the "pyro" model, finite element simulations indicate that tensile waves appeared in the aluminum for spike durations of less than about 0.1 ms. This duration is about half the spike duration predicted by the AEDC gas dynamics launch code. Considering any possible numerical damping in these models, the appearance of tensile waves in the projectile cannot be definitely ruled out. Careful numerical modeling of the gas dynamics should provide more definitive estimates of the spike and the exit decompression durations.

- Regardless of the question concerning tensile waves, the finite element analysis predicts significant compression yielding at the interface of the model and the sabot near the base of the model. FEAMOD quantifies the high stresses occurring at reentrant corners, interfaces, or gaps between the different parts of the model/sabot. Most of the yielding is associated with the peaks of the pressure spikes as opposed to the average load on the projectile. Plastic work appears to provide a rate-independent measure of the compression damage. Impact tests, in conjunction with the finite element analysis of the tests, could provide estimates of the critical plastic work, or the plastic work at the ultimate failure.
- The viscoplasticity tends to smooth the peak stresses by redistributing the load near regions that have yielded. The viscoelasticity damps the stress wave, whether the material is yielding or not, and inhibits the reflection of strong tensile waves. The degree of the damping depends on the viscous relaxation time. This relaxation time is an important parameter in describing the behavior of Lexan and nylon, and good estimates of its magnitude are needed.
- The wear of the Lexan inside the barrel is neither a linear function of position along the barrel nor the time after launch. This has implications on the current linear taper of the bore; more studies are needed to characterize the wear with more realistic pressure histories and actual bore tapers.
- Friction tends to increase the deviatoric stresses and increase the likelihood of failure, but it is a secondary influence unless the coefficient of friction is above 0.4.
- Side-pressure loads, as a result of gas leaking around the sides of the Lexan, reduce the shear stresses near the base and tend to move the maximum shear load closer to the top of the sabot and in the model.
- The most plausible explanation of the cause of projectile ballating is attributed to turbulent structures generated at the base of the projectile as shock waves reflect from the surface. If these structures have length scales of the size of the bore radius and if the pressure variations within these structures are of the same magnitude of the shock pressure rise, then large torques can be expected. Furthermore, if the projectile has eroded, then these torques could produce high yawing velocities to impact the bore wall. Modeling the effects of the barrel taper on the erosion is important if the designs to prevent possible ballating are to be analyzed.

Several practical issues in the use of FEAMOD have also been identified:

- Regions with reentrant corners, gaps, and interfaces must be meshed sufficiently fine to avoid numerical instabilities associated with the nonlinear viscoplastic model.
- Since projectiles launched at the AEDC facilities generally have a fairly complex geometry, a preprocessor with good "automated meshing" capabilities is imperative if such analyses are to be manpower effective. Also, if the analyst is to quickly view the temporal results, automation in the postprocessor is important. It is recommended that in Phase II, an evaluation of commercial pre/postprocessors be conducted to decide which is most appropriate for AEDC personnel and the FEAMOD software.

- The iterative solver provides substantial improvements over the usual direct solver in terms of memory and CPU time. The iterative solver currently in FEAMOD, however, is not applicable to the sliding/sticking contact element. Since the advantages of the iterative solver will be especially crucial for the quick analysis of complicated projectile geometries, it is recommended that a modified iterative solver be incorporated into FEAMOD in Phase II.
- Temporal elastic solutions using grids with near 3000 degrees of freedom over a pressure history of 0.4 ms require a little over one megabyte and about 30 minutes on the 386/387. Elastic simulations over the duration that the projectile resides in the barrel would require about 8 hours. Nonlinear simulations would increase the cost of a full simulation to about 24 hours. With complicated geometries and finer meshes, the run times will be longer, and the analysts may not be satisfied with this turnaround. Therefore, we recommend that FEAMOD be ported to a computer with a RISC architecture. For example, the same elastic simulation over the full duration on an IBM RISC 6000 would require about 10 minutes!! Since FEAMOD makes no system calls and is written entirely in FORTRAN, portability is not a problem.

To conclude, this effort has met or exceeded all the Phase I technical objectives set out in the proposal and demonstrates the feasibility of the proposed approach for realistic dynamic stress analysis of projectiles accelerated by a two-stage light gas gun.

REFERENCES

- Anderson, J. D. Jr. (1982) *Modern Compressible Flow*, McGraw-Hill.
- Bathe, K.-J. (1982) *Finite Element Procedures in Engineering Analysis*, Prentice-Hall, Inc., Englewood Cliffs, New Jersey.
- Bathe, K.-J., and Chaudhary, A. (1985) "A Solution Method for Planar and Axisymmetric Contact Problems," *Inter. J. for Numerical Methods in Engineering*, Vol. 21, pp. 65-85.
- Bodner, S. R. (1984) "Review of a Unified Elastic-Viscoplastic Theory," Interim Scientific Report on Grant AFOSR-84-0042, published as a chapter in *Unified Constitutive Equations for Plastic Deformation and Creep of Engineering Alloys*.
- Bodner, S. R., and Partom, Y. (1975) "Constitutive Equations for Elastic-Viscoplastic Strain Hardening Materials," *Journal of Applied Mechanics*, Vol. 42, p. 385.
- Bowden, F. P. and Tabor, D. (1964) *The Friction and Lubrication of Solids: Part II*, Oxford University Press, pp. 472-478.
- Katona, M. G. (1983) "A Simple Contact-Friction Interface Element with Applications to Buried Culverts," *International Journal for Numerical and Analytical Methods in Geomechanics*, Vol. 7, 371-384.
- Kollé, J. J. (1991) "Impact Tester for Hypervelocity Projectiles: Phase I Final Report," QUEST Technical Report No. 549.
- Mueller, A. C. (1986) "FEAMOD, A Modifiable Finite Element Analysis Program," Flow Research Report No. 381.
- Oppe, T. C., Joubert, W. D., and Kincaid, D. R. (1988) "NSPCG User's Guide Version 1.0: A Package for Solving Large Sparse Linear Systems by Various Iterative Methods," Center for Numerical Analysis, The University of Texas at Austin, CNA-216, April.
- Powell, E. S., Winstead, C. A., DeWitt, J. R., and Cable, A. J. (1985) "A Preliminary Study of Model Wear in A Two-Stage Light-Gas Launcher," Presented at the 36th Meeting of the Aeroballistic Range Association, Southwest Research Institute, October.
- Shapiro, A. H. (1953) *The Dynamics and Thermodynamics of Compressible Fluid Flow*, John Wiley & Sons.
- Tardif, H. P. and Marquis, H. (1963) "Some Dynamic Properties of Plastics," *Canadian Aeronautics and Space Journal*, pp. 205-213, September.
- Vassiliou, M., Salvado, C. A., and Tittmann, B. R. (1984) "Seismic Attenuation," Chapter 5 in *Handbook of Physical Properties of Rocks*, Vol. III, CRC Press, Boca Raton, Florida.
- Zienkiewicz, O. C. (1977) *The Finite Element Method*, McGraw-Hill, London.

APPENDIX A

FEAMOD USER'S GUIDE

FEAMOD has undergone many extensions and revisions since the last update of the user's guide (Mueller, 1986), the most notable being the revisions made when it was placed on the 386/387 and with the addition of the iterative solver. Section A.1 of this appendix gives the 1987 FEAMOD User's Guide. Section A.2 gives the amendments to this user's guide.

A.1 1987 FEAMOD User's Guide

The FEAMOD User's Guide, as published in Mueller (1986), is provided on the following pages, labeled pages 78 through 90 of document FD-TR-1001. The next section of this appendix then continues after page 90.

4. FEAMOD USER'S MANUAL

This section serves as the User's Manual for the FEAMOD code; it is meant to be both a reference and a guide for using the code. Input formats and the use of the macro commands to set up and solve problems are explained here.

There are two important aspects of running the code: 1) the size of the M array. The code checks to make sure the array is large enough for the problem by comparing the size of the variable MAX in the main program EXEC against the markers used in M. The code sets up these array markers during input as the storage requirements for the problem arrays are determined from input variables. Thus, it is important that the variable MAX be given the same value as the dimension of M. This allows the code to check the problem size and to stop, if necessary. 2) The precision level of variables in the code. There is a variable IPR set in BLOCK DATA that is the ratio of the real variable size to the integer variable size, which is very important for assigning addresses in the M array. The size of variables is most easily determined by the number of bits or bytes in the variable word. The variable IPR must be an integer amount. Usually, it has a value of 2 for both single- and double-precision situations; however, the operator should make sure the correct value for IPR is being used.

The following sections describe the format of the input files MACRO, PROBLEM, and MATERIAL.

4.1 File Description

FEAMOD requires seven input/output files, of which four are output files, three are files input by the user, and one is a file set up by the execution of SUPERTAB. The following sections describe these files.

4.1.1 MACRO File and Executive Macro Commands

The MACRO file is the first file read by the code. The main program begins by reading the MACRO file. The first card in the file is the problem title card shown below.

Problem Title Card

Card 1 FORMAT (20A4)

<u>Column</u>	<u>Description</u>	<u>Variable</u>
1-80	Problem title used in printout	HEAD (1-20)

The rest of the MACRO file is used to input the executive and analysis macros. The analysis macro commands direct the solution steps to be performed by the code. They follow the ANALYS executive macro in the MACRO file and are described in Section 4.3 of this report.

The executive macros are listed below. Macro commands must begin in column one. Two F10.0 variables read in are used to specify which dump sets the code will read or write. The INPUT and the ANALYS executive macros have certain automatic dump read or write operations. The first F10.0 field specifies which dump set is to be read by these automatic operations, the second specifies which one is to be written. The INPUT section automatically writes data it has read into the dump set specified by the executive macro. Future capabilities of the code will allow the INPUT routine to read in the specified dump set, modify the data using input macro commands, and write the new set of data to a specific dump set.

Executive Macros

(Format(2A4,2X,2F10.0))

<u>Macro</u>	<u>Description</u>
INPUT	Begins the data input section. Transfers program control to the INPUT routine which reads from the PROBLEM file.
ANALYS	Begins the problem analysis section. Transfers program control to PMACR which reads the analysis macros. These macros direct the solution steps to be performed by the code and are described in Section 4.3. The analysis macros are read from the MACRO file immediately following the ANALYS executive macro command.
REPORT	Begins the report section. Transfers program control to the REPORT routine. Currently, this routine uses only the printing analysis macros. These macros are read from the MACRO file immediately following the REPORT executive macro.
STOP	Terminates program operation.

4.1.2 PROBLEM File

The PROBLEM file is used to input data needed to set up a problem. The code begins reading from this file after either the INPUT executive macro or the MESH analysis macro is executed.

The file begins with several problem definition cards (see description below) that are read by the INPUT routine. This data is used initially in setting array storage sizes and, later, in running the problem. Input macro commands follow the problem definition cards.

Problem Definition Cards

Card 1 FORMAT (20A4)

<u>Column</u>	<u>Description</u>	<u>Variable</u>
1-80	Convenience title (may contain anything)	TITLE (1-20)

Card 2 FORMAT (20A4)

<u>Column</u>	<u>Description</u>	<u>Variable</u>
1-80	Convenience title used to describe the next line of input; this card is usually "NUMNPNUMELNUMAT NDM NDF NEN NAD"	TITLE (1-20)

Card 3 FORMAT (7I5)

<u>Column</u>	<u>Description</u>	<u>Variable</u>
1-5	Total number of nodes in the problem	NUMNP
6-10	Number of grid elements	NUMEL
11-15	Number of element groups	NUMAT
16-20	Number of spatial dimensions (max = 3)	NDM
21-25	Number of unknowns per node (max = 6)	NDF
26-30	Maximum number of nodes per element	NEN
31-35	Added size to element matrices in excess of NDF*NEN (for nodeless variables)	NAD

Card 4 FORMAT (20A4)

<u>Column</u>	<u>Description</u>	<u>Variable</u>
1-80	Convenience title used to describe the next line of input; this card is usually "LSYMLSTATNMASSLMOVE SECOND"	TITLE (1-20)

Card 5 FORMAT (2L5,I5,L5)

<u>Column</u>	<u>Description</u>	<u>Variable</u>
1-5	True, if stiffness matrix is symmetric	LSYMM
6-10	True, if the problem is static	LSTAT
11-15	Describes the mass matrix = 0 for no mass matrix = 1 for lumped mass matrix = 2 for consistent mass matrix	NMASS
16-20	True, if the X-coordinate array is to be updated after each solution (this is almost always true)	LMOVE
21-25	True if the problem is second order-in time	SECOND

4.1.3 MATERIAL File

The MATERIAL file is used to input element material data that is required by the MATE input macro command; its particular format depends on the particular element. See Section 6 for the format of each element.

4.1.4 UNIVERSAL File

The UNIVERSAL file is an input file that contains data which defines the grid, element types, loading, and boundary restraints. This file may be generated via the Model Creation Module of SUPERTAB. Information on the file is accessed by the input macro commands COOR, ELEM, BOUN, FORC, and TEMP.

4.1.5 DUMP File

The DUMP file is an unformatted output file that is essentially a dump of the contents in the memory of a FEAMOD run. A new dump file is created for each analysis DUMP macro command. The individual dump files are distinguished by appending an index to the dump file name. The DUMP file is especially useful for re-starting lengthy calculations.

4.1.6 REPORT File

The REPORT file is a formatted output file that records the results of the analysis and any error messages. If requested, the input data is also recorded on this file. The REPORT file is generated through the analysis macro commands - PRTC, PRTG, PRTK, PRM, PRTR, PRTV, AND REAC.

4.1.7 ANALYSIS File

The ANALYSIS file is a formatted output file that writes analysis data in a universal file format so that it may be read by SUPERTAB. The ANALYSIS file is generated through the UNIV analysis macro command.

4.2 Input Macro Commands

The input macro commands are found in the MACRO file (see 4.1.1). The subroutine PMESH is called by the INPUT routine after the problem definition cards are read. Then, PMESH reads the input macro commands, which are listed below. Each macro directs PMESH to read a data set.

Input Macro Commands

(Format(A4))

<u>Macro Command</u> (Columns 1-4)	<u>Description of</u> <u>the Input Data</u>
COOR	Grid coordinate data
ELEM	Grid element numbering data
BOUN	Boundary restraint data
FORC	Prescribed nodal force data
TEMP	Nodal state variable data
MATE	Element group data; directs program to read input information from the IOMATL file.
PAGE	Read in carriage control variable.
PRIN	Print subsequent input data (default mode).
NOPR	Do not print subsequent input data.
END	Ends input macro string (required); returns the code to the executive macro level in MACRO.

Input macro commands can appear in any order except for END, which must be the last command. COOR, ELEM, MATE, and END must always be used, but use of the other macros is optional. Blank cards are allowed between input macros. However, some macros must be followed by a specific set of input cards, and, in these cases, where a blank card may have a special meaning. In particular, COOR, ELEM, BOUN, FORC, TEMP, MATE, and PAGE require input data in specific formats. For this reason, the data arrays for the BOUN, FORC, and TEMP macros are first zeroed, in case they are not used. Each of these macros is discussed in more detail under its own subheading in this section. The PRIN, NOPR, and END macros require no data.

4.2.1 COOR Input Macro Command

The COOR input macro is used to direct the program to read nodal coordinate data from the UNIVERSAL file. This macro will cause the program to search the UNIVERSAL file for a data set = 15 (nodes) and read in all data. For axisymmetric problems, the Y axis is the axis of symmetry, and X is treated as the radius.

4.2.2 ELEM Input Macro Command

The ELEM input macro is used to direct the program to read data from the UNIVERSAL file that defines the grid element connectivity, element type, and material type. This macro will direct the program to search the UNIVERSAL file for data set = 71 (connectivity).

4.2.3 BOUN Input Macro Command

The BOUN input macro directs the program to read the UNIVERSAL file for data defining the prescribed restraints. It searches for the data set = 89 (restraints).

4.2.4 FORC Input Macro Command

The FORC input macro directs the program to read data from the UNIVERSAL file that define the nodal loading forces. It searches the UNIVERSAL file for data set = 90 (loadsets).

4.2.5 TEMP Input Macro Command

The TEMP input macro directs the program to read the UNIVERSAL file for nodal state variable data (a scalar value). It searches the file for data set = 55 (analysis data at nodes).

4.2.6 MATE Input Macro Command

The MATE input macro is used to input the element routine number and the necessary data for each element group. When the MATE macro command is encountered, the code begins reading from the MATERIAL file.

The MATE macro needs a set of input cards for each element group. There must be no blank cards for this macro. The first two cards for each element group are read by the PMESH routine. The first card is a convenience title card and the second card contains the element group number, MGRP, and the element routine number for this group, IEL. Then, the element routine number, IEL, is called to read in the rest of the input cards for this element group. The cards may vary depending on the element routine used. It is important to remember that the main purpose of this call to the element routine is to fill the C array.

MATE Macro Data Cards

Card 1 Format(20A4)

<u>Column</u>	<u>Description</u>	<u>Variable</u>
1-80	Convenience title used to describe the next input lines. Usually this card is "GROUP ELnn OPTIONAL ELEMENT TITLE"	TITL(1-20)

Card 2 Format(2I5)

<u>Column</u>	<u>Description</u>	<u>Variable</u>
1-5	Element group number	MGRP
6-10	Element routine number assigned to this element group	IEL

4.2.7 PAGE Input Macro Command

The PAGE input macro is used to read in a vertical spacing carriage control variable. A default value is provided (see below), so this macro does not have to be used. If used, there is only one data card required, and it must immediately follow the macro command (blank cards may follow the data card). The card contains the carriage control variable, 0, read with the format (A1). The variable is used to control the vertical formatting of the beginning of major blocks of output. The values given to 0 may depend on the compiler and printer used, but typical values are:

blank = start on next line (single spacing)
0 = skip a line and then start (double spacing) (default)
1 = start on first line of next page
+ = start where the printer pointer is currently located
(no advance)

4.3 Analysis Macro Commands

The analysis macro commands are used to define the solution steps for a problem. They are input on the MACRO file following the ANALYS executive macro command. A complete list of these macros appears below. The input format for these macros requires that they begin in column 1. Restrictions or warnings on the use of these variables, if any, for a particular macro command are described in the list below. The use of these macros in the solution of particular problems is explained in the next section.

Analysis Macro Commands Format (2A4, 2X, 2F10.0)

CONR - Performs convergence check on δR .
CONU - Checks for $||\delta|| < \text{tolerance } ||\Delta U||$.
DATA - Reads in a value for THETA (θ)

Analysis Macro Commands (Cont.)

DISP	- Prints the nodal coordinates, displacements, velocities, and accelerations.
DT	- Sets desired time step Δt .
DUMP	- Dumps the storage for a future restart or report.
EIGE	- Solves for λ and \underline{U} and prints results.
END	- Returns to executive macros.
EXCD	- Solves for \underline{A} .
FORM	- Forms $\underline{R}_{bc} - \underline{P}$.
FORMA	- Forms $\underline{R}_{bc} - \underline{P} - \underline{MA}$.
INIT	- Checks Jacobian of element coordinates for + sign.
LOOP	- Begins loop.
MASS	- Forms \underline{M} .
MASSV	- Forms $\underline{M} + \frac{\Delta t}{2} \underline{C}$.
MESH	- Allows re-inputting of a portion of the problem definition file.
MOVE	- Updates the nodal coordinates.
NEXT	- Ends loop.
NOPR	- Sets flag to not print macro commands (default).
PRIN	- Sets flag to print the macro commands as they occur.
PROP	1. - Reads one line of proportional load data from below END macro. (The number 1 is input in the first F10.0 field.)
PRTC	- Prints control variables.
PRTG	- Prints the variables stored at the Gauss points.
PRTK	- Prints effective stiffness matrix.
PRTM	- Prints effective mass matrix.
PRTR	- Prints contents of DR vector (states whether it is the out-of-balance load vector, $\delta \underline{R}$, or the displacement update vector, $\underline{\delta}$).
PRTU	- Prints the DU vector, $\Delta \underline{U}$.
REAC	- Calculates and prints the nodal reactions for \underline{P} (use only after CONV or CONU and before UPDA).
REACA	- ditto for $\underline{P} + \underline{MA}$
SOLV	- Solves for $\underline{\delta}$ and updates $\Delta \underline{U}$ and \underline{U} .

Analysis Macro Commands (Cont.)

SSS	- Updates \underline{V} for steady-state ice calculations.
STIF	- Forms \underline{K} .
STIFA	- Forms $\underline{K} + \frac{6}{\theta^2 \Delta t^2} \underline{M}_s$
STIFCN	- $\theta \underline{K} + \frac{1}{\Delta t} \underline{B}$
STIFV	- Forms $\underline{K} + \frac{1}{\Delta t} \underline{C}$.
STIFVA	- Forms $\underline{K} + \frac{3}{\theta \Delta t} \underline{C} + \frac{6}{\theta^2 \Delta t^2} \underline{M}$.
STRE	- Calculates and prints stresses and strains at the Gauss points. (Note that since calculations are done for this macro, the kinematic variables and initial stresses must be consistent; use before UPDA macro).
TIME	- Increments time.
TOL	- Sets convergence tolerance.
UPDA	- Updates the state variables stored in the GP array.
WIL1	- Prepares a consistent estimate for the kinematic variables at time $t + \theta \Delta t$.
WIL2	- Updates \underline{V} and \underline{A} .
WIL3	- Interpolates kinematic variables back to time $t + t$.
WIL4	- Makes new estimate for acceleration at time $t + t + \Delta t$
UNIV DISP	- Writes displacement type variables to a UNIVERSAL file
UNIV STRE	- Writes stress type variables to a UNIVERSAL file
UNIV REAC	- Writes reaction type variables to a UNIVERSAL file

4.4 Problem-Solving Methods

In this section, specific types of problems are presented along with the analysis macro string required to solve the problem. Note that these macro strings are only the necessary commands needed to solve the problem. Other macros, such as parameter-defining macros, printout macros, and dump macros, can be placed where needed within these strings. Be sure, however, to heed any restrictions or warnings on the use of these macros given in the complete list of analysis macros in Section 4.3.

4.4.1 Static Problems

Static problems may be solved using either the Newton iteration technique or the incremental load method.

4.4.1.1 Newton Iteration Technique

Static problems having equations of the form

$$\underline{P} = \underline{R}_{bc} \quad (4.4.1)$$

can be solved using the Newton iteration technique. It is assumed that the velocity, acceleration, and mass tensors are unnecessary for a static problem. The form of this equation actually solved by Newton's method is

$$\underline{K}\underline{\delta} = \underline{R}_{bc} - \underline{P} \quad , \quad (4.4.2)$$

where $\underline{\delta}$ is the correction increment of the displacement and \underline{P} is the nodal internal stress vector. The necessary macro string to solve this type of problem is

LOOP	- Begins iteration loop.
STIF	- Forms \underline{K} .
FORM	- Forms $\underline{R}_{bc} - \underline{P}$.
SOLV	- Solves for $\underline{\delta}$ and updates $\Delta\underline{U}$ and \underline{U} .
CONU	- Checks for $ \underline{\delta} < \text{tolerance } \Delta\underline{U} $.
NEXT	- Ends iteration loop.
END	- Returns to executive macros.

4.4.1.2 Incremental Load Method

An alternate method for solving static structural problems that is particularly well suited for plasticity is the incremental load method. The program does not iterate at each step to achieve convergence but performs a displacement correction resulting from incrementally increasing the load. The form of the equation solved is

$$\underline{K}\underline{\delta} = \underline{R}_{bc} - \underline{P} \quad . \quad (4.4.3)$$

The necessary macro command string to solve this problem by incrementing the load is

PROP 1. - Reads one line of proportional load data which has been inserted following the END macro command.
(or using MESH macro after TIME macro).

LOOP	- Begins artificial time loop.
TIME	- Increments artificial time and zeros out $\underline{\delta}$.
LOOP	- Begins iteration loop.
STIF	- Forms \underline{K} .
FORM	- Forms $p(\underline{R}_{bc} - \underline{P})$, where p is the proportional load factor.
SOLV	- Solves for $\underline{\delta}$ and updates $\Delta \underline{U}$ and \underline{U} .
CONU	- Checks for $ \underline{\delta} < \text{tolerance } \Delta \underline{U} $.
NEXT	- Ends iteration loop.
UPDA	- Updates state variables.
NEXT	- Ends artificial time loop.
END	- Returns to executive macros.

A variety of loading histories can be applied with the form of the proportional load factor expression presently available:

$$p = A_1 + A_2 t + A_3 \sin(A_4 t + A_5)^L \quad (4.4.4)$$

where the A_i coefficients are read from the proportional load data, along with the exponent L and upper and lower limits on time.

4.4.2 Dynamic Structural Problems

Dynamic structural problems can be solved using either the explicit central-difference time method, or the Wilson- θ implicit time integration method coupled with Newton's iteration technique.

4.4.2.1 Explicit Central-Difference Time Integration Method

Dynamic structural problems can be solved using an explicit central-difference time integration method. The form of the equation solved in this case is

$$\underline{M} \underline{\ddot{A}} = \underline{R}_{bc} - \underline{P} \quad , \quad (4.4.5)$$

where \underline{M} is the global mass matrix. Note that there are limitations on the step size for this type of problem (see Section 2.4.1). The necessary macro string to solve this problem for accelerations, velocities, and displacements is

MASS	- Forms \underline{M} .
LOOP	- Begins time-step loop.

FORM - Forms $\underline{R}_{bc} - \underline{P}$.
 EXCD - Solves for \underline{A} . Updates all kinematic variables.
 NEXT - Ends time-step loop.
 END - Returns to executive macros.

4.4.2.2 Wilson-θ Method

Dynamic structural problems having an equation of the form

$$\underline{M}\underline{\ddot{A}} + \underline{P} = \underline{R}_{bc} \quad (4.4.6)$$

can be solved using the Wilson-θ implicit time integration method coupled with Newton's iteration technique. This equation is solved for a time step that is 1.4 times larger than the desired time step. After getting the solution at this long time step, the solution at the desired time is found by interpolation using Wilson's assumption of linear variation of acceleration with time. The form of the equation that is actually solved is

$$\left(\underline{K} + \frac{6}{\theta^2 \Delta t^2} \underline{M} \right) \underline{\delta} = \underline{R}_{bc} - \underline{P} - \underline{M}\underline{\ddot{A}} \quad (4.4.7)$$

where θ is Wilson's theta (=1.4) and $\underline{\delta}$ is again the correction increment of the displacement. The necessary macro string to solve this type of problem is

LOOP - Begins time-step loop.
 WIL1 - Prepares a consistent estimate for the kinematic
 variables at time $t + \Delta t$.
 LOOP - Begins iteration loop.
 STIFA - Forms $\underline{K} + \frac{6}{\theta^2 \Delta t^2} \underline{M}$.
 FORMA - Forms $\underline{R}_{bc} - \underline{P} - \underline{M}\underline{\ddot{A}}$.
 SOLV - Solves for $\underline{\delta}$ and updates ΔU and U .
 CONU - Checks for || || tolerance || U||.
 WIL2 - Updates V and A .
 NEXT - Ends iteration loop.
 WIL3 - Interpolates kinematic variables back to time $t + t$.
 UPDA - Updates the state variables stored in the GP array.
 WIL4 - Makes new estimate for acceleration at time $t + \Delta t + \theta t$.
 NEXT - Ends time-step loop.
 END - Returns to executive macros.

4.4.3 Evaluation of Fundamental Eigenvalue

The determination of the dominant (smallest) eigenvalue of the problem

$$\underline{K}\underline{U} = \lambda \underline{M}\underline{U} \quad , \quad (4.4.8)$$

where λ is the dominant eigenvalue, is determined by inverse iteration using the following string of macro commands:

```
STIF      - Forms  $\underline{K}$ .
MASS      - Forms  $\underline{M}$ .
EIGE      - Solves for  $\lambda$  and  $\underline{U}$  and prints results.
END       - Returns to executive macros.
```

Following these macros, the \underline{U} vector contains the normalized eigenvector corresponding to the dominant eigenvalue.

4.4.4 Dynamic First-Order Time Problems

Dynamic first-order time problems having an equation of the form

$$\underline{B} \frac{d\underline{U}}{dt} + \underline{P} = \underline{R}_{bc} \quad (4.4.9)$$

can be solved using the Crank-Nicolson technique. The form of the discrete equation solved is

$$\left(\frac{\underline{B}}{\Delta t} + \theta \underline{K} \right) \underline{\delta} = \underline{R}_{bc} - \underline{P} \quad (4.4.10)$$

where $\underline{\delta}$ is the increment of the displacement between time steps. The necessary macro string to solve this type of problem is

```
LOOP      - Begins time step loop
STIFCN    - Forms  $\frac{1}{\Delta t} \underline{B} + \theta \underline{K}$ 
FORM      - Forms  $\underline{R}_{bc} - \underline{P}$ 
SOLV      - Solves for  $\underline{\delta}$  and updates  $\underline{U}$ 
NEXT      - Ends iteration loop
UPDA      - Updates the state variables stored in the GP array
NEXT      - Ends time step loop
END       - Returns to executive macros
```

If the problem is linear, the STIFCN command can appear outside the time loop.

A.2 FEAMOD Amendments

A.2.1 I/O Files

FEAMOD now uses 10 files that are stored under a common name (NAME) with different extensions in the subdirectory DF\ (Data File).

Input files (formatted):

Macro command file	DF\NAME.MAC
Problem definition file	DF\NAME.PRO
Grid definition file	DF\NAME.GRD
Material definition file	DF\NAME.MAT

Output files (formatted):

Report output file	DF\NAME.RPT
Analysis output file	DF\NAME.ANL
Summary output file	DF\NAME.SUM

Input/output files (unformatted)

Memory Dump file	DF\NAME.DMP
Nodal Point Dump file	DF\NAME.NOD
Gauss Point Dump file	DF\NAME.GAU

Most of these files are described in Mueller (1986); the new files are defined as follows:

Summary Output File

This file contains a a brief summary of selected variables determined by the code. Its output varies depending on the type of elements used. For this project, the summary file contains the history of center of mass variables, z position, velocity, acceleration, and the position and velocity of a selected point.

Nodal Point Dump File

This binary input/output file contains the nodal results for all degrees of freedom. It is generally used to transfer nodal data between different runs that use the same grid but apply different boundary conditions or different problem types. In this effort, the nodal dump file has been used to transfer deformation and constraint forces from a static run to be used as initial conditions in a dynamic run.

Gauss Point Dump File

This binary input/output file contains Gauss point results for all elements in the grid. It is similar to the nodal point dump file in that it is generally used to transfer Gauss point data between different runs that use the same grid but apply different boundary conditions or problem types. In this effort, the nodal dump file has been used to transfer stress, strain, and other quantities from a static run to be used as initial conditions in a dynamic run.

A.2.2 Macro Commands

Some of the macro commands have been modified and there are several additional macro command since the documentation of Mueller(1986). The modified commands are:

SOLV TOL

With the addition of the iterative solver, the SOLV command also provides a relative tolerance (TOL) that the iterative solver must reach before the solution is considered converged.

CONRABS TOL

The CONR command has a second word extension of CONR that commands FEAMOD to compute the absolute norm of the residual. If the absolute residual norm is less than TOL, then the Newton's iteration is considered converged.

CONUABS TOL

The CONUABS command is identical to the CONRABS command except the convergence test is on the absolute normal of the change in the nodal values in the last iteration.

WRTX

The WRTX command instructs FEAMOD to write out data to either the DF\NAME.NOD or the DF\NAME.GAU file. It has several second word extensions:

WRTXDISP

Write all nodal data to the DF\NAME.NOD.

WRTXVEL

Write all nodal rate of change data to the DF\NAME.NOD.

WRTXACC

Write all nodal rate of rate of change data to the DF\NAME.NOD.

WRTXSTRE

Write all Gauss point data to the DF\NAME.GAU.

REDX

The REDX command is identical to the WRTX command except it instructs FEAMOD to read data from either the DF\NAME.NOD or the DF\NAME.GAU file. It has identical second word extensions:

REDXDISP

REDXVEL

REDXACC

REDXSTRE

Another versatile addition to the FEAMOD command library is the WILD command. WILD is a wild card command that takes on its meaning depending on the particular elements used. This command instructs FEAMOD to call a user-definable routine called WILD. In this effort, the wild card command has been used to compute and update the position and velocity of the center of mass. Since this requires integration, the WILD command instructs the elements to carry out this integration with a Gaussian quadrature.

PRTG is no longer a command supported by FEAMOD. The stress type variables (variables that are stored at the GAUSS points) may be written unformatted with the WRTXSTRE command or they may be interpolated to the nodal points and written formatted with the UNIVSTRE.

A.2.3 Element Library

The elements described in the following are elements developed specifically for this effort. Some are modified versions of previous elements and others are completely new elements.

ELMT24

This is an axisymmetric, linear, isotropic, thermo-elastic infinitesimal strain element. The element accepts all two-dimensional element types in the FEAMOD library. The data definition and format of the data in the material file is as follows:

card 3 FORMAT(20A4)

Convenience title usually "YOUNG POISSON DENSITY CTE"

card 4 (free format)

E , ν , ρ , CTE

card 5 FORMAT(20A4)

Convenience title usually "NGAUSS"

card 6 free format

integer order of Gaussian integration

ELMT25

This is a one-dimensional, axisymmetric 3-node element that enforces the general contact/free constraints for contact with a stiff wall aligned in the axial direction. The element also computes the erosion rate based on Equation (42) to determine the total radial nodal erosion. The local element order is shown in Figure A.1 with the node number 3 having the largest axial value. The radial coordinates of the nodes need not be equal. The data definition and format of the data in the material file is as follows:

card 3 FORMAT(20A4)

Convenience title usually "YOUNG EPS RADIUS XMU0 V0 POWER RHO H"

card 4 (free format)

$E, \epsilon, R, \mu_o, v_o, \rho, H$

where each variable is defined as

E : Young's modulus of contacting body

ϵ : ratio of young's modulus of contacting body and rigid wall

R : radius of rigid wall

μ_o : static coefficient of friction

v_o : normalizing velocity [see Equation (41)]

ρ : density of contacting body

H : Heat of ablation

ELMT28

This is an axisymmetric element, nonlinear thermo-viscoelastic-viscoplastic element for finite strains and large displacements. The element accepts all two-dimensional element types in the FEAMOD library. The data definition and format of the data in the material file is as follows:

card 3 FORMAT(20A4)

Convenience title usually "YOUNG POISSON DENSITY CTE TRELAX"

card 4 free format

$E, \nu, \rho, \text{CTE}, t$

card 5 FORMAT(20A4)

Convenience title usually "Z0 Z1 M N D0"

card 6 free format

z_o, z_1, m, n, D_o

where the meaning of these viscoplastic variables are described in Section 3.3.1

card 7 FORMAT(20A4)

Convenience title usually "NGAUSS"

card 8 free format

integer order of Gaussian integration

ELMT12

This is a one-dimensional axisymmetric element, 6-node element, that enforces sliding contact between elements that are at an arbitrary orientation. The local node numbering of each node is shown in Figure A.2. Opposing nodes need initially to be in the general vicinity of each other. The element enforces this constraint using a penalty method. The penalty is defined by the parameter $1/\epsilon$, and ϵ should be set no smaller than 10^{-3} for single precision calculations. The data definition and format of the data in the material file is as follows:

card 3 FORMAT(20A4)

Convenience title usually "YOUNG EPS XMU0"

card 4 (free format)

E, ϵ, μ

where each variable is defined as

E : Young's modulus of contacting body

ϵ : ratio of Young's modulus of contacting body and rigid wall

μ : coefficient of friction

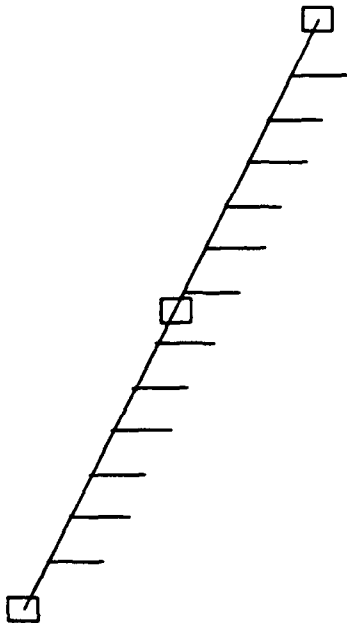


Figure A.1

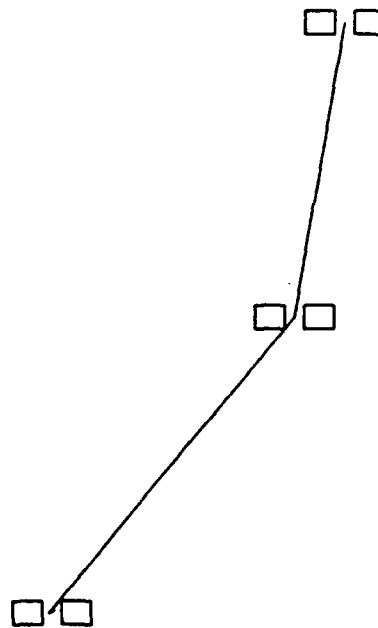


Figure A.2

APPENDIX B
SUPERTAB UNIVERSAL FILE FORMAT DEFINITION

Universal Dataset

Type: 15

Name: Nodes

Status: Current

Written by: I-DEAS Level 3 Frame

Written by: I-DEAS Level 3 Supertab

Written by: I-DEAS Level 3 Systan

Read by: I-DEAS Level 3 Supertab

Read by: I-DEAS Level 3 Systan

Written by: I-DEAS Level 2.5 Supertab

Written by: I-DEAS Level 2.5 Systan

Revision date: 22-JAN-1986

RECORD 1: FORMAT(4I10,1P3E13.5)

FIELD 1: NODE LABEL

FIELD 2: DEFINITION COORDINATE SYSTEM NUMBER

FIELD 3: DISPLACEMENT COORDINATE SYSTEM NUMBER

FIELD 4: COLOR

FIELDS 5-7: 3-DIMENSIONAL COORDINATES OF
 NODE IN THE DEFINITION SYSTEM

RECORD 1 IS REPEATED FOR EACH NODE IN THE MODEL.

EXAMPLE:

-1					
15					
1	0	0	8	0.00000E+00	0.00000E+00
0.00000E+00					
2	0	0	8	5.00000E-01	0.00000E+00
-5.00000E-02					
.					
.					
.					
100	0	0	8	1.20000E+01	1.20000E+01
-4.50000E+00					
-1					

Universal Dataset

Type: 55

Name: Data at nodes

Status: Current

Written by: I-DEAS Level 3 Frame

Written by: I-DEAS Level 3 Supertab

Written by: I-DEAS Level 3 Systan

Written by: I-DEAS Level 3 Tdas

Read by: I-DEAS Level 3 Frame

Read by: I-DEAS Level 3 Supertab

Read by: I-DEAS Level 3 Systan

Read by: I-DEAS Level 3 Tdas

Written by: I-DEAS Level 2.5 Supertab

Written by: I-DEAS Level 2.5 Systan

Revision date: 29-JAN-1986

Systan and Tdas use a slightly different form of this dataset. See "Systan Notes" and "Tdas Notes" below for differences.

RECORD 1: FORMAT (40A2)
FIELD 1: ID LINE 1

RECORD 2: FORMAT (40A2)
FIELD 1: ID LINE 2

RECORD 3: FORMAT (40A2)
FIELD 1: ID LINE 3

RECORD 4: FORMAT (40A2)
FIELD 1: ID LINE 4

RECORD 5: FORMAT (40A2)
FIELD 1: ID LINE 5

RECORD 6: FORMAT (6I10)

DATA DEFINITION PARAMETERS

FIELD 1: MODEL TYPE 0: UNKNOWN
 1: STRUCTURAL
 2: HEAT TRANSFER
 3: FLUID FLOW

FIELD 2: ANALYSIS TYPE 0: UNKNOWN
 1: STATIC
 2: NORMAL MODE
 3: COMPLEX EIGENVALUE (FIRST ORDER)
 (COMPLEX CONJUGATE PAIRS NOT
 INCLUDED)
 -3: COMPLEX EIGENVALUE (FIRST ORDER)
 (COMPLEX CONJUGATE PAIRS
 INCLUDED)
 4: TRANSIENT

5: FREQUENCY RESPONSE
6: BUCKLING
7: COMPLEX EIGENVALUE (SECOND ORDER)

FIELD 3: DATA CHARACTERISTIC

0: UNKNOWN
1: SCALAR
2: 3 DOF GLOBAL TRANSLATION VECTOR
3: 6 DOF GLOBAL TRANSLATION & ROTATION VECTOR
4: SYMMETRIC GLOBAL TENSOR
5: GENERAL GLOBAL TENSOR

FIELD 4: SPECIFIC DATA TYPE

0: UNKNOWN
1: GENERAL
2: STRESS
3: STRAIN
4: ELEMENT FORCE
5: TEMPERATURE
6: HEAT FLUX
7: STRAIN ENERGY
8: DISPLACEMENT
9: REACTION FORCE
10: KINETIC ENERGY
11: VELOCITY
12: ACCELERATION
13: STRAIN ENERGY DENSITY
14: KINETIC ENERGY DENSITY
15: HYDRO-STATIC PRESSURE
16: HEAT GRADIENT
17: CODE CHECKING VALUE
18: COEFFICIENT OF PRESSURE

FIELD 5: DATA TYPE

2: REAL
5: COMPLEX

FIELD 6: NUMBER OF DATA VALUES PER NODE (NDV)

RECORDS 7 AND 8 ARE ANALYSIS TYPE SPECIFIC

GENERAL FORM

RECORD 7: FORMAT (8I10)
 FIELD 1: NUMBER OF INTEGER DATA VALUES
 1 < OR = NINT < OR = 10
 FIELD 2: NUMBER OF REAL DATA VALUES
 1 < OR = NRVAL < OR = 12
 FIELDS 3-N: TYPE SPECIFIC INTEGER PARAMETERS

RECORD 8: FORMAT (6E13.5)
 FIELDS 1-N: TYPE SPECIFIC REAL PARAMETERS

FOR ANALYSIS TYPE = 0, UNKNOWN

RECORD 7:

FIELD 1:1
FIELD 2:1
FIELD 3:ID NUMBER

RECORD 8:
FIELD 1:0.0

FOR ANALYSIS TYPE = 1, STATIC

RECORD 7:
FIELD 1: 1
FIELD 2: 1
FIELD 3: LOAD CASE NUMBER

RECORD 8:
FIELD 1: 0.0

FOR ANALYSIS TYPE = 2, NORMAL MODE

RECORD 7:
FIELD 1: 2
FIELD 2: 4
FIELD 3: LOAD CASE NUMBER
FIELD 4: MODE NUMBER

RECORD 8:
FIELD 1: FREQUENCY (HERTZ)
FIELD 2: MODAL MASS
FIELD 3: MODAL VISCOUS DAMPING RATIO
FIELD 4: MODAL HYSTERETIC DAMPING RATIO

FOR ANALYSIS TYPE = 3, COMPLEX EIGENVALUE (FIRST ORDER)

RECORD 7:
FIELD 1: 2
FIELD 2: 6
FIELD 3: LOAD CASE NUMBER
FIELD 4: MODE NUMBER

RECORD 8:
FIELD 1: REAL PART EIGENVALUE
FIELD 2: IMAGINARY PART EIGENVALUE
FIELD 3: REAL PART OF MODAL A
FIELD 4: IMAGINARY PART OF MODAL A
FIELD 5: REAL PART OF MODAL B
FIELD 6: IMAGINARY PART OF MODAL B

FOR ANALYSIS TYPE = -3, COMPLEX EIGENVALUE (FIRST ORDER)

RECORD 7:
FIELD 1: 2
FIELD 2: 6
FIELD 3: LOAD CASE NUMBER
FIELD 4: MODE NUMBER

RECORD 8:

FIELD 1: REAL PART EIGENVALUE
FIELD 2: IMAGINARY PART EIGENVALUE
FIELD 3: REAL PART OF MODAL A
FIELD 4: IMAGINARY PART OF MODAL A
FIELD 5: REAL PART OF MODAL B
FIELD 6: IMAGINARY PART OF MODAL B

FOR ANALYSIS TYPE = 4, TRANSIENT

RECORD 7:

FIELD 1: 2
FIELD 2: 1
FIELD 3: LOAD CASE NUMBER
FIELD 4: TIME STEP NUMBER

RECORD 8:

FIELD 1: TIME (SECONDS)

FOR ANALYSIS TYPE = 5, FREQUENCY RESPONSE

RECORD 7:

FIELD 1: 2
FIELD 2: 1
FIELD 3: LOAD CASE NUMBER
FIELD 4: FREQUENCY STEP NUMBER

RECORD 8:

FIELD 1: FREQUENCY (HERTZ)

FOR ANALYSIS TYPE = 6, BUCKLING

RECORD 7:

FIELD 1: 1
FIELD 2: 1
FIELD 3: LOAD CASE NUMBER

RECORD 8:

FIELD 1: EIGENVALUE

RECORD 9: FORMAT (I10)

FIELD 1: NODE NUMBER

RECORD 10: FORMAT (6E13.5)

FIELDS 1-N: DATA AT THIS NODE (NDV REAL OR
 COMPLEX VALUES)

FOR ANALYSIS TYPE = 7, COMPLEX EIGENVALUES (SECOND ORDER)

RECORD 7:

FIELD 1: 2
FIELD 2: 6
FIELD 3: LOAD CASE NUMBER
FIELD 4: MODE NUMBER

RECORD 8:

FIELD 1: REAL PART EIGENVALUE
FIELD 2: IMAGINARY PART EIGENVALUE
FIELD 3: REAL PART OF MODAL MASS
FIELD 4: IMAGINARY PART OF MODAL MASS
FIELD 5: REAL PART OF MODAL STIFFNESS
FIELD 6: IMAGINARY PART OF MODAL STIFFNESS

RECORDS 9 AND 10 ARE REPEATED FOR EACH NODE.

- NOTES:
1. ID LINES MAY NOT BE BLANK. IF NO INFORMATION IS REQUIRED, THE WORD "NONE" MUST APPEAR IN COLUMNS 1-4.
 2. FOR COMPLEX DATA THERE WILL BE 2*NDV DATA ITEMS AT EACH NODE. THE ORDER IS REAL PART FOR VALUE 1, IMAGINARY PART FOR VALUE 1, ETC.
 3. THE ORDER OF VALUES FOR VARIOUS DATA CHARACTERISTICS IS:

3 DOF GLOBAL VECTOR: X, Y, Z
6 DOF GLOBAL VECTOR: X, Y, Z, RX, RY, RZ
SYMMETRIC GLOBAL TENSOR: SXX, SXY, SYX,
SXZ, SYZ, SZZ

GENERAL GLOBAL TENSOR: SXX, SYX, SZX,
SXY, SYY, SZY,
SXZ, SYZ, SZZ
 4. ID LINE 1 ALWAYS APPEARS ON PLOTS IN OUTPUT DISPLAY.
 5. IF SPECIFIC DATA TYPE IS "UNKNOWN," ID LINE 2 IS DISPLAYED AS DATA TYPE IN OUTPUT DISPLAY.
 6. TYPICAL FORTRAN I/O STATEMENTS FOR THE DATA SECTIONS ARE:

```
      READ(LUN,1000)NUM
      WRITE
1000  FORMAT (I10)
      READ(LUN,1010) (VAL(I),I=1,NDV)
      WRITE
1010  FORMAT (6E13.5)
```

WHERE: NUM IS NODE NUMBER
VAL IS REAL OR COMPLEX DATA
ARRAY
NDV IS NUMBER OF DATA VALUES
PER NODE

7. DATA CHARACTERISTIC VALUES IMPLY THE FOLLOWING VALUES OF NDV:

- 3: COMPLEX EIGENVALUE (FIRST ORDER)
(COMPLEX CONJUGATE PAIRS NOT INCLUDED)
- 3: COMPLEX EIGENVALUE (FIRST ORDER)
(COMPLEX CONJUGATE PAIRS INCLUDED)
- 7: COMPLEX EIGENVALUE (SECOND ORDER)

FIELD 3: DATA CHARACTERISTIC 2: 3 DOF GLOBAL TRANSLATION VECTOR
 3: 6 DOF GLOBAL TRANSLATION & ROTATION VECTOR

FIELD 4: SPECIFIC DATA TYPE 8: DISPLACEMENT
 11: VELOCITY
 12: ACCELERATION

Tdas notes:

1. DATA ASSOCIATED WITH SDRC MODAL-PLUS HAS THE FOLLOWING SPECIAL FORM OF ID LINE 5.

FORMAT (4I10)

FIELD 1: REFERENCE COORDINATE LABEL
(1-8000)

FIELD 2: REFERENCE COORDINATE DIRECTION
 1: X DIRECTION
 -1: -X DIRECTION
 2: Y DIRECTION
 -2: -Y DIRECTION
 3: Z DIRECTION
 -3: -Z DIRECTION

FIELD 3: NUMERATOR SIGNAL CODE
 1: DISPLACEMENT
 2: VELOCITY
 3: ACCELERATION
 4: FORCE

FIELD 4: DENOMINATOR SIGNAL CODE
 1: DISPLACEMENT
 2: VELOCITY
 3: ACCELERATION
 4: FORCE

This plus records 7 and 8 are used to calculate Modal Mass and Residue with the following specifications.

ID line 5

Read:

- Modal Plus used the information in ID line 5 to scale the residue amplitude.
- Tdas prompts the user for the reference/response to be used for scaling the residue and ignores the reference in ID line 5.

Record 8

Read:

- Modal Plus zeros the value of modal mass on the read.
- Tdas stores the value of the modal mass directly in the shape header.

Write:

- Both Modal-Plus and Tdas calculate and write the modal mass based on the parameter table (not the value).

2. For Record 6 Field 4-Specific data type, values 0 through 12 are as defined above. 13 and 15 through 19 are:

13: excitation force
15: pressure
16: mass
17: time
18: frequency
19: rpm

Universal Dataset

Type: 56

Name: Data on elements

Status: Current

Written by: I-DEAS Level 3 Frame

Written by: I-DEAS Level 3 Supertab

Read by: I-DEAS Level 3 Supertab

Written by: I-DEAS Level 2.5 Supertab

Revision date: 15-JAN-1986

RECORD 1: FORMAT (40A2)
FIELD 1: ID LINE 1

RECORD 2: FORMAT (40A2)
FIELD 1: ID LINE 2

RECORD 3: FORMAT (40A2)
FIELD 1: ID LINE 3

RECORD 4: FORMAT (40A2)
FIELD 1: ID LINE 4

RECORD 5: FORMAT (40A2)
FIELD 1: ID LINE 5

RECORD 6: FORMAT (6I10)

DATA DEFINITION PARAMETERS

FIELD 1: MODEL TYPE 0: UNKNOWN
 1: STRUCTURAL
 2: HEAT TRANSFER
 3: FLUID FLOW

FIELD 2: ANALYSIS TYPE 0: UNKNOWN
 1: STATIC
 2: NORMAL MODE
 3: COMPLEX EIGENVALUE
 4: TRANSIENT
 5: FREQUENCY RESPONSE
 6: BUCKLING

FIELD 3: DATA CHARACTERISTIC 0: UNKNOWN
 1: SCALAR
 2: 3 DOF GLOBAL TRANSLATION
 VECTOR
 3: 6 DOF GLOBAL TRANSLATION &
 ROTATION VECTOR
 4: SYMMETRIC GLOBAL TENSOR
 5: GENERAL GLOBAL TENSOR

FIELD 4: SPECIFIC DATA TYPE 0: UNKNOWN
 1: UNKNOWN

2: STRESS
3: STRAIN
4: ELEMENT FORCE
5: TEMPERATURE
6: HEAT FLUX
7: STRAIN ENERGY
8: DISPLACEMENT
9: REACTION FORCE
10: KINETIC ENERGY
11: VELOCITY
12: ACCELERATION
13: STRAIN ENERGY DENSITY
14: KINETIC ENERGY DENSITY
15: HYDRO-STATIC PRESSURE
16: HEAT GRADIENT
17: CODE CHECKING VALUE
18: COEFFICIENT OF PRESSURE

FIELD 5: DATA TYPE

2: REAL
5: COMPLEX

FIELD 6: NUMBER OF DATA VALUES FOR EACH POSITION ON THE
ELEMENT (NDV)

RECORDS 7 AND 8 ARE ANALYSIS TYPE SPECIFIC

GENERAL FORM

RECORD 7: FORMAT (8I10)
 FIELD 1: NUMBER OF INTEGER DATA VALUES
 1 < OR = NINT < OR = 10
 FIELD 2: NUMBER OF REAL DATA VALUES
 1 < OR = NRVAL < OR = 12
 FIELDS 3-N: TYPE SPECIFIC INTEGER PARAMETERS

RECORD 8: FORMAT (6E13.5)
 FIELDS 1-N: TYPE SPECIFIC REAL PARAMETERS

FOR ANALYSIS TYPE = 0, UNKNOWN

RECORD 7:
 FIELD 1: 1
 FIELD 2: 1
 FIELD 3: ID NUMBER

RECORD 8:
 FIELD 1: 0.0

FOR ANALYSIS TYPE = 1, STATIC

RECORD 7:
 FIELD 1: 1
 FIELD 2: 1
 FIELD 3: LOAD CASE NUMBER

RECORD 8:

FIELD 4: 0.0

FOR ANALYSIS TYPE = 2, NORMAL MODE

RECORD 7:

FIELD 1: 2

FIELD 2: 3

FIELD 3: LOAD CASE NUMBER

FIELD 4: MODE NUMBER

RECORD 8:

FIELD 1: FREQUENCY (HERTZ)

FIELD 2: MODAL MASS

FIELD 3: MODAL DAMPING

FOR ANALYSIS TYPE = 3, COMPLEX EIGENVALUE

RECORD 7:

FIELD 1: 2

FIELD 2: 6

FIELD 3: LOAD CASE NUMBER

FIELD 4: MODE NUMBER

RECORD 8:

FIELD 1: REAL PART EIGENVALUE

FIELD 2: IMAGINARY PART EIGENVALUE

FIELD 3: REAL PART OF MODAL A

FIELD 4: IMAGINARY PART OF MODAL A

FIELD 5: REAL PART OF MODAL B

FIELD 6: IMAGINARY PART OF MODAL B

FOR ANALYSIS TYPE = 4, TRANSIENT

RECORD 7:

FIELD 1: 2

FIELD 2: 1

FIELD 3: LOAD CASE NUMBER

FIELD 4: TIME STEP NUMBER

RECORD 8:

FIELD 1: TIME (SECONDS)

FOR ANALYSIS TYPE = 5, FREQUENCY RESPONSE

RECORD 7:

FIELD 1: 2

FIELD 2: 1

FIELD 3: LOAD CASE NUMBER

FIELD 4: FREQUENCY STEP NUMBER

RECORD 8:

FIELD 1: FREQUENCY (HERTZ)

FOR ANALYSIS TYPE = 6, BUCKLING

RECORD 7:
FIELD 1: 1
FIELD 2: 1
FIELD 3: LOAD CASE NUMBER

RECORD 8:
FIELD 1: EIGENVALUE

RECORD 9: FORMAT (2I10)
FIELD 1: ELEMENT NUMBER
FIELD 2: NUMBER OF DATA VALUES FOR THIS
 ELEMENT (NVAL)

RECORD 10: FORMAT(6E13.5)
FIELDS 1-N: DATA ON ELEMENT (NVAL REAL OR
 COMPLEX VALUES)

RECORDS 9 AND 10 ARE REPEATED FOR ALL ELEMENTS.

- NOTES:
1. ID LINES MAY NOT BE BLANK. IF NO INFORMATION IS REQUIRED, THE WORD "NONE" MUST APPEAR IN COLUMNS 1-4.
 2. FOR COMPLEX DATA THERE WILL BE 2*NVAL DATA ITEMS. THE ORDER IS REAL PART FOR VALUE 1, IMAGINARY PART FOR VALUE 1, REAL PART FOR VALUE 2, IMAGINARY PART FOR VALUE 2, ETC.
 3. THE ORDER OF VALUES FOR VARIOUS DATA CHARACTERISTICS IS:

3 DOF GLOBAL VECTOR: X, Y, Z
6 DOF GLOBAL VECTOR: X, Y, Z, RX, RY, RZ
SYMMETRIC GLOBAL TENSOR: SXX, SXY, SYX, SYY, SYZ, SZY, SZZ, SXZ, SZX

GENERAL GLOBAL TENSOR: SXX, SYX, SZX, SXY, SYY, SZY, SXZ, SYZ, SZZ
 4. ID LINE 1 ALWAYS APPEARS ON PLOTS IN OUTPUT DISPLAY.
 5. IF SPECIFIC DATA TYPE IS "UNKNOWN," ID LINE 2 IS DISPLAYED AS DATA TYPE IN OUTPUT DISPLAY.
 6. TYPICAL FORTRAN I/O STATEMENTS FOR THE DATA SECTIONS ARE:

```
      READ (LUN, 1000) NUM, NVAL  
      WRITE  
1000 FORMAT (2I10)  
      READ (LUN, 1010) (VAL(I), I=1, NVAL)  
      WRITE
```

1010 FORMAT (6E13.5)

WHERE: NUM IS ELEMENT NUMBER
NVAL IS NUMBER OF REAL OR COMPLEX
DATA
VALUES FOR THIS ELEMENT (MAX = 90)
VAL IS REAL OR COMPLEX DATA ARRAY

7. DATA CHARACTERISTIC VALUES IMPLY THE FOLLOWING
VALUES OF NDV:

SCALAR: 1
3 DOF GLOBAL VECTOR: 3
6 DOF GLOBAL VECTOR: 6
SYMMETRIC GLOBAL TENSOR: 6
GENERAL GLOBAL TENSOR: 9

8. DATA ON 2D TYPE ELEMENTS MAY HAVE MULTIPLE VALUES
THROUGH THE ELEMENT THICKNESS. IN THESE CASES,
NVAL = NDV*NPOS WHERE NPOS IS NUMBER OF POSITIONS
THROUGH ELEMENT. NPOS IS ALWAYS 1 FOR SOLIDS.
THE ORDER OF THE DATA IS NDV VALUES FOR POSITION 1,
NDV VALUES FOR POSITION 2, ETC. THE ORDER OF THE
NODES DEFINES AN OUTWARD NORMAL WHICH SPECIFIES THE
ORDER FROM POSITION 1 TO NPOS.
9. ANY RECORD WITH ALL 0.0'S DATA ENTRIES NEED NOT
(BUT MAY) APPEAR.
10. A DIRECT RESULT OF 9 IS THAT IF NO RECORD 9 & 10
APPEARS, ALL DATA FOR THE DATA SET IS 0.0.
11. WHEN NEW ANALYSIS TYPES ARE ADDED, RECORD 7 FIELDS
1 AND 2 ARE ALWAYS > OR = 1 WITH DUMMY INTERGER AND
REAL ZERO DATA IF DATA IS NOT REQUIRED. IF COMPLEX
DATA IS NEEDED, IT IS TREATED AS TWO REAL NUMBERS,
REAL PART FOLLOWED BY IMAGINARY POINT.
12. DATALOADERS USE THE FOLLOWING ID LINE CONVENTION:

1. (80A1) MODEL IDENTIFICATION
2. (80A1) RUN IDENTIFICATION
3. (80A1) RUN DATE/TIME
4. (80A1) LOAD CASE NAME

FOR STATIC:

5. (17H LOAD CASE NUMBER;, 110)

FOR NORMAL MODE:

5. (10H MODE SAME, 110, 10H FREQUENCY, E13.5)

13. MAXIMUM VALUE FOR NDV IS 9.
MAXIMUM VALUE FOR NVAL IS 90.

14. TYPICAL FORTRAN I/O STATEMENTS FOR PROCESSING
RECORDS 7 AND 8.

```
      READ (LUN, 1000) NINT, NRVAL, (IPAR(I), I=1, NINT)
1000 FORMAT (8I10)
      READ (LUN, 1010) (NRVAL(I), I=1, NRVAL)
1010 FORMAT (6E13.5)
```

Universal Dataset

Type: 71

Name: Elements

Status: Current

Written by: I-DEAS Level 3 Frame

Written by: I-DEAS Level 3 Supertab

Read by: I-DEAS Level 3 Supertab

Read by: I-DEAS Level 3 Systan

Written by: I-DEAS Level 2.5 Supertab

Revision date: 15-JAN-1986

RECORD 1: FORMAT(7I10)
FIELD 1: ELEMENT LABEL
FIELD 2: FE GRAPHICAL DESCRIPTION ID
FIELD 3: FE DESCRIPTOR ID
FIELD 4: PHYSICAL PROPERTY TABLE NUMBER
FIELD 5: MATERIAL PROPERTY TABLE NUMBER
FIELD 6: COLOR
FIELD 7: NUMBER OF NODES ON ELEMENT

RECORD 2: FORMAT (8I10)
FIELDS 1-N: NODE LABELS DEFINING ELEMENT

RECORDS 1 AND 2 ARE REPEATED FOR EACH ELEMENT IN THE MODEL.

EXAMPLE:

```
-1
71
  1      19      1      1      1      8
  8
 11      12      13      16      21      20
 19      15
  2      12      2      2      1      8
 16
 31      32      33      34      35      36
 37      38
 39      40      41      42      43      44
 45      46
  .
  .
  .
124      19      1      1      1      8
  8
  9      10      11      15      19      18
 17      14
-1
```

Universal Dataset

Type: 88

Name: Constraint set

Status: Current

Written by: I-DEAS Level 3 Supertab

Read by: I-DEAS Level 3 Supertab

Revision date: 15-JAN-1986

RECORD 1: FORMAT (2110)
 FIELD 1: CONSTRAINT SET NUMBER
 FIELD 2: CONSTRAINT TYPE
 1 - KINEMATICS
 2 - COUPLED DOFS
 3 - MULTI-POINT CONSTRAINT EQUATIONS

RECORD 2: FORMAT (20A2)
 FIELD 1: CONSTRAINT SET NAME

FOR CONSTRAINT TYPE = 1 - KINEMATICS

RECORD 3: FORMAT (2110,612)
 FIELD 1: KINEMATIC NODE LABEL
 FIELD 2: COLOR NUMBER
 FIELDS 3-8: SWITCHES FOR DOFS 1-6
 0 - OFF
 1 - ON

RECORD 3 IS REPEATED FOR EACH KINEMATIC OF THE CONSTRAINT SET.

FOR CONSTRAINT TYPE = 2 - COUPLED DOFS

RECORD 3: FORMAT (3110,612)
 FIELD 1: INDEPENDENT NODE LABEL
 FIELD 2: COLOR NUMBER
 FIELD 3: NUMBER OF DEPENDENT NODES
 FIELDS 4-9: SWITCHES FOR DOFS 1-6
 0 - OFF
 1 - ON

RECORD 4+N: FORMAT (8110)
 FIELDS 1-8: DEPENDENT NODE LABELS

RECORDS 3, 4, AND 4+N ARE REPEATED FOR EACH COUPLED DOF OF THE CONSTRAINT SET.

FOR CONSTRAINT TYPE = 3 - MULTI-POINT CONSTRAINT EQUATION

RECORD 3: FORMAT (4110,1PE13.5)
 FIELD 1: EQUATION LABEL
 FIELD 2: NUMBER OF TERMS
 FIELD 3: FORCE/DISPLACEMENT SWITCH
 1 - FORCE
 2 - DISPLACEMENT

FIELD 4: COLOR NUMBER
FIELD 5: CONSTANT FORCE/DISPLACEMENT VALUE

RECORD 4+N: FORMAT (I10,I2,IPE13.5)
FIELD 1: NODE LABEL
FIELD 2: NODAL DEGREE OF FREEDOM
1 - X
2 - Y
3 - Z
4 - X ROTATIONAL
5 - Y ROTATIONAL
6 - Z ROTATIONAL
FIELD 3: CONSTRAINT COEFFICIENT

RECORDS 3, 4, AND 4+N ARE REPEATED FOR EACH MULTI-POINT
CONSTRAINT EQUATION OF THE CONSTRAINT SET.

THE ENTIRE SET OF RECORDS, INCLUDING THE SEPARATORS AND THE
DATASET TYPE RECORDS, IS REPEATED FOR EACH CONSTRAINT TYPE OF
EACH CONSTRAINT SET IN THE MODEL.

Universal Dataset

Type: 89

Name: Restraint set

Status: Current

Written by: I-DEAS Level 3 Supertab

Read by: I-DEAS Level 3 Supertab

Revision date: 15-JAN-1986

RECORD 1: FORMAT (2I10)
 FIELD 1: RESTRAINT SET NUMBER
 FIELD 2: RESTRAINT TYPE
 1 - NODAL DISPLACEMENT
 2 - NODAL TEMPERATURE

RECORD 2: FORMAT (20A2)
 FIELD 1: RESTRAINT SET NAME

FOR RESTRAINT TYPE = 1 - NODAL DISPLACEMENT

RECORD 3: FORMAT (2I10,6I2)
 FIELD 1: RESTRAINT LABEL
 FIELD 2: COLOR NUMBER
 FIELDS 3-8: SWITCHES FOR DOFS 1-6
 0 - OFF
 1 - ON

RECORD 4: FORMAT (1P6E13.5)
 FIELDS 1-6: DISPLACEMENT DOFS 1-6

RECORDS 3 AND 4 ARE REPEATED FOR EACH NODE IN THE RESTRAINT SET.

FOR RESTRAINT TYPE = 2 - NODAL TEMPERATURE

RECORD 3: FORMAT (2I10,1PE13.5)
 FIELD 1: RESTRAINT LABEL
 FIELD 2: COLOR NUMBER
 FIELD 3: TEMPERATURE VALUE

RECORD 3 IS REPEATED FOR EACH NODE IN THE RESTRAINT SET.

THE ENTIRE SET OF RECORDS, INCLUDING THE SEPARATORS AND THE DATASET TYPE RECORDS, IS REPEATED FOR EACH RESTRAINT TYPE OF EACH RESTRAINT SET IN THE MODEL.

Universal Dataset

Type: 90

Name: Load set

Status: Current

Written by: I-DEAS Level 3 Supertab

Read by: I-DEAS Level 3 Supertab

Revision date: 15-JAN-1986

RECORD 1: FORMAT (2I10)

FIELD 1: LOAD SET NUMBER

FIELD 2: LOAD TYPE

- 1 - NODAL FORCE
- 2 - NODAL TEMPERATURE
- 3 - FINITE ELEMENT FACE PRESSURE
- 4 - FINITE ELEMENT FACE HEAT FLUX
- 5 - FINITE ELEMENT EDGE PRESSURE
- 6 - FINITE ELEMENT EDGE HEAT FLUX
- 7 - NODAL HEAT SOURCE

RECORD 2: FORMAT (20A2)

FIELD 1: LOAD SET NAME

FOR LOAD TYPE = 1 NODAL FORCES

RECORD 3: FORMAT (2I10,6I2)

FIELD 1: NODAL FORCE LABEL

FIELD 2: COLOR NUMBER

FIELDS 3-8: SWITCHES FOR DOFS 1-6

0 - OFF

1 - ON

RECORD 4: FORMAT (1P6E!3.5)

FIELD 1: FORCE FOR DOF 1

FIELD 2: FORCE FOR DOF 2

FIELD 3: FORCE FOR DOF 3

FIELD 4: FORCE FOR DOF 4

FIELD 5: FORCE FOR DOF 5

FIELD 6: FORCE FOR DOF 6

RECORDS 3 AND 4 ARE REPEATED FOR EACH NODAL FORCE OF
THE LOAD SET.

FOR LOAD TYPE = 2 NODAL TEMPERATURES

RECORD 3: FORMAT (2I10,1PE!3.5)

FIELD 1: NODAL TEMPERATURE LABEL

FIELD 2: COLOR NUMBER

FIELD 3: TEMPERATURE VALUE

RECORD 3 IS REPEATED FOR EACH NODAL TEMPERATURE OF THE
LOAD SET.

FOR LOAD TYPE = 3 FINITE ELEMENT FACE PRESSURE

RECORD 3: FORMAT (2I10,6I2)
 FIELD 1: FINITE ELEMENT LABEL
 FIELD 2: COLOR NUMBER
 FIELDS 3-8: SWITCHES FOR FACES 1-6
 0 - OFF
 1 - ON

RECORD 4: FORMAT (1P6E13.5)
 FIELDS 1-6: PRESSURE VALUES ON FACES 1-6

RECORDS 3 AND 4 ARE REPEATED FOR EACH FINITE ELEMENT FACE
PRESSURE OF THE LOAD SET.

FOR LOAD TYPE = 4 FINITE ELEMENT FACE HEAT FLUX

RECORD 3: FORMAT (2I10,6I2)
 FIELD 1: FINITE ELEMENT LABEL
 FIELD 2: COLOR NUMBER
 FIELDS 3-8: SWITCHES FOR FACES 1-6
 0 - OFF
 1 - ON

RECORD 4: FORMAT (1P6E13.5)
 FIELDS 1-6: HEAT FLUX VALUES ON FACES 1-6

RECORDS 3 AND 4 ARE REPEATED FOR EACH FINITE ELEMENT FACE
HEAT FLUX OF THE LOAD SET.

FOR LOAD TYPE = 5 FINITE ELEMENT EDGE PRESSURE

RECORD 3: FORMAT (2I10)
 FIELD 1: FINITE ELEMENT LABEL
 FIELD 2: COLOR NUMBER

RECORD 4: FORMAT (1P4E13.5)
 FIELD 1: PRESSURE VALUE ON EDGE 1, END 1
 FIELD 2: PRESSURE VALUE ON EDGE 1, END 2
 FIELD 3: PRESSURE VALUE ON EDGE 2, END 1
 FIELD 4: PRESSURE VALUE ON EDGE 2, END 2

RECORD 5: FORMAT (1P4E13.5)
 FIELD 1: PRESSURE VALUE ON EDGE 3, END 1
 FIELD 2: PRESSURE VALUE ON EDGE 3, END 2
 FIELD 3: PRESSURE VALUE ON EDGE 4, END 1
 FIELD 4: PRESSURE VALUE ON EDGE 4, END 2

RECORD 6: FORMAT (1P4E13.5)
 FIELD 1: PRESSURE VALUE ON EDGE 5, END 1
 FIELD 2: PRESSURE VALUE ON EDGE 5, END 2
 FIELD 3: PRESSURE VALUE ON EDGE 6, END 1
 FIELD 4: PRESSURE VALUE ON EDGE 6, END 2

RECORD 7: FORMAT (1P4E13.5)
 FIELD 1: PRESSURE VALUE ON EDGE 7, END 1

FIELD 2: PRESSURE VALUE ON EDGE 7, END 2
FIELD 3: PRESSURE VALUE ON EDGE 8, END 1
FIELD 4: PRESSURE VALUE ON EDGE 8, END 2

RECORD 8: FORMAT (1P4E13.5)
FIELD 1: PRESSURE VALUE ON EDGE 9, END 1
FIELD 2: PRESSURE VALUE ON EDGE 9, END 2
FIELD 3: PRESSURE VALUE ON EDGE 10, END 1
FIELD 4: PRESSURE VALUE ON EDGE 10, END 2

RECORD 9: FORMAT (1P4E13.5)
FIELD 1: PRESSURE VALUE ON EDGE 11, END 1
FIELD 2: PRESSURE VALUE ON EDGE 11, END 2
FIELD 3: PRESSURE VALUE ON EDGE 12, END 1
FIELD 4: PRESSURE VALUE ON EDGE 12, END 2

RECORD 10: FORMAT (1P4E13.5)
FIELD 1: PRESSURE VALUE ON EDGE 13, END 1
FIELD 2: PRESSURE VALUE ON EDGE 13, END 2
FIELD 3: PRESSURE VALUE ON EDGE 14, END 1
FIELD 4: PRESSURE VALUE ON EDGE 14, END 2

RECORD 11: FORMAT (1P4E13.5)
FIELD 1: PRESSURE VALUE ON EDGE 15, END 1
FIELD 2: PRESSURE VALUE ON EDGE 15, END 2
FIELD 3: PRESSURE VALUE ON EDGE 16, END 1
FIELD 4: PRESSURE VALUE ON EDGE 16, END 2

RECORDS 3 - 11 ARE REPEATED FOR EACH FINITE ELEMENT EDGE
PRESSURE OF THE LOAD SET. SEE DOCUMENTATION FOR THE DEFINITIONS
OF EDGES 1-16 FOR SPECIFIC FINITE ELEMENT FAMILIES.

FOR LOAD TYPE = 6 FINITE ELEMENT EDGE HEAT FLUX

RECORD 3: FORMAT (2I10,4I2)
FIELD 1: FINITE ELEMENT LABEL
FIELD 2: COLOR NUMBER
FIELDS 3-6: EDGE SWITCHES FOR EDGES 1 - 4
 =0, NO FLUX ON THIS EDGE
 =1, FLUX ON THIS EDGE

RECORD 4: FORMAT (1P4E13.5)
FIELD 1: HEAT FLUX VALUE ON EDGE 1, END 1
FIELD 2: HEAT FLUX VALUE ON EDGE 1, END 2
FIELD 3: HEAT FLUX VALUE ON EDGE 2, END 1
FIELD 4: HEAT FLUX VALUE ON EDGE 2, END 2

RECORD 5: FORMAT (1P4E13.5)
FIELD 1: HEAT FLUX VALUE ON EDGE 3, END 1
FIELD 2: HEAT FLUX VALUE ON EDGE 3, END 2
FIELD 3: HEAT FLUX VALUE ON EDGE 4, END 1
FIELD 4: HEAT FLUX VALUE ON EDGE 4, END 2

RECORDS 3, 4, AND 5 ARE REPEATED FOR EACH FINITE ELEMENT EDGE HEAT
FLUX OF THE LOAD SET.

FOR LOAD TYPE = 7

NODAL HEAT SOURCE

RECORD 3: FORMAT (2I10,1PE13.5)
 FIELD 1: NODAL HEAT SOURCE LABEL
 FIELD 2: COLOR NUMBER
 FIELD 3: HEAT SOURCE VALUE

RECORD 3 IS REPEATED FOR EACH NODAL HEAT SOURCE OF THE
LOAD SET.

THE ENTIRE SET OF RECORDS, INCLUDING THE SEPARATORS AND
THE DATASET TYPE RECORDS, IS REPEATED FOR EACH LOAD TYPE
OF EACH LOAD SET IN THE MODEL.

Definition of Edges 1 - 16 for Finite Element Families

- 1 ROD EDGE 1: AXIAL DISTRIBUTED FORCE
 EDGES 2 - 16: NOT APPLICABLE
- 2 BEAM EDGE 1: AXIAL DISTRIBUTED FORCE
 EDGE 2: Y - SHEAR DISTRIBUTED FORCE
 EDGE 3: Z - SHEAR DISTRIBUTED FORCE
 EDGE 4: DISTRIBUTED TORQUE
 EDGE 5: DISTRIBUTED Y - BENDING MOMENT
 EDGE 6: DISTRIBUTED Z - BENDING MOMENT
 EDGES 7 - 16: NOT APPLICABLE
- 3 PIPE EDGE 1: AXIAL DISTRIBUTED FORCE
 EDGE 2: Y - SHEAR DISTRIBUTED FORCE
 EDGE 3: Z - SHEAR DISTRIBUTED FORCE
 EDGE 4: DISTRIBUTED TORQUE
 EDGE 5: DISTRIBUTED Y - BENDING MOMENT
 EDGE 6: DISTRIBUTED Z - BENDING MOMENT
 EDGES 7 - 16: NOT APPLICABLE
- 4 PLANE STRESS EDGE 1: FIRST EDGE OF DISTRIBUTED MEMBRANE LOAD
 EDGE 2: SECOND EDGE OF DISTRIBUTED MEMBRANE LOAD
 EDGE 3: THIRD EDGE OF DISTRIBUTED MEMBRANE LOAD
 EDGE 4: FOURTH EDGE OF DISTRIBUTED MEMBRANE LOAD
 EDGE 5: FIRST EDGE OF DISTRIBUTED SHEAR LOAD
 EDGE 6: SECOND EDGE OF DISTRIBUTED SHEAR LOAD
 EDGE 7: THIRD EDGE OF DISTRIBUTED SHEAR LOAD
 EDGE 8: FOURTH EDGE OF DISTRIBUTED SHEAR LOAD
 EDGES 9 - 16: NOT APPLICABLE
- 5 PLANE STRAIN EDGE 1: FIRST EDGE OF DISTRIBUTED MEMBRANE LOAD
 EDGE 2: SECOND EDGE OF DISTRIBUTED MEMBRANE LOAD
 EDGE 3: THIRD EDGE OF DISTRIBUTED MEMBRANE LOAD
 EDGE 4: FOURTH EDGE OF DISTRIBUTED MEMBRANE LOAD
 EDGE 5: FIRST EDGE OF DISTRIBUTED SHEAR LOAD
 EDGE 6: SECOND EDGE OF DISTRIBUTED SHEAR LOAD
 EDGE 7: THIRD EDGE OF DISTRIBUTED SHEAR LOAD
 EDGE 8: FOURTH EDGE OF DISTRIBUTED SHEAR LOAD

EDGES 9 - 16: NOT APPLICABLE

- 6 FLAT PLATE
- EDGE 1: FIRST EDGE OF OUT-OF-PLANE SHEAR LOAD
 - EDGE 2: SECOND EDGE OF OUT-OF-PLANE SHEAR LOAD
 - EDGE 3: THIRD EDGE OF OUT-OF-PLANE SHEAR LOAD
 - EDGE 4: FOURTH EDGE OF OUT-OF-PLANE SHEAR LOAD
 - EDGE 5: FIRST EDGE OF DISTRIBUTED BENDING LOAD
 - EDGE 6: SECOND EDGE OF DISTRIBUTED BENDING LOAD
 - EDGE 7: THIRD EDGE OF DISTRIBUTED BENDING LOAD
 - EDGE 8: FOURTH EDGE OF DISTRIBUTED BENDING LOAD
 - EDGES 9 - 16: NOT APPLICABLE
- 7 MEMBRANE
- EDGE 1: FIRST EDGE OF DISTRIBUTED MEMBRANE LOAD
 - EDGE 2: SECOND EDGE OF DISTRIBUTED MEMBRANE LOAD
 - EDGE 3: THIRD EDGE OF DISTRIBUTED MEMBRANE LOAD
 - EDGE 4: FOURTH EDGE OF DISTRIBUTED MEMBRANE LOAD
 - EDGE 5: FIRST EDGE OF DISTRIBUTED SHEAR LOAD
 - EDGE 6: SECOND EDGE OF DISTRIBUTED SHEAR LOAD
 - EDGE 7: THIRD EDGE OF DISTRIBUTED SHEAR LOAD
 - EDGE 8: FOURTH EDGE OF DISTRIBUTED SHEAR LOAD
 - EDGES 9 - 16: NOT APPLICABLE
- 8 AXISYMMETRIC SOLID
- EDGE 1: FIRST EDGE OF DISTRIBUTED MEMBRANE LOAD
 - EDGE 2: SECOND EDGE OF DISTRIBUTED MEMBRANE LOAD
 - EDGE 3: THIRD EDGE OF DISTRIBUTED MEMBRANE LOAD
 - EDGE 4: FOURTH EDGE OF DISTRIBUTED MEMBRANE LOAD
 - EDGE 5: FIRST EDGE OF DISTRIBUTED SHEAR LOAD
 - EDGE 6: SECOND EDGE OF DISTRIBUTED SHEAR LOAD
 - EDGE 7: THIRD EDGE OF DISTRIBUTED SHEAR LOAD
 - EDGE 8: FOURTH EDGE OF DISTRIBUTED SHEAR LOAD
 - EDGES 9 - 16: NOT APPLICABLE
- 9 THIN SHELL
- EDGE 1: FIRST EDGE OF DISTRIBUTED MEMBRANE LOAD
 - EDGE 2: SECOND EDGE OF DISTRIBUTED MEMBRANE LOAD
 - EDGE 3: THIRD EDGE OF DISTRIBUTED MEMBRANE LOAD
 - EDGE 4: FOURTH EDGE OF DISTRIBUTED MEMBRANE LOAD
 - EDGE 5: FIRST EDGE OF DISTRIBUTED SHEAR LOAD
 - EDGE 6: SECOND EDGE OF DISTRIBUTED SHEAR LOAD
 - EDGE 7: THIRD EDGE OF DISTRIBUTED SHEAR LOAD
 - EDGE 8: FOURTH EDGE OF DISTRIBUTED SHEAR LOAD
 - EDGE 9: FIRST EDGE OF OUT-OF-PLANE SHEAR LOAD
 - EDGE 10: SECOND EDGE OF OUT-OF-PLANE SHEAR LOAD
 - EDGE 11: THIRD EDGE OF OUT-OF-PLANE SHEAR LOAD
 - EDGE 12: FOURTH EDGE OF OUT-OF-PLANE SHEAR LOAD
 - EDGE 13: FIRST EDGE OF DISTRIBUTED BENDING LOAD
 - EDGE 14: SECOND EDGE OF DISTRIBUTED BENDING LOAD
 - EDGE 15: THIRD EDGE OF DISTRIBUTED BENDING LOAD
 - EDGE 16: FOURTH EDGE OF DISTRIBUTED BENDING LOAD
- 10 THICK SHELL
- EDGES 1 - 16: NOT APPLICABLE
- 11 SOLID
- EDGES 1 - 16: NOT APPLICABLE
- 12 RIGID BAR
- EDGES 1 - 16: NOT APPLICABLE

13	SPRING	EDGES 1 - 16: NOT APPLICABLE
14	DAMPER	EDGES 1 - 16: NOT APPLICABLE
15	GAP	EDGES 1 - 16: NOT APPLICABLE
16	LUMPED MASS	EDGES 1 - 16: NOT APPLICABLE
17	AXISYMMETRIC THIN SHELL	EDGE 1: DISTRIBUTED MEMBRANE LOAD EDGE 2: DISTRIBUTED SHEAR LOAD EDGE 3: DISTRIBUTED BENDING LOAD EDGES 4 - 16: NOT APPLICABLE